STRUCTURAL STUDIES IN LONAR CRATER, INDIA AND LOCKNE CRATER, SWEDEN.

Ph. D. THESIS

by
Amar Agarwal

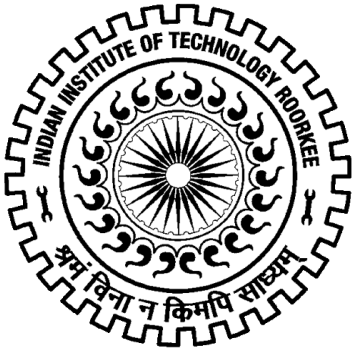

DEPARTMENT OF EARTH SCIENCES
INDIAN INSTITUTE OF TECHNOLOGY ROORKEE
ROORKEE-247 667 (INDIA)

FEBRUARY, 2015

STRUCTURAL STUDIES IN LONAR CRATER, INDIA AND LOCKNE CRATER, SWEDEN.

A THESIS
Submitted in partial fulfilment of the requirements for the award of the degree of
DOCTOR OF PHILOSOPHY
in
EARTH SCIENCES

by

AMAR AGARWAL

DEPARTMENT OF EARTH SCIENCES
INDIAN INSTITUTE OF TECHNOLOGY ROORKEE
ROORKEE-247 667 (INDIA)

FEBRUARY, 2015

INDIAN INSTITUTE OF TECHNOLOGY ROORKEE
ROORKEE

CANDIDATE'S DECLARATION

I hereby certify that the work which is being presented in the thesis entitled "**STRUCTURAL STUDIES IN LONAR CRATER, INDIA AND LOCKNE CRATER, SWEDEN.**" in partial fulfilment of the requirements for the award of the Degree of **Doctor of Philosophy** and submitted in the **Department of Earth Sciences** of the Indian Institute of Technology Roorkee is an authentic record of my own work carried out during a period from July, 2011 to February, 2015 under the supervision of **Dr. D.C. Srivastava,** Professor, Department of Earth Sciences, Indian Institute of Technology Roorkee, Roorkee, India and **Dr. R.O. Greiling,** Professor, Department of Structural Geology and Techtonophysic, Institute of Applied Geosciences, Karlsruhe Institute of Technology, Karlsruhe, Germany.

The matter presented in the thesis has not been submitted by me for the award of any other degree of this or any other Institute.

(AMAR AGARWAL)

This is to certify that the above statement made by the candidate is correct to the best of our knowledge.

(D.C. Srivastava) (R.O. Greiling)

Supervisor Supervisor

Dated: February, 2015

Abstract

Impact crater is an approximately circular depression in the surface of a solid celestial body that is formed by impact of a smaller body. Well preserved impact craters are very common on extra-terrestrial bodies like the Moon or the Mars [1,2], however on the Earth, they are constantly damaged and eliminated by the endogenic and exogenic processes such as active tectonics and erosion. Moreover, the oceanic crust covers two-third of earth's surface, and is constantly recycled, rendering identification of younger impact structure difficult, and that of older impact structures, > 200 Ma, impossible. In consequence, only 200 impact craters have been identified on the earth till date [3].

Impact craters mark global scale catastrophic events [4], in which the deformation occurs at a remarkably high strain rate. The deformation caused by the impact, is provoked by impact generated outward radiating shock waves. Peak shock pressure exerted by the shock wave is a yard stick for the intensity of deformation. The shock pressures, therefore, provide important clues for understanding the cratering process. The most common method of estimating the shock pressures is the identification of shock indicators such as high pressure-temperature polymorphs. However, in weakly shocked rocks such shock indicators are absent and estimations become difficult. In this study, therefore, a combination of rock magnetic and microfracture investigations are used for estimation of shock pressure in the target rocks of two very different craters, the Lonar crater in India and Lockne crater in Sweden.

The Lonar crater in India is a very young, 50 ka old, impact structure [5]. The crater, devoid of any tectonic overprint, can be assumed as pristine. The magnetic fabrics show a good correlation with the magmatic fabric of the impact target rock, i.e., Deccan basalt. The high coercivity component of the natural remnant magnetisation in the crater rim basalt is similar to that in the unshocked basalt, located away from the crater. The lack of any shock related magnetic overprint on the crater rim basalt is, therefore, evident in the Lonar crater. On the other hand, radial and concentric microfractures observed in basalts at the crater rim and farther away, show symmetric distribution with respect to the crater. The concentric fractures

consistently overprint the radial microfractures. The overprinting relationships suggest that the radial and concentric microfractures were developed during propagation of the early compressional and the late decompressional (tensile) shock wave components, respectively. The results of present rock magnetic and microfracture studies, when interpreted in light of the published experimental and numerical simulation studies on the Lonar basalt [6–11], reveal that the shock pressure in the Lonar crater rim was less than 0.5 GPa but greater than 0.2 GPa. These results are in agreement with the pressures estimated through numerical modelling by Louzada et al. [12].

The Lockne crater in Sweden is a 455 Ma old impact structure that has been overthrust by Caledonian napes, obducted, and suffered eroded. The magnetic fabrics in the target basement represent a pre-impact tectonic or magmatic emplacement fabric, and are, therefore, not related to any shock related re-orientation of the magnetic axes. However, the geometry of microfractures, radial or concentric, implies their impact origin. Published reports on experimental and natural craters suggest a correlation between shock induced fractures and peak shock pressures when shock pressures exceed 0.2 GPa [8,9]. Reports of rock magnetic investigations on the target rocks, with magnetic mineralogy similar to that in Lockne basement rocks, show conspicuous shock effects on magnetic fabrics in pressure excess of 0.5 Gpa [6,7,10,12]. Based on these reports, an interpretation of the present results on magnetic fabrics and microfractures reveal that the shock pressure was in the range of 0.5 to 0.2 GPa in rocks up to about 6.5 km from the centre of the crater, and in the order of < 0.2 GPa in the rocks farther away. These estimates are slightly lower than shock pressures numerically calculated by Lindstrom et al. [13].

The shock pressures predicted here or in other published reports either represent pressures experienced by entire mineral grains or represent an average over few cubic centimetres [12–15]. The studied rocks at Lockne crater, according to present and earlier published estimates, suffered very low shock pressures. The correlation between the distinct phases of shock wave and the overprinting sets of orthogonal microfractures is strong in these rocks. This implies that, despite being weak [13], the shock waves caused perceptible deformation.

Shock induced deformation is maximized, due to localization of stresses, as shock waves, especially weak to moderate ones, propagate across grain interfaces [16–18]. The localized stress and heat often cause melting or phase transformation in pockets along the interfaces. In the dolerite target rocks of Lockne impact structure, that according to published reports suffered shock pressure and temperature in the order of <3 GPa and <127°C [13], lingunite nano-crystals are discovered along the augite-labradorite mineral interfaces. Lingunite is a high pressure-temperature polymorph of Na-plagioclase, induced at pressures > 20 GPa and temperatures >1000°C [19,20]. Its presence suggests that although shock pressure and temperature in the bulk rocks were low, pressure-temperatures along the grain boundaries were 10 to 20 times higher due to the shock localization.

The study presents a new approach for estimation of the shock pressures in weakly shocked rocks and gives new information on the relationship between shock pressure and resulting microfractures. In suggests that the shock microfractures may help in discovery of unidentified impact craters.

Acknowledgments

I wish to express deepest gratitude towards Prof. D.C. Srivastava and Prof. R.O. Greiling, who guided me through the challenges and problems occurring during the course of work. Their ideas and support immensely benefited the work and my scientific thinking process. I would also like to thank Dr. A. Kontny for her constant encouragement and suggestions during the course of work. Dr. B. Reznik is thanked for sharing his suggestions and experience without which 'chapter 4' would never be possible.

I would like to thank Deutscher Akademischer Austausch Dienst, Germany (DAAD) and Council of Scientific & Industrial Research, India (CSIR) for providing personal financial support during the research in Germany and India, respectively.

The ideas presented in the present work sprouted from the numerous discussions with my supervisors and Prof. K.K. Agarwal, Prof. F. Schilling, Dr. K. Drüppel and Dr. J. Grimmer. The discussions were always very informative and full of suggestions, for which I am very thankful.

My most sincere regards to Prof. E. F. F. Sturkell and Dr. J. Ormö for their guidance during the field works and for explaining the setting of Lockne impact structure. I would like to thank Mr. P. Lied for his support during the field work at Lockne. Prof. K.K. Agarwal and Mr. D. Rana are thanked for their help during the field work at Lonar. The support extended by Prof. M.A. Mamtani and his group for drilling the cores of samples from Lonar was crucial to the work. The measurements of hysteresis parameters were not possible without the support of Prof. S. Gilder and his group, for which I am very grateful. I would like to express gratitude toward Ms. M. Wiegand for her suggestions during the magnetic measurements.

I am obliged to Mr. S. Unrein for patiently understanding the precise details of oriented thin-section preparation. Mr. V. Zibat, Mr. E. Müller and Mr. S. Heissler are thanked for their support and suggestions during the SEM, TEM and Raman spectroscopy, repectively.

At times of desperation, Ms. M. Chakraborty and Mr. A. Rastogi always provided a personal solace, for which I am ever in debt. Lastly, I would like to expresses most sincere regards to my parents for their unfailing moral support at hardest of the times. The present work is dedicated to them.

Contents

1. Introduction

1.1 Importance of impact on the Earth

Since early 1800s scientists agreed that extra-terrestrial material occasionally penetrate the atmosphere and collide with the Earth [21]. However, before 1960s, collisions of extra-terrestrial objects with the Earth were not considered significant and almost no one believed that such collisions could produce geologically significant effects or could be a global hazard [21]. This view changed drastically with (1) exploration of the solar system, which established the importance of impact cratering in shaping all the planets [22], including the Earth [21,23,24]; and (2) the ability to unambiguously identify impact craters, especially the large and old ones by distinct shock-metamorphic effect [21,25].

In the last few decades, geologists have gradually realized that collisions of extra-terrestrial objects with Earth have significantly shaped Earth's surface, disturbed its crust, and altered its geological history [21,26–29]. The impact structures range from only a few kilometres or less in diameter to large complex structures more than 200 km [21,30,31]. Formation of the larger features, such as the Sudbury in Canada and Vredefort in South Africa, involves widespread disturbances in Earth's crust and major perturbations in the regional geologic history [21].

Other than the geological disturbances, impact events sometimes produce economically valuable geological structures [e.g., 32]. In North America alone, a production value of $ 5 billion is estimated from the impact structures [33]. The economic products of impact craters include diverse items such as local building stone, diamonds, uranium and hydrocarbons (petroleum and gas) [21,34]. The biggest impact-generated bonanza (current production about $2 billion per year) is the Sudbury impact structure in Canada that contains one of the largest nickel-copper sulfide deposits on Earth [21,35,36].

Terrestrial life itself has not escaped this cosmic bombardment [21]. In 1980, Luis and Walter Alvarez and colleagues published a paper outlining evidence for an extra-terrestrial origin for the Cretaceous–Tertiary mass extinction event at approximately 65 Ma [37]. Later, the source, approximately 180 km in diameter wide Chicxulub impact structure, was discovered beneath approximately 1 km of sediment below and half offshore the present day Yucatan Peninsula, Mexico [38].The impact caused severe environmental effects that ranged from local to global and that lasted from seconds to tens of thousands of years [39]. The local and regional effects of the impact event include blast of air and heat, tsunamis and earthquakes [21,30,39]. Global

effects included injection of huge amounts of dust in the upper atmosphere, which may have inhibited photosynthesis for up to 2 months, forest fires ignited when the impact ejecta re-entered the Earth's atmosphere, and the production of vast quantities of N_2O from the shock heating of the atmosphere [39]. While it was initially thought that production of CaO and release of CO_2 due to impact induced vaporization and decomposition of carbonates caused global warming [40], apparently the most destructive effects sprouted from the release of sulphur from the evaporate target rocks [39,41]. Estimates for Chicxulub suggest a 15°C decrease in the average global temperatures, which when coupled with the other effects of the impact event would have resulted in severe environmental consequences [39,41].

1.2 Aim of the study

Shock pressure provides important clues for understanding the cratering process, though its estimate, in weakly shocked rocks, is commonly difficult. Moreover the surface processes such as post-impact tectonic activity, hydrothermal alteration and weathering further obscure the original signatures of shock pressures. In weakly shocked rocks, that lack the common shock indicators, the only method of estimating shock pressures is through numerical modelling. However, correlations of shock pressures with the rock magnetic properties and with the microfractures of the rocks are well known [6–10,42]. Therefore, study of the rock magnetic properties and the microfractures in weakly shocked rocks may be an alternate method of estimating shock pressures.

The present study, therefore, aims towards studying the rock magnetic properties and the microfractures in weakly shock target rocks of two very different impact craters, namely Lonar crater, India and Lockne crater, Sweden. The presented results are compared with the known analogues in order to estimate a range of shock pressure. The estimates are then compared with the pressure values known from published numerical models.

Most methods of estimating the shock pressures, for example through sock indicators or through numerical modelling, give peak shock pressures. For example the shock indicators would reveal pressures experienced by the whole rock grains. Pertaining to the limitations of computing time, the smallest particles considered in numerical models are of the order of 10

cm [13]. Therefore, these estimations do not account for shock-induced processes occurring at smaller scale, especially at the grain interfaces. Interactions at the interfaces lead to changes in character of the shock waves that progress through it [18]. Understanding the essential role of grain interfaces in the formation of impact microstructures and the behaviour of shock wave is, therefore, an important problem, which is not yet well understood. In case of weak to moderate shock waves the interfaces may cause impedance leading to high local stress concentration [16,43]. Localized heating due to shock and resultant melting in pockets has been observed in meteorites [44–46], produced in shock recovery experiments [18,47], and theoretically explained [16,48]. However, no published reports are available demonstrating localization of both shock pressure and temperature (P-T) along grain boundaries and formation of high P-T polymorphs of plagioclase, in terrestrial impact target rocks.

Therefore, the following questions demand further investigations: “Is shock induced polymorphism at grain boundaries possible in natural terrestrial impact target rocks?” and “What is the correlation between the pressures and temperatures estimated through numerical models and those experienced at grain interfaces?”

1.3 Processes of Impact cratering and time evolution

An impact crater is formed when an extra-terrestrial body traveling at high velocity strikes the surface of the earth [30]. The impact produces intense shock waves radiating outward from the point of impact [30,49]. Commonly the shock waves exert pressures up to several hundred GPa and are responsible for formation of the impact crater [30]. Intense shock pressures at very high rate, typically in the order of $< 10\ ms^{-1}$, cause stresses far greater than elastic and plastic deformation limit of the terrestrial rocks and result in permanent deformation.

The formation of an impact crater by shock waves and its immediate modification by gravity induced processes is a complex and continuous event. However, the evolution is classically divided into three distinct stages; each dominated by different forces and mechanisms, namely: **contact and compression**, **excavation**, and **modification** (Fig. 1.1) [30,50]. The first stage, i.e., ‘contact and compression’, begins when the leading edge of the moving projectile

contacts the target surface. The stage is marked by transfer of one set of shock waves, outward from the interface into the target rocks, and reflection of a complementary set, back into the projectile [30,49]. The high intensity shock waves vaporize, melts and causes shock metamorphism in its medium of travel. Even for impacts between colossal objects, the contact/compression stage lasts only for a few seconds, and ends when the shock waves have passed through the projectile [51].

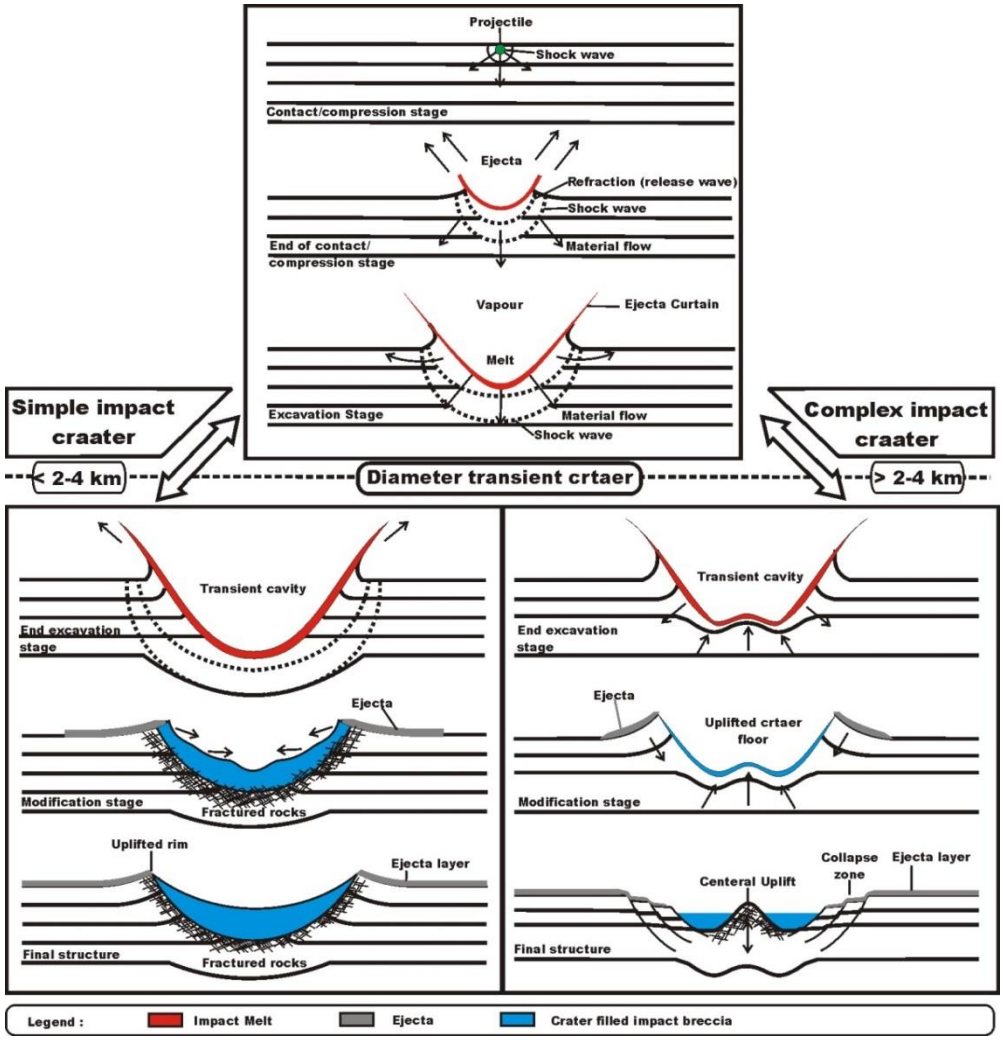

Figure 1.1. Cross-sections schematically demonstrating different stages of formation of an impact structure [21]. Craters with smaller diameter, in the range of 2 to 4 km, are commonly simple; however those with larger diameter have an unstable initial transient cavity, transforms under gravity and form complex impact craters. The first, contact/compression stage is similar in both cases, irrespective of the size of the crater.

During the second, i.e., 'excavation', stage the kinetic energy of the projectile is transferred completely to the target, and the radiating shock waves interact with the ground surface opening up the actual impact crater [26,30]. Simultaneously, a part of the initial shock-wave energy converts into kinetic energy, and the rocks involved are accelerated outward. As a

result a bowl-shaped depression, commonly known as the transient cavity or transient crater, is formed [30,52–54]. Eventually, the shock waves diffuse and weaken, and therefore are unable to further excavate or displace target rocks. Thus the growth of the transient crater ends.

The next stage, i.e., 'crater modification' begins as soon as growth of transient crater ends. Now, the crater is modified under the effect of gravity. The stage is marked by deposition of the ejected material and by the surges and resurges. This gravitational collapse forms the final crater morphology. If a central peak develops, in larger craters, the impact structure is classified as 'complex', for example the Lockne crater. However, no such peak is observed in the much smaller Lonar crater, which is, therefore, classified as a 'simple' crater.

1.4 Regional geology

1.4.1 The Lonar impact Structure, India

Lonar crater (19° 58' N, 76° 31' E; Fig. 1.2) is one of the youngest and best preserved impact structures on the Earth [5]. The 1.88 km wide simple impact crater was formed in the Deccan basalts about 50 ka ago [55,56] by a hypervelocity bolide traveling from east to west [57]. However, Jourdan et al. [58] estimated that the impact crater is about 570 ka old. The crater is about 1.88 km wide and 150 m deep from the rim, with an about 7-10 m deep shallow saline lake at its bottom. Below the crater floor, 30-100 m thick unconsolidated sediments are underlain by about 225 m thick impact breccia [59–61]. A continuous blanket of ejecta extends outward up to a distance of 1350 m from the rim crest [62]. The origin of the Lonar crater, volcanic versus impact, has been long debated [63–66]. With the discovery of shocked material, such as impact glasses in the impact breccia and shatter cones in basaltic fragments, its impact origin is now well established [55,67–69].

The ca 65 Ma old target Deccan basalts overlie the Precambrian rock formations and Palaeozoic-Mesozoic sedimentary rocks of the southern Indian Shield [62]. Five to six, 5 to 40 m thick, basalt flows are exposed in the crater wall (Tf0-Tf6; Fig 1.2). These basalts are

tholeiitic with high total Fe and CaO, but relatively low Al_2O_3 [70]. The massive and fine grained basalts, grade upwards into vesicular flow tops containing up to 20 vol. % vesicles of 1 to 20 mm diameter (e.g., [71]).

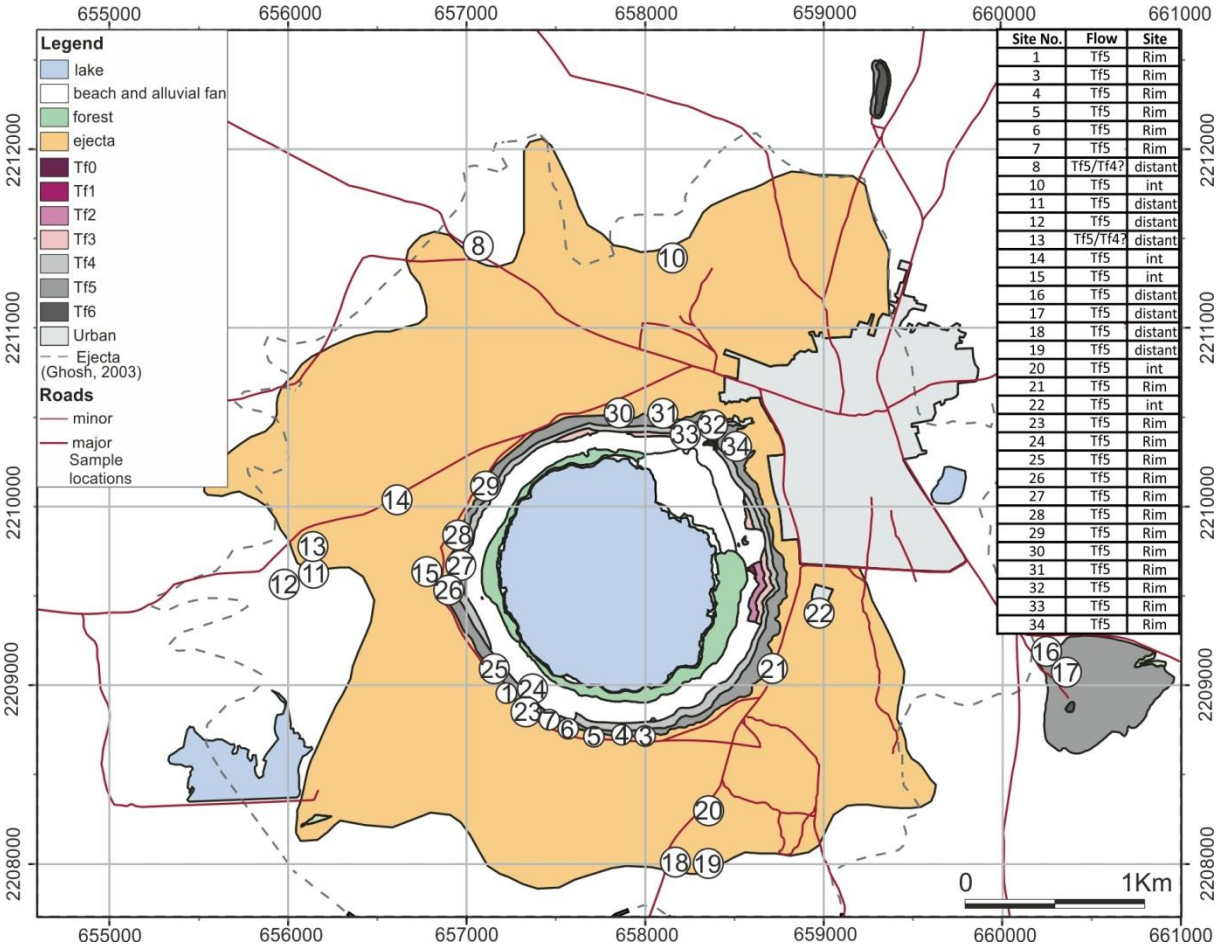

Figure 1.2. Map of Lonar Crater [5] with locations of sampling sites of this study. The grey line (dashed) outlines the edge of the continuous ejecta blanket determined by [72]. Lava flows: Tf0, Tf1, Tf2, Tf3, Tf4, Tf5, and Tf6. Easting (655000–661000) and Northing (2208000–2212000) coordinates are in Universal Transverse Mercator (UTM) (WGS84) meters. The table at the top-right corner describes the basalt flow and the distance, with respect to the crater, at which each sampling site is located.

1.4.2 The Lockne impact structure, Sweden

The Lockne impact structure (14°40'E, 63°00'N) is situated within and around the northern part of the lake Locknesjön (Fig. 1.3). The structure is marked by an about 7.5 km wide circular depression representing the inner crater, and a vaguely preserved 13.5 km wide outer crater, which were excavated into Proterozoic basement and overlying Cambro-Ordovician target rocks, during upper Ordovician time about 455 Ma ago [73,74]. The Cambro-Ordovician rocks

consisted of 30 m of Cambrian bituminous mudstone (Alum shale) and 50 m Ordovician lithified limestone (Orthoceratite limestone).

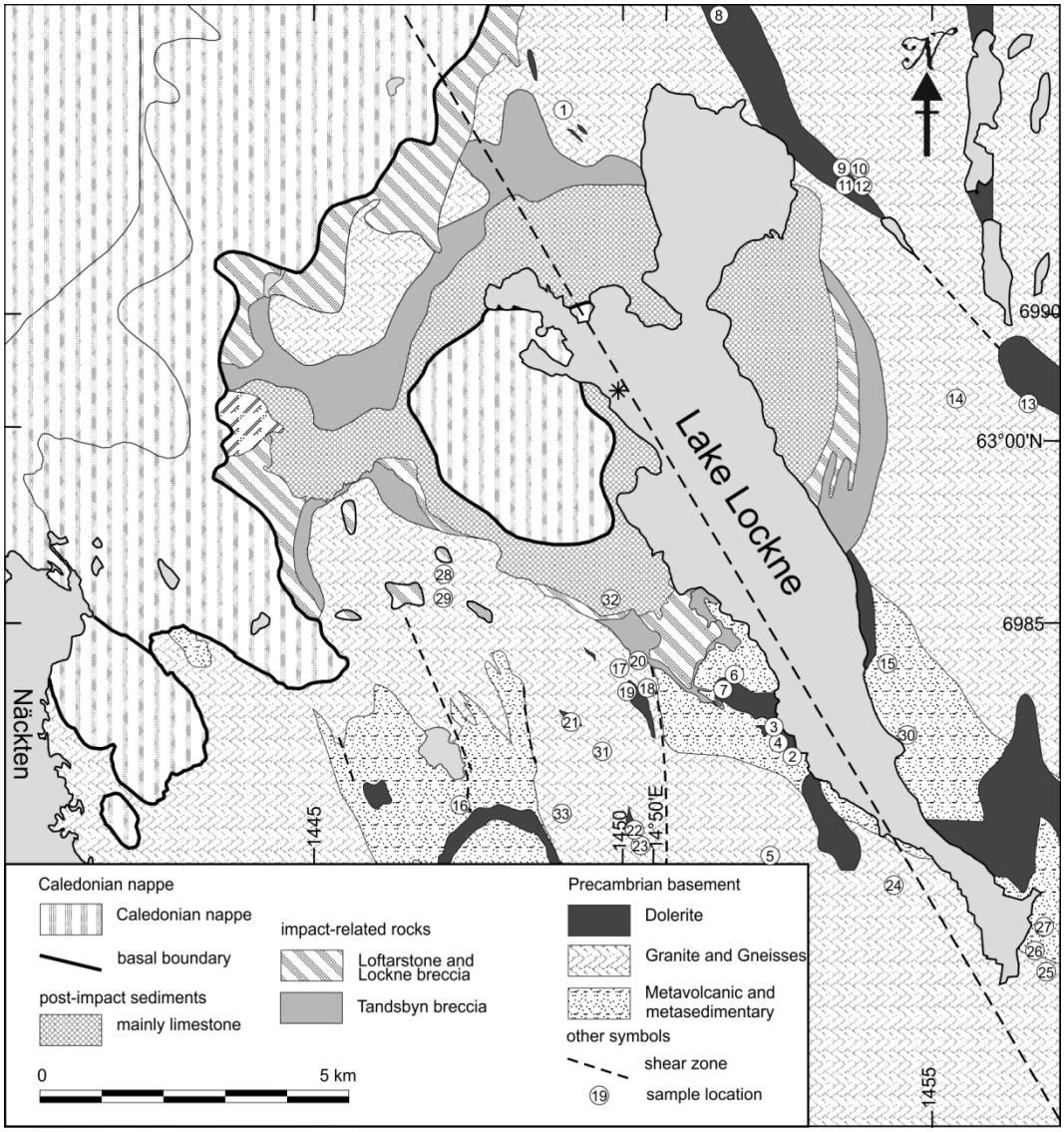

Figure 1.3. Geological map of the Lockne area in central Sweden showing major lithologies, faults, shear zones along with sampling site [75]. The centre of the Lockne impact structure is marked by an asterisk.

The oldest rocks in the Lockne area are early Proterozoic metavolcanic rocks, which are a part of the Trans-Scandinavian igneous belt, and locally show up to greenschist facies of Svecofennian metamorphism [73,76]. Several major, 1.82-1.80 Ga old NNW-SSE trending shear zones cut the metavolcanic rocks, which were later, at ca. 1.8 – 1.77 Ga ago, intruded by granites of the Revsund suite [77,78]. The crystalline bedrocks are cut by vertical faults, some of which run tangentially to the periphery of the crater and are the result of reactivation of

older shear zones (Fig. 1.3) [79]. Later, ca. 1.2 Ga, the entire sequence was intruded by dykes and sills known as Åsby dolerite, which typically dips less than 30° [80–83]. Gorbatschev et al. [84] suggested the dyke swarms in the area are part of the Jämtland complex of the Central Scandinavian Dolerite Group.

Sturkell et al. [85], through fluid inclusion studies, estimate overburden of the Lockne area in the order of ≥ 1.3 kbar suggesting a burial depth of ≥ 5 km. Moreover, the crystallinity index of the alum shale, conodont alteration index, and occurrence of laumontite suggest an upper limit of pressure, temperature (P-T) and corresponding depth of 3 kbar, 300°C and 10 km respectively [86].

The crater is situated at the present eastern erosional border of the Scandinavian Caledonian thrust front. However, the original nappes by far exceeded their present day extent [87]. The Cambrian Alum shale provided an ideal detachment for the eastward thrusting of the nappes over the Precambrian crystalline Baltoscandian platform [88]. In the eastern parts of the Caledonian deformation zone, the Precambrian crystalline basement is passive. The early Palaeozoic sediments (Jämtland super group), that detached, folded, and translated over the sole thrust at the alum shale level, mark the Caledonian Lower Allochthon [86]. While a nappe outlier of the Caledonides covers a part of the inner crater [86]. A part of the inner crater is also covered by resurge deposits, which are also observed outside of the crater. Lake Locknesjön and Quaternary glaciation related tills cover the eastern half of the crater. At the present day the Lockne crater is sub-circular and has a subdued morphology due to the preferred erosion of sedimentary strata at its centre, which according to gravity anomaly modelling demonstrates a weak uplift [74]. The subdued crater morphology may also be attributed to, up to 70 m high, crystalline brim [86]. The crystalline brim comprises of brecciated and fractures crystalline rocks [89]. Based on presence of Cambrian alum shale beneath the crystalline brim and the borehole data, Lindström et al. [89] suggested the brim to be rootless and therefore, interpreted it as overturned ejecta flap.

1.5 State of the art

1.5.1 Rock magnetics and fractures in the experimental craters

Studies on the target rocks of experimental and natural craters give a comprehensive report on the relationships of shock pressure with the magnetic fabrics and fractures. Results from these studies may be used as analogues for estimation of shock pressures, especially in weakly shocked rocks. A review of published studies on magnetic fabrics of experimental and natural craters reveals that in magnetite bearing rocks, maximum (k_1) or minimum (k_3) susceptibility axes reorient subparallel with the shockwave propagation direction at pressures in the order of 0.5 - 3 GPa or ≥ 3 GPa, respectively [6,7,10]. At much higher shock pressure, ≥ 10 GPa, increase in coercivity has been reported, which is attributed to permanent modification of the magnetite crystalline structure [10].Titanomagnetite bearing shocked basalts in Lonar crater rim, that have experienced shock pressures ≥ 3 GPa, show a decrease in magnetic anisotropy by about 2% [90].

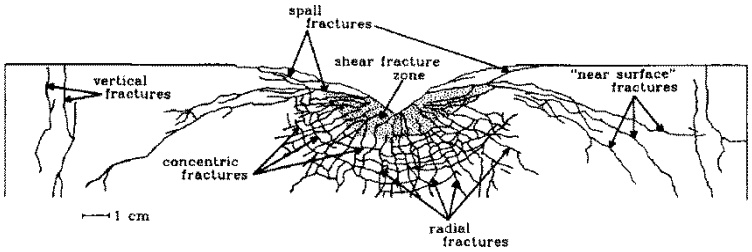

Figure 1.4 (a) Cross section of experimental crater [92], demonstrating the radial, concentric, and near-surface fractures, which occur below the near-surface zone.

Studies from the natural craters report three types of impact generated fracture sets, namely (i) radial, (ii) concentric and (iii) conical [e.g., 62,91]. These three types of fracture sets are also observed during shock experiments on rocks [42,92] and ice [93]. Several authors interpret the origin of radial and concentric fractures with the help of theoretical models, for example those by Field [94], Fourney [95], Selberg [96], Shibuya and Nakahara [97] and Swain and Hagan [98] and compare them to previous experimental observations, such as those by Melosh [99] and Sammis and Ashby [100]. The comparisons unambiguously demonstrate that the radial fractures form during the compressive phase due to accumulation of tensile stresses at mechanical flaws [42,92,100] and the concentric fractures form due to sudden pressure release during the decompressive phase, perpendicular to the shock wave propagation direction [42,96,97,101]. Hörz [9] and Lambert [8] suggest that, in general, a systematic relationshionship between the impact generated fractures and the shock pressures is valid

only in the range of 0.2 – 20 GPa. The impact origin of the fractures may, therefore, be confirmed by investigating their orientations with respect to the impact crater and if the microfractures are indeed generated by shock wave we may quantify the shock pressures to be in the range of 0.2 – 20 GPa.

However, the chronology of the radial and the concentric fractures has not yet been well illustrated. Several studies have 'predicted' that the formation of the radial fractures, during the compressive phase 'may be' followed by the formation of the concentric fractures during the decompressive phase of the shock wave [42,92,93]. However, no petrographic or other visual evidence was supplied. The question of the chronology of the radial and concentric fractures was also not clear on the photographs of microcraters developed on solar panels of space craft [figure 4a, 6a in 102]. Graham et al. [102] and other authors such as Kumar and Kring [91] conclude from the photographs that in some cases the radial fractures predate the concentric fractures while in others the concentric fractures predate the radial fractures. Through microscopic evidences we, therefore, attempt to comment upon the chronology of the radial and concentric microfractures and relate them to the compressive and decompressive phase of the shock wave.

1.5.2 The Lonar crater, India

Review of published literature reveals comprehensive information on the structure, magnetic fabrics and paleomagnetic properties of the target basalts. Misra et al. [57] and Arif et al. [90] studied the magnetic fabrics of the target basalts around the Lonar Crater. They suggest that the shock waves overprinted the primary magnetic fabrics such that the minimum susceptibility axes (k_3) was reoriented subparallel with the down range direction of the impact, East-to-West. Moreover, they demonstrate the magnetic anisotropy of the shocked basalts, in comparison to the unshocked ones has decreased by 2%. This interpretation, when viewed in light of the experimental studies on the Lonar basalt samples by Nishioka et al. [7] and Nishioka and Funaki [6] and other rocks by Gattacceca [10] imply that the crater rim basalts should have experienced at least 3 GPa and probably ≥ 10 GPa peak shock pressures. The pressure estimates are based on the observations that, experimentally applied shock pressures in the range of 0.5 to 3 GPa causes in Lonar basalt samples reorientation of

maximum susceptibility axes (k_1) parallel with the direction of shock. At shock pressures above 3 GPa, k_3 is the favored axis experiencing similar reorientation [6,7].

2D numerical simulation of the Lonar impact by Louzada et al. [12] does not support the high levels of shock pressure in the Lonar crater rim basalt. Their modelling shows that the shock pressure at the present day crater rim was of the order of < 1 GPa [12]. The thick breccia lens below the crater floor and a small fraction of the ejecta may have, however, experienced pressures greater than the Hugoniot elastic limit of basalt, ~5 GPa [12,103].

Existing reports on the NRM studies are also equivocal. For example, Arif et al. [90] demonstrate that the mean HC_HT component of shocked basalts from the Lonar crater rim, D = 120.5°, I = + 34.2°, are different from paleo-Deccan directions. They interpret the deviating NRM direction to be a consequence of unidirectional impact generated magnetic field that modified the magnetization vector. They, therefore, inferred that the basalts acquired an HC_HT magnetization component, systematically oriented in the uprange direction of the impact. By contrast, Louzada et al. [12] show that in the crater rim basalts the high coercivity component (D = 156.0°, I = + 66.5°, k = 10.5, α_{95} = 8.6°, for flow 5) is similar to those in the unshocked basalts as calculated by Vandamme et al. [104] (D = 157.6°, I = +47.4°, α_{95} = 1.9°). They further suggest that the low coercivity components of NRM in the crater is rim similar to present day magnetic field respectively and attribute it to the post-impact viscous remanent magnetization and/or chemical remanent magnetization [12].

Published studies on the fractures in the rim of the Lonar crater are also contradicting. Kumar [62] attributes the development of radial, concentric and conical mesoscopic fractures around the Lonar crater to the impact event. This interpretation is in agreement with the radial and concentric fractures, experimentally demonstrated by Polanskey and Ahrens [92], and Ai and Ahrens [105]. A diametrically opposite hypothesis for the origin of fractures is proposed by Maloof et al. [5]. They argue that the fractures in the Lonar target rocks are not impact related, but owe their origin to cooling of basalt. They demonstrate that the fracture patterns in the crater rim are similar to those in the unshocked basalts. In this study, microfractures in crater rim and outside are used for addressing the issue of origin of the microfractures and compare them to known analogues for estimation of shock pressure.

1.5.3 The Lockne crater, Sweden

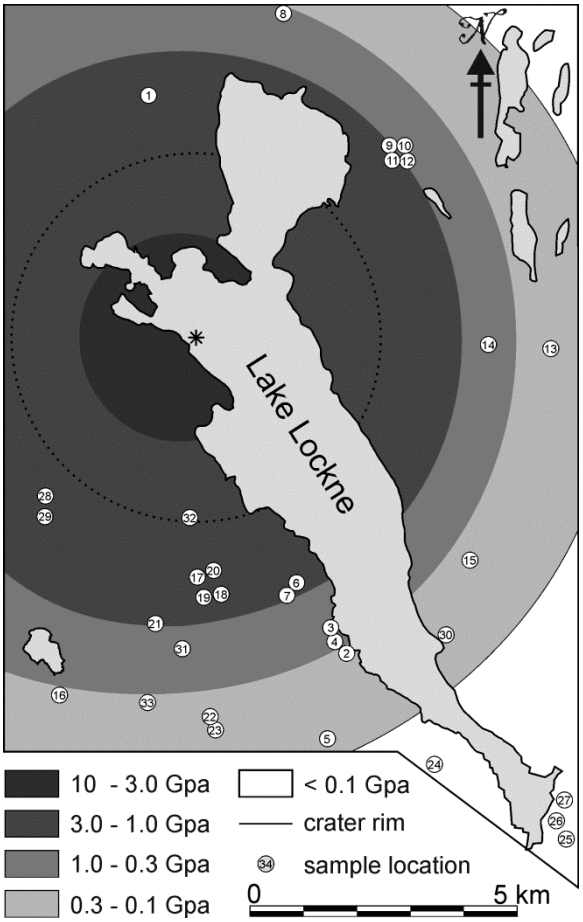

Figure 1.5 Map showing the estimated shock pressures at sampling site of crystalline basement rocks and in the area. The shock pressures are estimated after Lindström [13].

Magnetic fabric and microfracture studies have not yet been attempted on the Lockne target rocks, however several studies demonstrate the processes of crater formation. Recent numerical modelling implies formation of the Lockne crater in a 500-700 m deep sea due to an oblique impact (45^{o} from horizontal) of an about 600 m wide projectile, which was travelling at about 15 km/s from the east [13,15,106]. The shock pressures in Lockne varied from over 100 GPa at the point of impact to 0.5 GPa at a distance of approximately 5 km (Fig. 1.5) [13]. The impact blasted away the sea within about 6 km from the impact site. The top of the Orthoceratite limestone that remained in situ was strongly stirred by the water, and by pelting from granitic hypervelocity ejecta. This stirring created a monomictic limestone breccia called Ynntjärnen Breccia [89,107,108]. The impact also excavated rocks from inside the crater, which were later deposited as impact ejecta. The brecciated basement ejecta are called Tandsbyn Breccia and those deposited by water resurge are called Lockne Breccia and Loftarsten [79,109]. The final stage of cratering is marked by an oceanic resurge wave. The wave had a strong outgoing flow along the seafloor, causing excavation followed by relatively weaker inward depositional flows [89,107].

The studied basement rocks (metavolcanic, granite and dolerite) lie between the 7.5 km wide inner crater and 13 km wide outer crater of Lockne impact structure. The rocks do not show the common shock features such as PDF, polymorphism, amorphization, that may be used as indicator of shock pressure. They fall in shock metamorphic ‘stage 0’ according to the

definitions suggested by Stöffler [110]. Therefore, the present study employs magnetic and microscopic lines of evidence to investigate the effects of shock. Orientation of magnetic susceptibility ellipsoids and geometry of microfractures is used to determine their origin. The magnetic fabrics and microfractures are compared with published, natural and experimental, analogues to estimate a range of shock pressure, which discussed in the context of the pressure range that is suggested by Lindström et al. [13] employing numerical simulations.

1.6 Methodology

For estimating the shock pressures and understanding the origin of magnetic fabrics and microfractures in the target rocks, the basalts at Lonar and the crystalline basement rocks at Lockne, are studied. The situation of the outcrops and the sampling details are described under the heading 'Sampling of the outcrops'. The following text describes the methods that were used during the study. Transmitted and reflected polarized light microscopy (PLM), scanning electron microscopy (SEM), transmission electron microscopy (TEM) are described under 'microscopy', which include investigations related to the microfractures and the magmatic foliation, i.e., shape preferred orientation (SPO) of plagioclase. Temperature dependent low-field magnetic susceptibility (χ-T), anisotropy of magnetic susceptibility (AMS), field dependence of magnetic susceptibility, hysteresis, and natural remanent magnetization (NRM) investigations are grouped under 'rock magnetic methods'. The micro-Raman spectroscopy is described under the heading 'spectroscopy'.

1.6.1 Sampling of the outcrops

At Lonar impact structure

Six 10 to 30 m thick basalt flows (Tf0-Tf5) are exposed in the inner crater wall (cf. [5]). Each flow is separated from other by discontinuous flow top autobreccia consisting of red and green paleosols, chilled margins and vugs filled with secondary chlorite, zeolite, quartz and limonite. The basalt flows are massive, vesicular and amygdaloidal, and may be classified as quartz-normative tholeiites of high total iron and CaO, and lower Al_2O_3 and MgO [70]. Ghosh and Bhaduri [111,112] remark that, all basalt flows have a common mineralogy and texture,

except for minor differences in abundance of plagioclase phenocrysts, glass and opaque phases.

Out of the six basalt flows in the inner crater rim only flow Tf5 is continuously exposed, whereas the underlying flows are sometimes covered by basalt debris, soil and vegetation (cf. [62]). Slumping is also common in the lower flows [62]. Along the rim crest, Tf5 is recumbently folded and variably brecciated, with semi-intact beds preserving a reverse basalt stratigraphy (cf. [5]). Hence the 19 sampling sites in the inner crater wall were restricted to the normal limb of the flow Tf5, which is exposed few meters below the crater rim. Several normal faults are observed in the inner crater. The sampling was, carefully done from the in-situ footwall of these faults. Away from the crater rim a thin but continuous blanket of ejecta overlies the lava flows. Sampling at distances of few hundred meters away from the crater rim was therefore, restricted to 5 sites within natural and artificial pits in which flow Tf5 was accessible. 8 sites were sampled at a distance of 1.4 -2.5 times R_C (crater radius) from the crater center (Fig. 1.2). Out of these, 6 (site 11, 12, 16, 17, 18 and 19) are in Tf5, while the rest 2 sites may be in Tf5 or Tf4. However, since the unshocked basalt are subhorizontal flows with consistent mineralogy, having only minor variations [60,111], samples from all 6 sites should have similar pre-impact petrographic texture, rock magnetic properties and microfracture orientation, if any. Block samples or at least 5 drill cores, oriented using magnetic compass, were collected from each site. A minimum of 5 cylindrical cores (25.4 mm diameter and 22 mm height) were drilled from each block samples in the workshop of Department of Geology and Geophysics, IIT-Kharagpur, India.

At Lockne impact structure

27 sampling sites were selected around the crater, from where oriented block samples and drill cores, oriented using magnetic compass, were collected. Cylindrical cores (25.4 mm diameter and 22 mm height) were drilled from the block samples in the workshop of institute of Applied Geology, KIT, Germany. At least 5 cylindrical cores were obtained from each sample.

Four sets of thin sections were prepared from each sample collected at Lonar and Lockne impact structures, viz. (i) horizontal, (ii) vertical sections, (iii) along a plane along the magnetic

foliation and (iv) along a plane perpendicular to magnetic foliation but parallel to magnetic lineation. The vertical and horizontal thin sections were used for the studying the microfracture orientations, while the thin sections prepared with respect to the principal planes of the AMS ellipsoid were used for studying the correlation between the magnetic minerals and the rock fabrics. All thin sections were studied to understand the mineralogy and petrofabrics of the rocks.

1.6.2 Microscopy

Light microscopy

Transmitted and reflected light investigations were done to understand the mineralogy and texture of the rocks on an orthoplan microscope with maximum magnification of 600X. The magnetic minerals were distinguished from other opaque phases by coating the thin section with the ferro-fluid. The ferro-fluid, produced by Institut für Angewandte Polymerchemie FH Aachen, is colloidal solution of ultrafine magnetite particles that stains the magnetic minerals brownish-red.

Oriented sub-horizontal and sub-vertical thin sections were used for geometrical analysis of the microfractures. At least 200 individual fracture trends were recorded from each thin section and were plotted in rose diagrams. In Lockne, the area was divided into sectors and the fractures recorded from all the samples in a sector, were plotted together. This helped in establishing a relationship between the microfracture trends and the shock pressures.

Scanning electron microscopy

For SEM, the rock-thin sections, were mounted on an aluminium holder and were coated with a fine conductive nano-carbon layer. SEM studies were carried out with a LEO 1530 electron microscope of Gemini instrument. During the studies secondary (SE) and backscattered (BSE) electrons were recorded. Simultaneously an energy-dispersive X-ray (EDX) attachment, Noran System 6 Thermo Fischer, was used for qualitative and quantitative elemental analysis of particular grains and for elemental mapping of the thin-section.

Transmission electron microscopy

About 20 µm thick rock thin-sections bonded to glass plates were mounted on aluminium holder, similar to SEM, using conductive carbon adhesive. A Nanocarbon (Plano carbon N625 of PLANO GmbH, Wetzlar) conductive paste was used to mark the area of interest and, therefore, allow conductive contact between the rock thin section and the aluminium holder (Fig. 1.6 a, b). Conduction between the rock sample and the aluminium holder is critical for providing a stable beam current and reducing the sample charging and its amorphization.

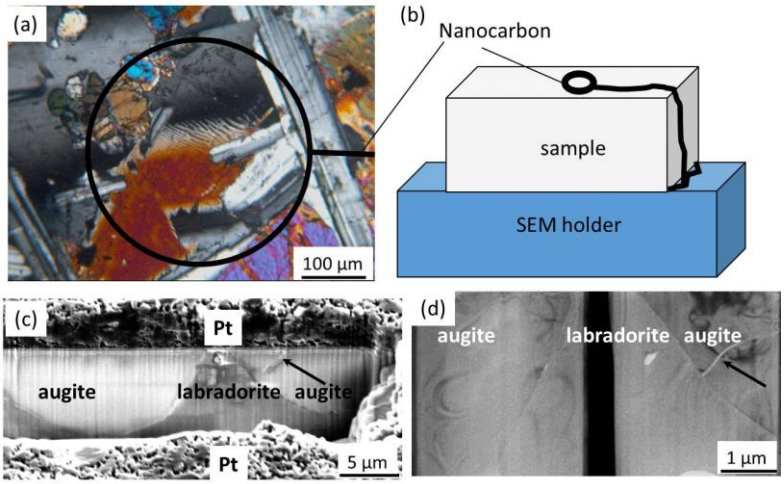

Figure 1.6. Preparation and analysis of a TEM section. (a) Light micrograph of a dolerite thin-section. The area of interest, around augite-labradorite lamellae, is encircled by conductive carbon paste (black circle). (b) Conductive contact, between the rock thin-section and the aluminium FIB sample holder, is established. (c) 'TEM-1' section, before being removed from the rock thin-section, which is covered by platinum (Pt). Vertical striations observed on the surface of TEM-section after FIB milling, but before the final polishing. The section is thicker towards the bottom, and therefore the straight augite-labradorite lamellae interface seems curved. (d) Overview TEM image of the 'TEM-1' section showing the interface. In (c) and (d) black arrow points to the impact generated microfracture in augite. The microfractures cease in labradorite.

Sections for TEM analysis were obtained from the thin-sections using a FIB station, FEI Dual Beam Strata 400S with a Ga+ cathode. Here the area of interest was coated with a 3 µm thick conductive Platinum layer. Thereafter, TEM-sections were cut from the rock thin-section by a 30kV, 6.5 nA Ga ion beam. The TEM-sections were later thinned by a 30kV, 26 pA Ga ion beam and two to three, 5 to 50 nm thick, windows were prepared to check FIB induced damage and amorphization. In the final step, the TEM-sections were polished with a 5kV (71 pA ion current) beam for several minutes. The step is essential to remove the crust of the TEM-sections were, which is commonly be damaged by the ion beam. The polishing was competent as the augite, present above lingunite, and therefore closer to the ion beam source is crystalline. Since, the lingunite and the amorphous phase are present below the crystalline augite, possibility of FIB induced amorphization is slim. The TEM studies were done using a

200 keV Philips CM 200 FEG/ST by Dr. Boris Reznik. He also analysed the Selective area electron diffraction (SAED) patterns and helped in interpretation of the results.

It is well known that Na-plagioclase and lingunite, under high energy electron beam, may transform into an amorphous phase [e.g., 113]. Amorphization was avoided by using a cold stage that was cooled by liquid nitrogen, and smaller exposure time, about 10-20 ms. A condenser aperture of 100 µm at a spot size of ≥ 300 nm was used for initial selective area electron diffraction image and general TEM investigations. Usually much higher energy is transmitted to the sample during high resolution TEM (HRTEM) investigations. Therefore, for HRTEM the beam was first focused at a location away from the area of interest and only then the investigations were carried out.

Shape preferred orientation of plagioclase

In Lonar, a comparison between the magnetic fabrics (AMS) and the magmatic fabrics (shape preferred orientations of plagioclase; SPO) was done to test whether both are interrelated [e.g., 114,115,116] or if the AMS is reoriented due to some secondary process, such as shock metamorphism and/or hydrothermal alteration. Two samples were selected that represented the rocks from the crater rim in the downrange (sample 1) and the uprange (sample 34) direction of the impact (Fig. 1.2). Another sample (sample 19) was selected from the background flow that according to published data [12,57,90] has not been shocked (Fig. 1.2). These samples were selected since they show larger plagioclase grain size compared to other samples, and they were less strongly weathered rendering magmatic fabric analysis more precise. Three perpendicular polished sections from each sample were made. For better comparison between magnetic and magmatic fabrics, same cylinders were used for AMS and thin section studies. A high resolution monochromatic camera was used to capture oriented photomicrographs. To increase the grain count, several photomicrographs, were captured in a continuous and overlapping fashion, which were later stitched together using Adobe Photoshop (Fig. 1.7a). In each section, the shape fabric was extracted using the intercept method of Launeau and Robin [117] (see http://www.sciences.univ-nantes.fr/geol/UMR6112/SPO/index.html), which is based on analysis of boundary orientation distribution of objects (Fig. 1.7b, c, d and Table 1.1).

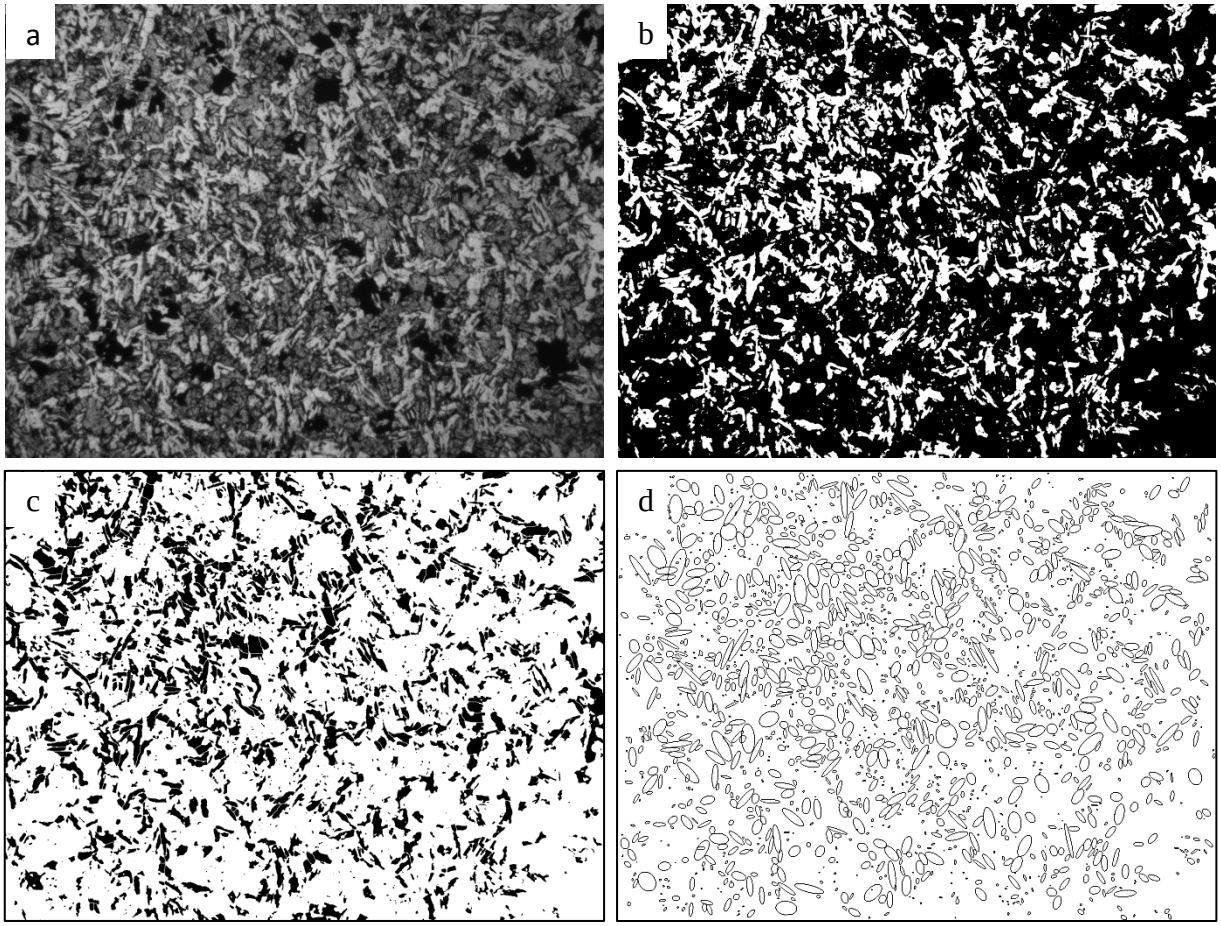

Figure 1.7. Steps of magmatic fabric analysis from thin sections. (a) Grayscale photomicrograph from a monochromatic camera. (b) The image is thresholded into b/w such that the plagioclase grains in white, contrast against black background of mafic minerals. (c) The image is smoothened to get rid of smaller grains, holes, etc. The image is then inverted. (d) ImageJ is used to fit ellipse in all the grains.

Table 1.1. Example results of "particle analysis" through ImageJ. "Count" is the number of particles analysed. "Total area" is the sum of the area covered by the analysed grains. "Average size" is average size of the ellipse. The mean length of the major and minor axis and the mean angle of the major axis from the vertical are represented by "major", "minor" and "angle", respectively. The lengths and angles are in pixels and degree, respectively.

Count	Total Area	Average Size	Major	Minor	Angle
1847	1120482	606.65	33.907	14.831	88.77389984

1.6.3 Rock magnetic studies

Fundamentals of rock magnetism

Magnetic anomalies are extensively used to map geologic structures and metamorphic terrains. However, the correlation between shock and magnetic properties/anomalies is not

yet fully understood. In order to understand the results and appreciate the interpretations of the thesis, an introduction to the fundamentals of magnetism is indispensable. Detailed textbooks about rock magnetism have been written by Soffel [118] Dunlop and Özdemir [119], Butler [120] and Dubey [121].

The magnetization of a material, as a response to the applied external magnetic field is given by the following relation:

$$J = \chi . H$$

Where H is the external magnetic field, χ is the magnetic susceptibility, which for rock magnetic purposes is volume specific and J the magnetization. χ is a material constant representing magnetizability of a substance, which in turn determines the amount of induced magnetization, J_i. The magnetization remaining in the material after removal of an external magnetic field is the remanent magnetization (M_{rs}). The Königsberger ratio Q allows one to estimate the dominance of the induced or remanent magnetization through the relation:

$$Q = \frac{M_{rs}}{\chi^H}$$

Similar to the induced magnetic field, generated when electric current flows through a conductive material, an electron also produces a magnetic field during its motion around the atomic nucleus. The vector sum of the magnetic moments generated by the rotation and revolution of the electron is the effective magnetic spin moment, which is commonly indicated by a magnetic field vector. In case of *diamagnetic* materials all electrons in an atom have paired spins, i.e., there are equal numbers of spins moments in opposite directions such that the net vector sum is zero. However, the *paramagnetic* materials have atoms containing one or more unpaired electrons, and, therefore, have a net magnetic moment, which is a multiple of Bohr magneton, $\mu B = 9.27 = 10^{-24}$ Am i.e., spin magnetic momentum of an electron. The paramagnetic materials have no permanent magnetic moment because when an external magnetic field is applied the magnetic moments are aligned in the direction of the field, and as soon as the field is removed the moments regain their original position. The *ferromagnetic* minerals are characterized by strong interactions of magnetic moments which results in a net magnetic ordering and a magnetic dipole moment, even without the application of an external magnetic field. The magnetic dipole moment is temperature dependent, as beyond the Curie temperature (T_C), the spins disorder and the material

becomes paramagnetic. Several different types of ferromagnetic arrangements are possible within a crystal lattice. For example, oxides have typical antiferromagnetic ordering, where the magnetic moments of oxygen atoms are aligned in an antiparallel fashion i.e., the spin-spin interactions, resulting, in a zero net magnetic moment of the whole crystal lattice. However, in case of a ferrimagnetic arrangement, spins of unequal strength demonstrate an antiferromagnetic ordering, which results in a unidirectional strong net magnetic moment. A region within the material marked by parallel coupling of spins from neighbouring atoms, such that all individual spin momenta are pointing in the same direction, is commonly known as magnetic domains.

In rocks, four different magnetic domain states occur depending upon the grain size and shape. Multidomain (MD) grains contain uniformly magnetized multiple magnetic domains, which are have variable bulk magnetic vector orientation. On application of an external magnetic field, the magnetic domains with vectors aligned approximately in direction of the applied field grow in size at the expense of other domains and therefore the net magnetic moment produced may be attributed to the movement of the domain walls. As the field is removed the domains approximate, but never completely regain, their original shape and size. This common phenomenon is attributed to the fact that in an applied field the domain walls stabilize in certain energetically favourable positions, depending upon the lattice imperfections and internal strains, and a small net magnetic moment always remains. In MD grains, weak magnetic fields are sufficient to reorient the domain walls and remove the magnetic moment; therefore the MD grains are magnetically soft. Single domain (SD) grains are much smaller and have only one uniform magnetic domain with more stable walls. The only process of changing the magnetization is by rotating the remanent magnetization, Mrs, therefore rendering high remanence stability and making SD grains very efficient magnetic remanence carriers. Grains with size between the SD and MD are known as Pseudo-single-domain (PSD) grains. PSD grains, generally, have few magnetic domains, marked by magnetic behaviour similar either to an assemblage of SD grains or to a MD grain with few magnetic domains. The fourth type of magnetic domain state is the super paramagnetic (SP) grains, which are unable to preserve a magnetic moment because the magnetic relaxation time is very small, <100s. Magnetic relaxation time is referred to as the natural exponential decay of remanent magnetization in SD grains with time.

Magnetic domains reduce the overall free energy associated with the magnetic ordering. Three important phenomena are employed to describe the behaviour of magnetic ordering. First is the, magnetocrystalline anisotropy, which determines the direction of magnetization, and commonly correspond to the “easy direction of magnetization” also known as the “easy magnetic axis”. This axis represents a particular crystallographic direction, which is easier to magnetize than others. Second are the, “magnetostatic effects”, which arise from Coulomb interactions between the free surfaces or domain boundaries. The resulting magnetostatic energy depends on the magnetic domain distribution and crystal shape. When the magnetic moments in a domain are aligned in opposite directions the magnetostatic energy is least. Third is the, “magnetostriction”, which describes the phenomenon of, change in shape of a magnetic mineral during magnetization due to the shift and rotation of magnetic domains. All three phenomena influence the magnetic domain structure, which is generally arranged such that the overall free energy is least.

Temperature dependent low-field magnetic susceptibility

For investigating the magnetic mineralogy of the basalts, temperature dependent low-field magnetic susceptibility (χ-T) experiments were carried out. The measurements were done in two runs on powdered samples using a Kappabridge (KLY-4S) (AGICO, Brno, Czech Republic). For low temperature (-194°C to room temperature) measurements the Kappabridge was equipped with CS-L (AGICO, Brno, Czech Republic) cryostat and the sample was cooled to -194°C using liquid nitrogen, which was then flushed out of the holder using a blast of argon. The bulk susceptibility of the sample was measured as it gradually warmed up to the room temperature. For high temperature (40°C to 700°C) measurements, the Kappabridge was equipped with a CS-2 furnace (AGICO, Brno, Czech Republic). The sample was first heated from 40°C to 700°C (at a rate of 10°C min^{-1}) and was then cooled back. The bulk susceptibility was measured during the entire cycle of heating and cooling. An argon environment (flow rate of 60 ml min^{-1}) was maintained in the sample holder to minimize the risk of oxidation of the sample while heating. The temperature of the sample was measured with a Pt resistance thermometer, placed within a distance of 1 mm. According to the manufacturer, the thermometer (JUMO) is accurate within ± 1°C at temperatures up to 150°C and within ± 3°C in the range of 150 – 700°C. The first derivative curve of the χ-T measurements was calculated

and the Curie temperature and Verwey transition temperatures were determined, as well as reversibility of the χ-T curves was tested.

Field dependence of magnetic susceptibility

Field dependence of magnetic susceptibility of basalts may reach up to 20% for measurements in 30 and 300 A/m AC field amplitude depending on titanomagnetite composition [122]. For testing the field dependence of AMS in Lonar basalts, nine cores (with known mineralogical and magnetic domain properties) collected from three different sites were selected and AMS was studied under the applied field of 50 A/m and 300 A/m. Further three samples, with known mineralogical and magnetic domain characteristics were selected to test the field dependence of magnetic susceptibility and k_m versus applied field was plotted. The field dependence parameter χ_{Hd} ($\chi_{Hd}[\%]=[(\chi_{300A/m} - \chi_{50A/m})/\chi_{300\ A/m}])*100$) for the bulk susceptibility and anisotropy of AMS, P'_{Hd} ($P'_{Hd} = [(P'_{300A/m} – P'_{50A/m})/P'_{300\ A/m}])*100$) were also calculated (modified after de Wall [123]).

Hysteresis parameters

Magnetic grain size distribution of the ferrimagnetic minerals (single domain-SD, multidomain -MD and pseudo-single domain- PSD components) was determined from hysteresis, backfield and acquisition of isothermal remnant magnetisation (IRM) curves using a Variable Field Translation Balance (VFTB) at the Department of Earth and Environmental Sciences, Munich University. During the hysteresis measurements on the VFTB, a magnetic field is applied and successively increased until all magnetic moments are aligned along the direction of the field and saturation remanence (Ms) is reached. Then after reducing the applied field to zero, a remanent magnetization (Mrs) remains in the sample. In order to completely remove this magnetization (Mrs = 0) a field in opposite direction to the initial magnetizing field is applied. The field strength of this opposite field, which is sufficient to reduce Mrs to 0, is referred to as coercive force (Hc), whereas the field necessary to reorient one half of Mrs into the opposite direction is called remanence of coercivity (Hcr). Both parameters are expressions of the coercivity, which is a measure of the magnetic hardness. The IRM curves were generated through the application of stepwise increasing uniaxial field on the sample. Both the saturated and non-saturated IRM acquisition curves were effectively modeled into their individual

coercivity contributions according to the shape of the curves and by calculating the median destructive field (MDF) of each sample [e.g., 124,125].

Natural remanent magnetization

In order to understand the history of magnetisation of the basalts, natural remanent magnetization (NRM) was studied. Depending on the history of the rock, NRM may have several components, such as: Thermoremanent magnetization (TRM), common in magmatic rocks, is acquired when a magnetic mineral is cooled down to below its T_C, and represents the direction of the Earth's magnetic field at that time. Remanent magnetization acquired during growth of secondary/new mineral either through chemical alteration or precipitation from solutions is referred as the chemical remanent magnetization (CRM). Exposure to shock wave, may lead to loss of existing and acquisition of new remanence, which is known as shock remanent magnetization (SRM). SRM generally represents Earth's magnetic field at the time and place of shock. Variations in thermal conditions may alter pre-existing NRM and may induce a new viscous remanent magnetization (VRM).

NRM was measured with a JR5A spinner magnetometer (AGICO, Brno, Czech Republic). Alternating field (AF) demagnetization was performed in peak fields up to 160 mT with a MI AFD 1.1 from Magnon International. During AF experiments, a certain field is applied on the sample and after removal of the field, remanence is measured. This procedure is repeated and in every step intensity of the magnetic field is successively increased. The demagnetization was plotted in orthogonal vector diagrams, and characteristic directions were determined as line or plane data using principal component analysis [126].

For magnetic fabric studies the AMS was measured using a KLY-4S Kappabridge (AGICO, Brno, Czech Republic). The data were processed through the Anisoft 4.2 software, and plotted in lower hemisphere stereographic projections. Following AMS parameters were used: mean susceptibility (k_m)= (k_1+k_2+k_3)/3; corrected degree of magnetic anisotropy (P') = exp √[2(η_1-η_m)^2+(η_2-η_m)^2+(η_3-η_m)^2]; mean of shape factor of AMS ellipsoid, (T_{mean}) = (2η_2-η_1-η_3)/(η_1-η_3); here η_1=ln k_1; η_2=ln k_2; η_3=lnk_3; η_m=(η1. η2. η3)$^{1/3}$ k_2; and k_1, k_2 and k_3 are the maximum, intermediate and minimum susceptibility axes of AMS ellipsoid [127]. T_{mean} was plotted against P' [128] and k_m was plotted against P' to understand the relationship among them.

1.6.4 Spectroscopy

Raman spectroscopy provides characteristic fundamental vibrations that are employed to understand the molecular structure. It involves the study of interaction/transfer of radiation, (photon energy) with the molecular vibrations, and thereby changing its vibrational state. Raman spectroscopy is a two-photon inelastic light-scattering event. The incident photon has higher energy than the vibrational quantum energy. During interaction, the incident photon loses part of its energy to the molecular vibration and is scattered back with the remaining energy as a photon of reduced frequency. In the case of Raman spectroscopy, the interaction between light and matter is an off-resonance condition involving the Raman polarizability of the molecule.

The Raman vibrational bands are characterized by their polarizability or polar character (intensity), frequency (energy), and band shape (environment of bonds). The vibrational energy levels are unique to each molecule, therefore, Raman spectrum provides a unique fingerprint of a particular molecule. The frequencies of these molecular vibrations depend on the masses of the atoms, their geometric arrangement, and the strength of their chemical bonds. The spectra provide information on molecular structure, dynamics, and environment.

Raman spectroscopy describes the nature of the interaction of an oscillating electric field using classical arguments [129]. Figure 1.8 schematically represents the basic mathematical description of the Raman Effect. The electromagnetic field will perturb the charged particles of the molecule resulting in an induced dipole moment:

$$\mu = \alpha E$$

where α is the polarizability, and E is the incident electric field of the radiation, which is oscillating at a frequency ν_0, which can induce an oscillation of the dipole moment, μ, of the molecule at the same frequency, Figure 1.8a. The polarizability, α, of the molecule has a certain magnitude, that may slightly vary with time at much slower molecular vibrational frequency ν_m, Figure 1.8b. The result, Figure 1.8c, depicts an amplitude modulation of the molecular dipole moment oscillation, which mathematically, can be resolved into three steady amplitude components with frequencies ν_0, $\nu_0 + \nu_m$, and $\nu_0 - \nu_m$, Figure 1.8d. These molecular dipole moment oscillations can emit scattered radiation at same frequencies called Rayleigh,

Raman anti-Stokes, and Raman Stokes frequencies. If a molecular vibration does not cause a variation in the polarizability, there would be no amplitude modulation of the dipole moment oscillation and no Raman Stokes or anti-Stokes emission.

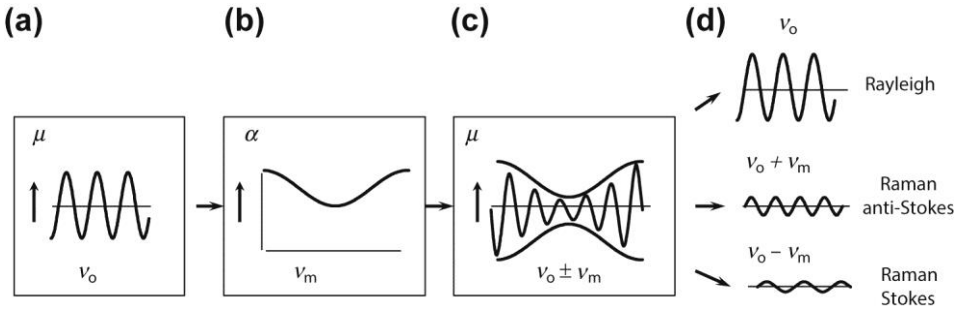

Figure 1.8. Schematics of Rayleigh and Raman scattering [after 130]. (a) The incident radiation causes the induced dipole moment of the molecule to oscillate at the photon frequency. (b) The molecular vibration may change the polarizability, α, which in turn changes the amplitude of the dipole moment oscillation. The result, (c), is an amplitude modulated dipole moment oscillation. (d) Shows the steady amplitudes components which may emit electromagnetic radiation.

Micro-Raman spectroscopy was carried out at Department of Chemie Oxydischer und Organischer Grenzflächen (Chemistry of Oxides and Organic interfaces), Institute of Functional Interfaces, KIT, Germany. A Bruker SENTERRA Raman spectrometer (Bruker Optics, Ettlingen, Germany) based on an Olympus BX-51 microscope (OLYMPUS Co. Tokyo Japan) provided insights into structures on the micrometre scale. A frequency doubled NdYAG Laser, λ=532 nm, operated at 5 mW power, served as the excitation source. The beam was focused through an objective, Olympus 100X, NA 0.8, in a 1 µm spot on the sample surface. An integration time of 80 s with 2 co-additions (2*40 s) was used to scan an area about 190*90 µm (Fig. 1.9). The obtained spectra were processed and baseline corrected using Bruker OPUS® software Ver. 7.2.

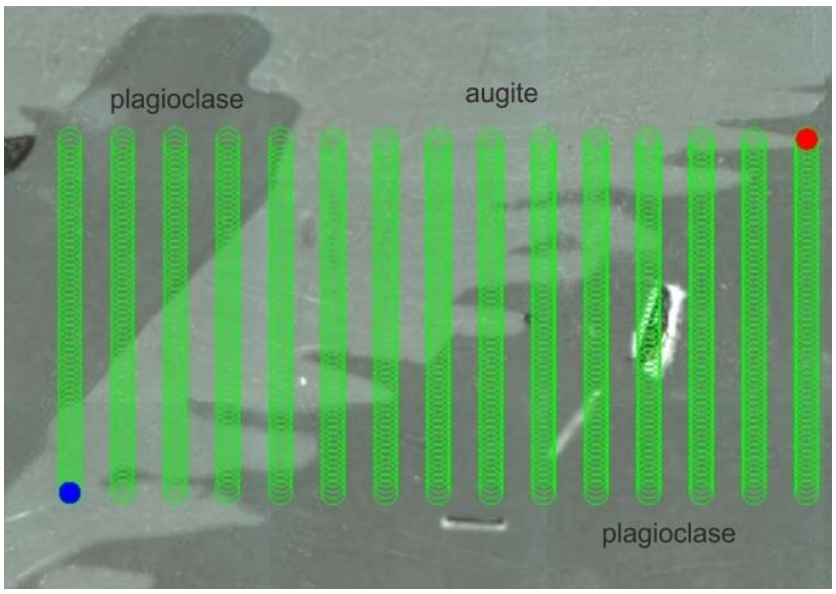

Figure 1.9. Fluorescence image showing array of analysis points for Raman spectroscopy at the augite-plagioclase grain boundary.

2. Estimation of shock pressure at the Lonar crater

2.1. Rock magnetism, magnetic fabrics and microfractures at Lonar crater, India

2.1.1 Magnetic Mineralogy and rock magnetic investigations

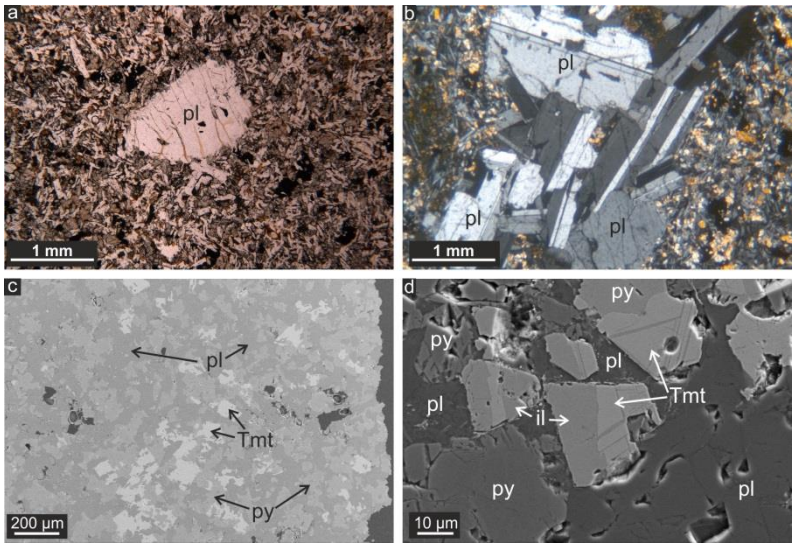

Figure 2.1 (a, b). Plane and cross polarized photomicrographs showing larger plagioclase (pl) grains embedded in a matrix of finer pyroxenes, plagioclase and opaque minerals (sample 1 and 8).
SEM images showing (c) coarse grained titano-magnetite (Tmt) with pyroxene (py) and plagioclase (pl) (sample 1) and (d) intergrowth of titanomagnetite and ilmenite (il) (sample 22).

The target basalt consists of large phenocrysts of plagioclase (up to 1500 µm) in a fine grained matrix of plagioclase (up to 60 µm,) pyroxene (up to 200 µm) and opaque phases (up to 100 µm; Fig. 2.1a, b, c). SEM and EDX show that most of the opaque phases are titanomagnetite and ilmenite (Fig. AF1), which occur as large laths intergrown with magnetite, i.e., sandwich type, or as small lamellae in magnetite, i.e., trellis type (Fig. 2.1c, d). While the sandwich type may either be a result of primary ilmenite nucleation or oxidation, the trellis type is clearly an oxidation product formed during cooling of subaerial basalts above 600°C [e.g., 131]. Some grains of pyroxene and plagioclase are altered to clay minerals. The alteration is stronger at the grain boundaries and can be attributed to low temperature hydrothermal activity during volcanic episodes or to weathering. No impact related hydrothermal alteration with minerals like saponite, minor celadonite and carbonates, as observed in basalt breccia present beneath the crater floor by Hagerty and Newsom [70], could be detected.

Magnetic susceptibility varies from $26.0*10^{-3}$ to $55.8*10^{-3}$ SI units in the investigated basalts indicating ferrimagnetic contribution (Table 2.1). Some samples, show a very subtle Verwey transition temperature (T_V) indicating a minor contribution of a magnetite end member near phase (Fig. 2.2a). Others show a distinct T_V around -180°C, which is about 30°C lower than that of pure magnetite (Fig. 2.2b). A T_V of -180°C is characteristic for titanomagnetite with about 5 per cent of the ulvöspinel component [132] or a vacancy concentration (δ) in pure magnetite

of 0.012 per formula unit ($Fe_{3(1-\delta)}O_4$) [133]. A sharp peak of T_V in some samples may be attributed to characteristically smaller grain size of titanomagnetite grains (Fig. 2.2a). These observations are in accordance with those of Senanayake and McElhinny [134], who suggest that a peak increase in magnetic susceptibility for pure or nearly pure magnetite at low temperatures indicates decreasing grain size down to 1 µm. However, as the size decreases below 1 µm, the peak flattens off until it vanishes, typical for SD magnetite grains.

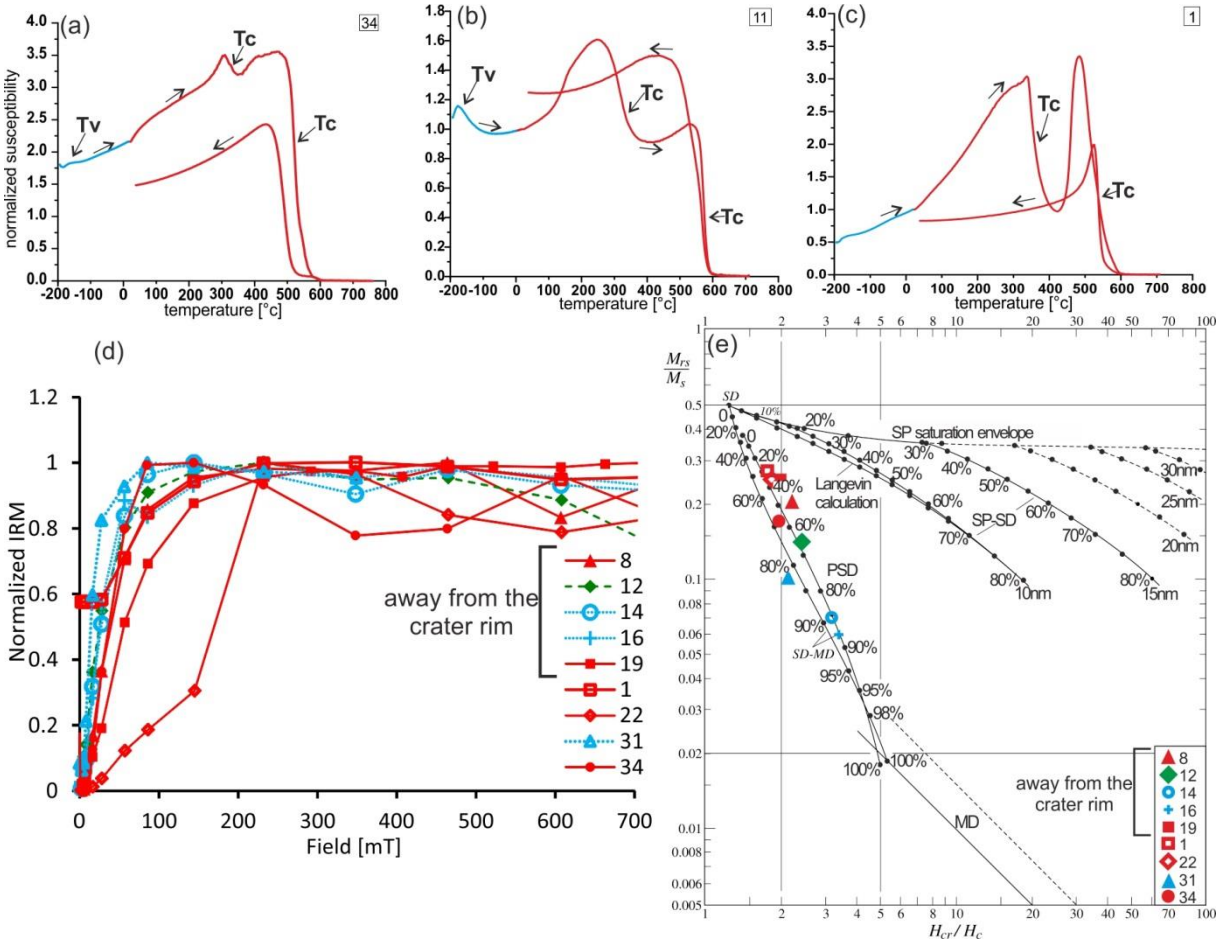

Figure 2.2. (a, b and c) Magnetic susceptibility (normalised by the susceptibility at 40°C) vs. temperature (see appendix, figure AF2 for all samples) (a) Shows a subtle T_V (around -180°C) and a characteristic T_C (570°C) (sample 34). (b) Shows a conspicuous T_V (-180°C) and two T_Cs (350 and 570°C) characteristic of titanomaghemite and titanomagnetite with low titanium concentration (sample 11). (c) Two T_Cs at about 350 and 561°C (sample 1). While in (a) the magnetite-near titanomagnetite dominates, in (c) it is the titanomaghemite, which transforms into a Ti-poor titanomagnetite. (d) Normalized IRM vs. applied field (mT). The curves with solid lines are of samples from the crater rim, while the curves with dashed lines are away from the rim. (e) Mrs / Ms vs. Hcr / Hc [Day plot modified after 135,136] indicate a variation of magnetic grain sizes, typical for basalts. The samples and curves with high MDF are represented by red-solid line, while those with intermediate and low MDF are represented in green-dashed and blue-dotted lines, respectively.

In some samples the T_V peak is nearly absent (e.g. sample 1, Fig. 2.2c). This may either be due to small magnetic domain, evident from hysteresis parameter (Fig. 2.2e), or titanomagnetite composition, evident from the dominant Curie temperature (T_C) at about 350°C.

Table 2.1. AMS data, representing mean of values from cores (N) collected from each site (sample no.), k_1d, k_2d and k_3d are the declination and k_1i, k_2i and k_3i are the inclination of k_1, k_2 and k_3, respectively. See Table AT1, for individual cores.

Sample No.	Site	N	k_m (10^{-3} SI)	k_1d	k_1i	k_2d	k_2i	k_3d	k_3i	k_1	k_2	k_3	P‘	T_{mean}
1	Rim	8	26.500	38	58	288	12	191	29	1.003	1.001	0.996	1.008	0.53
3	Rim	6	21.000	24	74	173	14	265	8	1.003	1.000	0.997	1.006	0.20
4	Rim	5	44.400	277	38	157	33	40	35	1.008	1.002	0.989	1.019	0.37
5	Rim	5	34.500	298	4	28	11	190	78	1.011	1.005	0.984	1.028	0.57
6	Rim	5	26.700	342	19	189	69	75	9	1.006	1.001	0.994	1.012	0.14
7	Rim	5	19.600	286	1	16	3	187	87	1.003	1.001	0.996	1.008	0.57
8	distant	5	35.500	145	19	252	40	36	44	1.004	1.002	0.994	1.011	0.67
10	int	5	75.300	97	69	289	20	197	4	1.005	1.000	0.995	1.010	0.02
11	distant	5	28.800	65	11	156	6	273	77	1.004	1.001	0.996	1.008	0.32
12	distant	6	48.800	26	33	120	6	220	57	1.008	1.002	0.990	1.019	0.31
13	distant	6	30.500	293	54	68	28	170	22	1.004	1.000	0.997	1.007	-0.07
14	int	6	61.700	269	1	359	24	177	66	1.003	1.001	0.997	1.006	0.42
15	int	5	49.300	179	18	323	69	85	12	1.006	1.005	0.989	1.020	0.83
16	distant	5	73.100	25	71	237	17	144	10	1.002	1.001	0.997	1.005	0.47
17	distant	6	59.700	136	17	253	57	36	28	1.012	1.010	0.978	1.039	0.86
18	distant	5	19.300	300	3	208	37	34	53	1.007	1.002	0.991	1.017	0.40
19	distant	5	19.200	17	20	266	46	123	38	1.007	1.001	0.992	1.015	0.25
20	int	5	21.800	202	22	320	50	98	32	1.006	1.001	0.993	1.014	0.21
21	Rim	5	39.000	8	5	102	32	270	58	1.005	1.003	0.991	1.015	0.72
22	int	5	27.200	5	53	161	34	259	12	1.007	0.999	0.994	1.014	-0.24
23	Rim	6	37.400	148	3	57	16	250	74	1.007	1.000	0.992	1.015	0.06
24	Rim	5	53.000	181	45	345	44	83	9	1.017	0.999	0.984	1.034	-0.06
25	Rim	8	50.700	210	28	120	1	28	62	1.006	1.003	0.991	1.016	0.54
26	Rim	6	31.100	3	48	114	18	219	36	1.003	1.001	0.996	1.008	0.55
27	Rim	5	32.100	175	17	271	20	47	64	1.007	1.003	0.990	1.019	0.52
28	Rim	5	51.200	267	79	150	5	59	10	1.010	1.005	0.984	1.028	0.61
29	Rim	5	46.200	346	31	219	45	96	29	1.006	1.003	0.990	1.017	0.60
30	Rim	9	30.300	214	28	318	25	83	50	1.004	1.002	0.994	1.011	0.72
31	Rim	5	53.100	274	45	144	33	35	27	1.011	1.005	0.984	1.028	0.56
32	Rim	5	30.400	68	8	158	2	259	82	1.006	1.003	0.991	1.017	0.59
33	Rim	5	32.500	169	22	259	1	352	68	1.005	1.004	0.991	1.015	0.80
34	Rim	6	46.800	221	16	127	13	360	69	1.006	1.005	0.989	1.019	0.93

Two T_C intervals are evident in the χ-T curves, one between 300° and 450°C and the other between 506°C and 570°C (Fig. 2.2a, b, c). The higher T_C (506°- 570°C) is due titanomagnetite poor in Ti. Additionally, the curves show an increase in susceptibility between 200° – 300°C. This susceptibility increase and the lower T_C (300° - 450°C) is attributed to titanomaghemite which is destroyed due to further heating in argon atmosphere. The irreversible curves (Fig. 2.2a, b, c), with lower susceptibilities in the cooling curves indicate that, the titanomaghemite is destroyed during heating. The titanomaghemite may have formed due to low temperature hydrothermal alteration or weathering of titanomagnetite.

In general the high temperature part of the χ-T curves from the Lonar basalt samples resemble irreversible type I/II curves shown in Oliva et al. [137], suggesting high-temperature oxyexsolution and low-temperature hydrothermal alteration of titanomagnetite, typical for basalt provinces worldwide.

Jackson et al. [138] and de Wall [123] suggest that the bulk magnetic susceptibility in titanomagnetite depends on the applied field. Therefore as a test, of presence of titanomagnetite, bulk susceptibility versus applied field was measured for three samples (sample 1, 12 and 16, Fig. 2.3d). Although all the three samples have different magnetic domain size (Fig. 8e), the curves show little dependence of bulk susceptibility on the applied field (Fig. 2.3d). Field dependence of AMS in 9 samples was also measured in applied fields of 300 and 50 A/m. Moreover, the results show no significant change in the orientations of k_1, k_2 and k_3 (Fig. 2.3a, b, c) In P'_{Hd} and χ_{Hd} maximum values in the order of 0.68% and 6.87% occur, respectively (Table AT2, AT3).

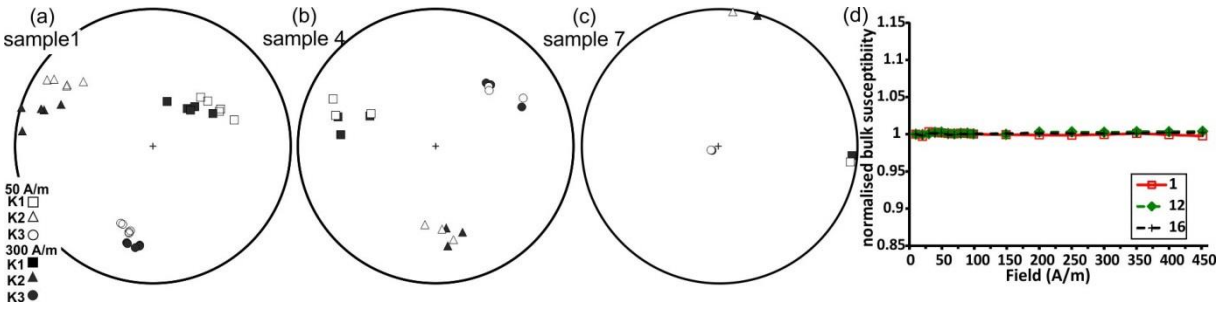

Figure 2.3. (a, b, c) Orientation of k_1, k_2 and k_3 axis of sample 1 (a), 4 (b) and 7 (c) obtained when measured at fields of 50 A/m (open) and 300 A/m (close), respectively. (d) Bulk susceptibility (normalised to susceptibility at 10 A/m) versus applied field.

IRM curves show that some of the samples are magnetically harder (sample 19, 22 and 8) than others. These magnetically harder samples have higher percentage of SD magnetite, as deduced from the Day plot (Fig. 2.2e). IRM curves do not show any difference in the coercivity of the basalt sampled from the crater rim and far away from it.

Hysteresis studies (Fig. 2.2e) reveal that a few samples such as 1, 22 and 19 contain much higher percentage (up to 70%) of SD magnetite than others and most samples show a dominance of pseudo-single domain (PSD) magnetite with a variable mixture of SD and MD magnetite. A comparison with SEM observations indicates that some of the samples with a higher percentage of SD magnetite have larger opaque Fe-oxide, grains (up to 200 µm). This observation is in agreement with the above mentioned high-temperature oxyexsolution, which decreases grain sizes due to trellis and\or sandwich type microstructures.

2.1.2 Natural remanent magnetization

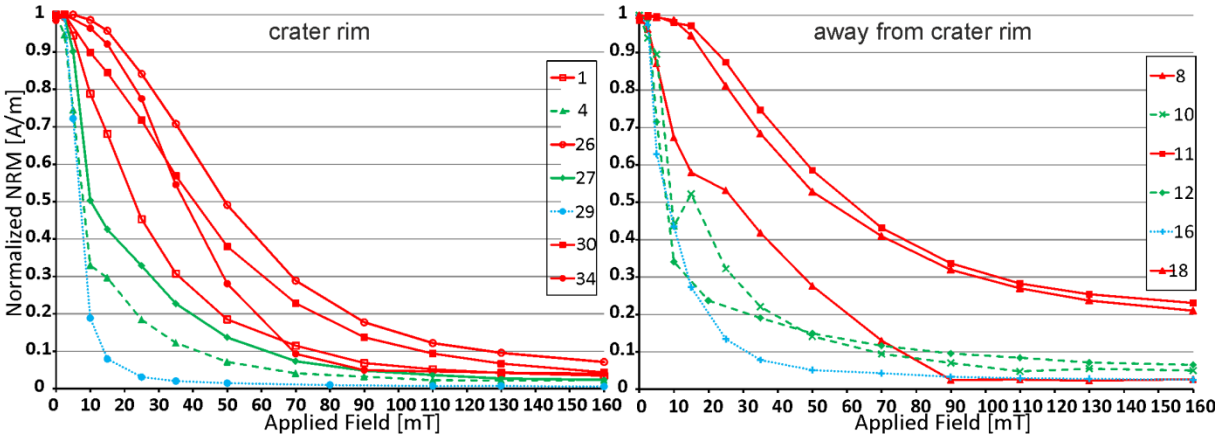

Figure 2.4. Normalised natural remanent magnetisation (NRM) versus applied field for representative basalt samples from the Lonar crater rim and away from it (see appendix table AT4 and figure AF3 for complete data set). The samples and curves with high MDF are represented by red-solid line, while those with intermediate and low MDF are represented in green-dashed and blue-dotted lines, respectively.

AF demagnetization of NRM from representative samples is shown in figure 2.4. Based on the MDF, the samples were classified into three groups. The first group (samples 31, 29, 14 and 16) shows magnetically soft behaviour with MDF up to 7 mT. These samples have higher multidomain (MD) component, especially sample 14 and 16 with about 80% of the MD fraction (represented in blue in Fig. 2.2e). The second group (samples 1, 6, 8, 11, 13, 18, 19, 20, 21, 26, 33 and 34) shows magnetically hard behaviour with MDF higher than 22 mT. These samples contain more than 60% of single domain (SD) grains (represented in red in Fig. 2.2e).

The third group (samples 4, 10, 12, 25, 27, and 28) is intermediate to the first two groups. They have MDF between 8 and 21 mT and consist of varying amounts of SD, MD and PSD grains (represented in green in Fig. 2.2e).

The magnetically hard basalts from the crater rim and away from the rim behavior show only a single NRM component with a mean direction of D= 173.9°, I = +51.2° (k = 30.75, α_{95} = 3.04°) and D= 190.0°, I = +57.4° (k = 44.54, α_{95} = 3.0°), respectively (Fig. 2.5a, b, Table 2.2). The NRM direction is almost constant throughout the demagnetization process, suggesting it to be a high coercivity (HC) component (Fig. 2.5c). These directions are comparable to the Deccan flow direction calculated by Vandamme et al. [104] (D = 157.6°, I = +47.4°, α_{95} = 1.9°) and Louzada et al. [12] (D = 156.0°, I = + 66.5°, k = 10.5, α_{95} = 8.6°, for flow 5; Table 2.2). A small scatter in the mean direction can be justified, as Vandamme et al. [104] argue that, scatter within a single flow may be due to early or late overprints (e.g., due to reheating of upper surface of a flow by succeeding flows).

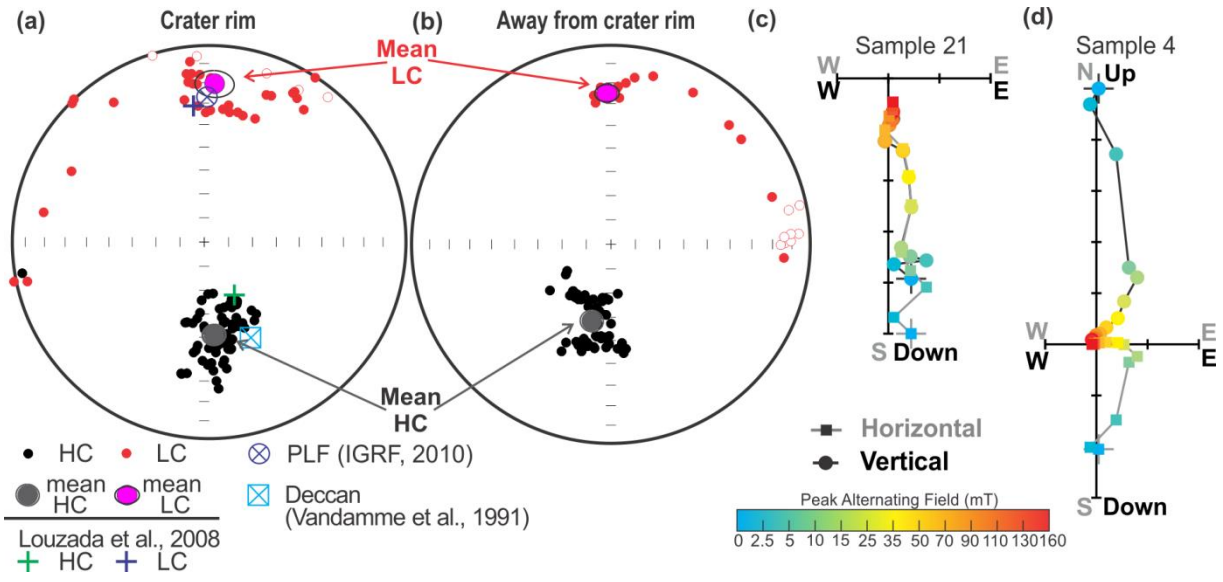

Figure 2.5. Lower hemisphere equal area projection of NRM vectors of samples from crater rim (a) and away from the rim (b). The HC and LC components are represented by black and red circles respectively. Close and open symbols denote the vectors pointing downwards and upwards, respectively. (c and d) Orthogonal demagnetization plots. Squares are 'N and E' projections and circles are 'up and E' projections. NRM in sample 21 has a single HC component, while in sample 4 it has only a LC component. Note the differences in scales of the plots.

Table 2.2. Comparison of paleomagnetic directions, at the crater rim and in unshocked, background flows, calculated in this study and in previous reports. D = declination, I = inclination, k = precision parameter, α95 = radius of 95% confidence. The number of samples in each group is indicated in parentheses. PLF = present day local geomagnetic field.

Site (no. of samples)	D°	I°	k	α95°	Reference
Primary Component (HC)					
Background flow 5 (51)	190.0	+57.4	44.54	3.0	**This study**
Crater Wall Flow 5 (77)	173.9	+51.2	30.75	3	**This study**
Crater Wall Flow 5 (65)	156.0	+66.5	12.1	59.7	Louzada et al., 2008
PaleoDeccan Direction at Lonar	157.6	+47.4	--	1.9	Vandamme et al., 1991
Aurangabad (19°51'N,75°16'E) – Deccan Basalt Flows	150	+48.0	26	5.5	Athavale and Anjaneyulu, 1972
Jalna (19°50'N, 75°56'E) – Deccan Basalt Flows	160	+46	32	3.8	Pal and Bhimasankaram, 1971
Secondary Component (LC)					
Background flow 5 (51)	358.5	25.0	342.42	2.8	**This study**
Crater Wall Flow 5 (14)	3.8	21.4	37.18	6.6	**This study**
Background flow (66)	7.4	+30.7	11.2	5.5	Louzada et al., 2008
Crater wall flow	9	+47	47.6	6.4	Poornachandra Rao and Bhalla, 1984
PLF*	-0.8	+28.0	--	8.8	IGRF (Finlay et al., 2010)

*Based on secular variation for the past 10 kyrs.

Some of the basalts, being magnetically too soft (containing larger proportions of MD titanomagnetite), show no stable NRM direction (Fig. AF4). Others, of intermediate magnetic hardness, show only a low-coercivity (LC) component which was removed by stepwise AF demagnetization by a field of about 15 mT (Fig. 2.5d). The mean LC component of basalts from the crater rim and away from the rim, D = 3.8°, I = +21.4° (k = 37.18, α_{95} = 3.0°) and D = 358.5°, I = +25.0° (k = 342.42, α_{95} = 2.8°), is comparable to the present day local geomagnetic field direction (D = -0.8°, I = +28°) calculated by IGRF [139] (Fig. 2.5a, b; Table 2.2). The LC component is approximately reverse to the HC component.

2.1.3 Anisotropy of magnetic susceptibility

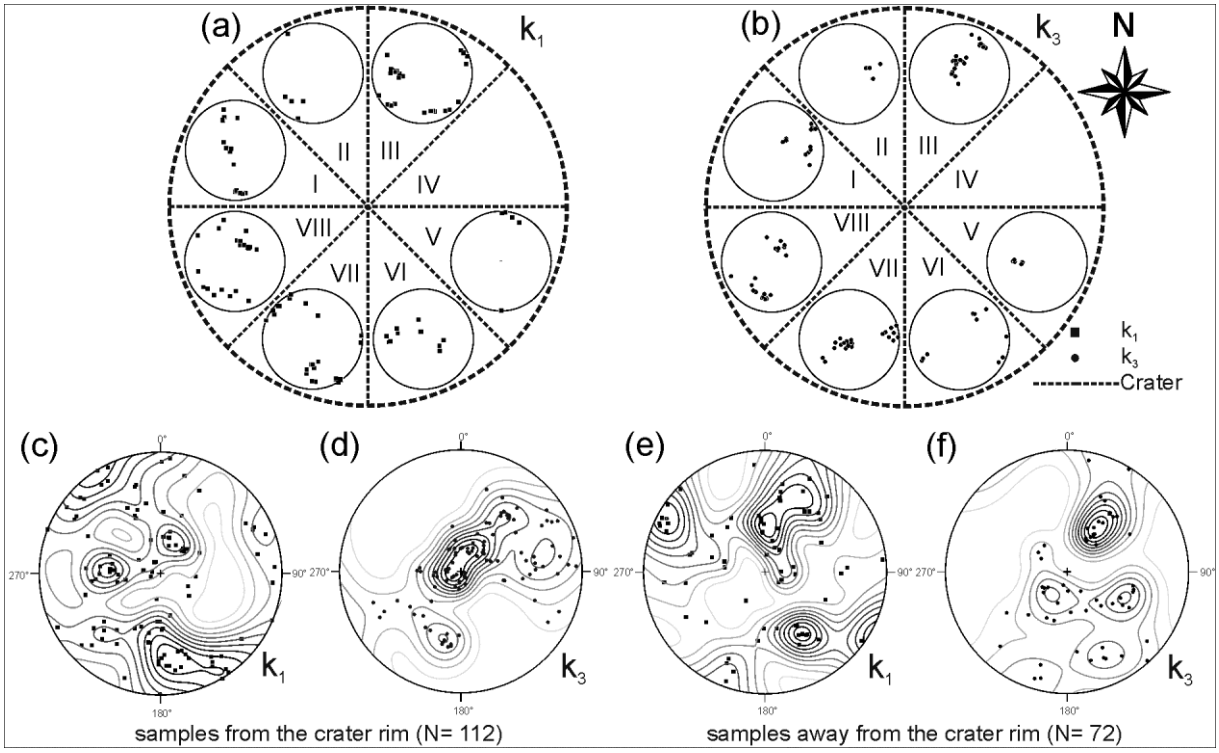

Figure 2.6. (a and b) lower hemisphere equal area stereographic projection of the k_1 and k_3 of the AMS ellipsoid of samples collected from the crater rim. The impact crater was subdivided into eight sectors (I to VIII) and the data of all samples from a sector are represented in one stereoplot. see appendix figure AF5 for stereoplots of individual cores (c to f) Density contours of the k_1 and k_3 of samples collected from the crater rim (c, d) and away from the crater rim (e, f). The density contours were calculated with cosine sums method, considering 20 as cosine exponent and 10 as contour intervals.

The Lonar crater is subdivided into eight orientational sectors (I to VIII in Fig. 2.6a, b). Figure 2.6a and 2.6b show the streoplots of the k_1 and k_3 axes of different samples in each sector. In the event of shock reorienting the k_1 and k_3 axes, the stereoplots are expected to show a strong preferred orientation in sectors I and VIII, weakly preferred orientation in sectors II, III,

VI and VII and probably random patterns in sectors IV and V. The results of our magnetic fabric analysis do not show any such pattern (Fig. 2.6a, b). The lack of preferred orientation in k_1 or k_3 axes in sectors I and VIII is, in particular, noteworthy in our observations.

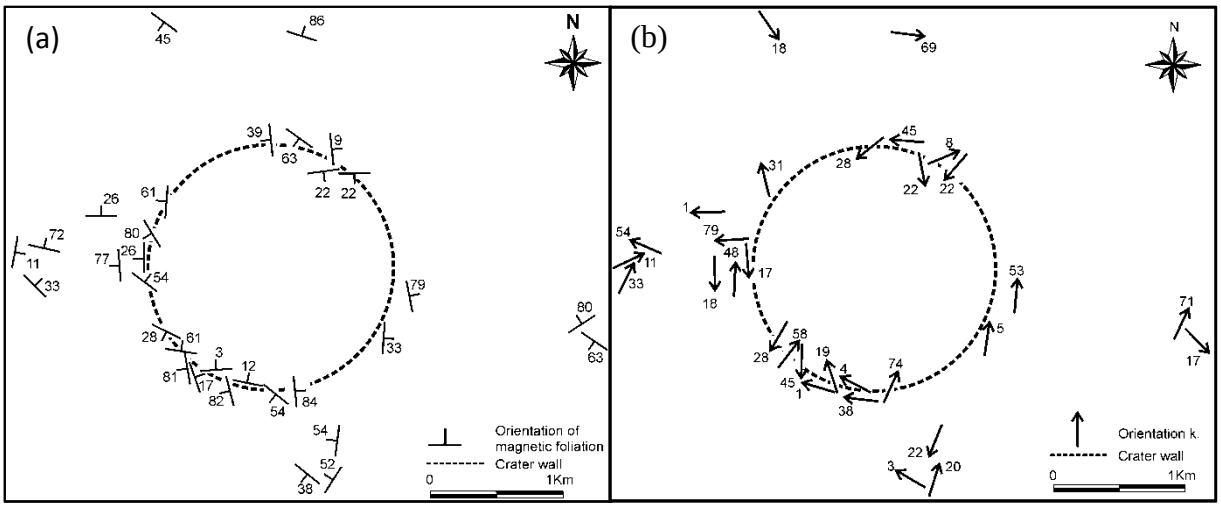

Figure 2.7. (a) Mean strike of magnetic foliations of the target basalt. The numbers indicate the dip angle of the foliations. (b) Orientation of the mean of maximum susceptibility axis (k1) at each sampling site in the target basalts. The numbers indicate the plunge.

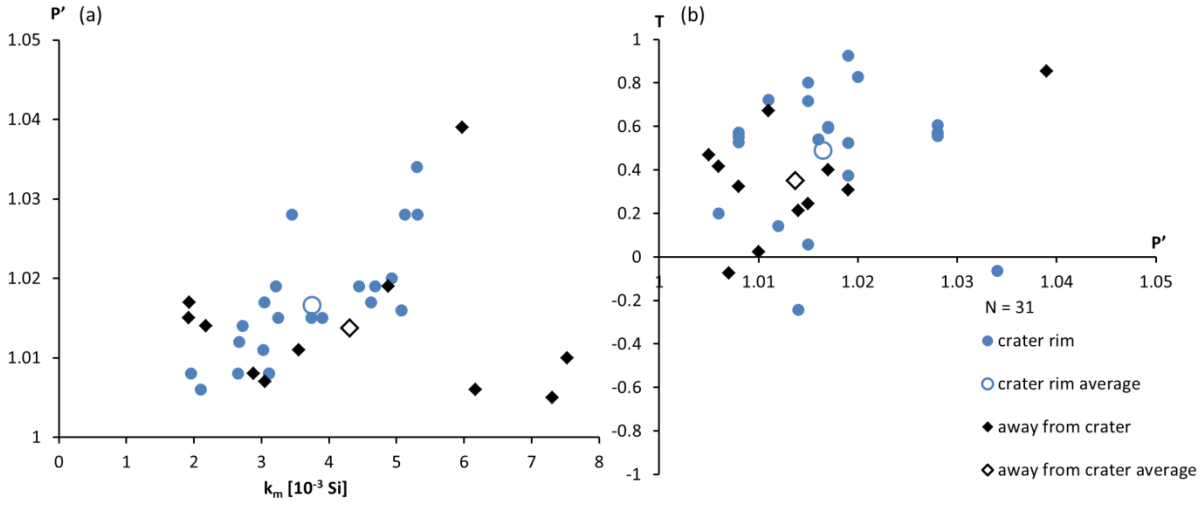

Figure 2.8. P' vs. k_m (a) and T vs. P' (b) discrimination diagrams of samples collected from the crater rim (circles) and away from it (diamonds). Note that each data point represents an average of at least 5 samples collected from the same location.

The magnetic foliation in crater rim basalts is generally sub-horizontal with randomly distributed k_1 and sub-vertical k_3 axes (Fig. 2.6a, b, 2.7a, b). Away from the crater rim, the basalts have random k_1 (Fig. 2.6e, 2.7b) and the magnetic foliation is characterised by varied strike and dip angles (Fig. 2.6f, 2.7a). The random pattern of k_1 in basalts from crater rim and away from the rim may be due to the very low anisotropy of the AMS ellipsoid.

Additionally, most samples show oblate fabrics, with $0.2 \leq T_{mean} \leq 0.7$ and $1.01 \leq P' \leq 1.03$ (Table 2.1, AT1). The average P' and T of the samples from the crater rim and those away from the crater are close to each other (Fig. 2.8a, b).

2.2. Shape preferred orientations studies and analysis of the magmatic foliations

SPO of plagioclase are determined by combining the shapes of plagioclase crystals in three orthogonal sections of the samples (Table 2.3, Fig. AF6, Table AT5; e.g., [140]). In the Lonar basalts, shape of the SPO ellipsoid is neutral to oblate (T in range of 0.006 and 0.485). The high degree of anisotropy of the ellipsoid, 3.072 to 4.41 reflects the elongation of plagioclase grains. The incompatibility index (√F), a measure of the misfit between sectional ellipses and the objective ellipsoid [141], has maximum value of 12.50%, which is within the expectable limit.

Table 2.3. Mean values obtained from the 'Ellipsoid' software. *N* is the average number of grains measured per perpendicular thin section. K_1, K_2 and K_3 are the longest, intermediate and shortest axis of the SPO ellipsoid. Note that the orientations K_1, K_2, K_3 are in sample coordinate system. *P'* and *T* are the anisotropy and shape factor of the SPO ellipsoid. *√F* is the incompatibility index (for definitions see [141]).

Sample no.	Sample position	N	K_1	K_2	K_3	P'	T	√F
19	Away from the crater	1284	104°/72°	0°/4°	268°/18	4.41	0.01	12.50%
1	SW crater rim	1756	269°/12°	87°/78°	179°/0°	3.072	0.40	10.20%
34	NE crater rim	1536	200°/85°	3°/5°	93°/2°	3.283	0.27	10.20%

The comparison between the orientations of the principal axes of AMS and SPO ellipsoids reveals that the magnetic fabric in some samples is perpendicular, and therefore inverse to the magmatic fabric (Fig. 2.9a). For example, in sample 19 the orientations of k_1, k_2 and k_3 of the AMS ellipsoid compare closely with the K_3, K_2 and K_1 of the SPO respectively (Fig. 2.9a). In other samples, the relationship is complex and described by the situations where k_2 and k_3 of the AMS ellipsoid match with K_1 and K_2 of the SPO respectively (Fig. 2.9b), or k_1 and k_2 of the AMS and, K_2 and K_3 of the SPO lie on a great circle (Fig. 2.9c). Furthermore, in the complex relationships either the K_3 of SPO approximates k_1 of AMS (Fig. 2.9b), or K_1 of SPO approximates k_3 of AMS (Fig. 10c). The complex relationships are ascribed to the insignificant differences in principal magnetic susceptibility axes k_2 and k_3 of sample 1 or k_1 and k_2 of sample 34 (Fig. 2.9b, c; Table 2.1).

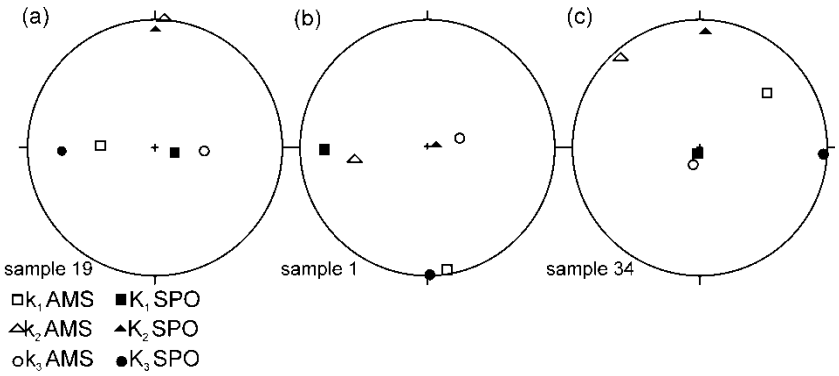

Figure 2.9. Lower hemisphere stereographic projections of AMS (hollow markers) and SPO (solid markers) axis from sample 1, 19 and 34. All data are presented in the sample coordinate system.

2.3 Microfractures

As mentioned earlier, the basalts contain large phenocrysts of plagioclase in a fine grained matrix of plagioclase, pyroxene and opaque phases. The fracture orientations were recorded only from larger plagioclase grains. To assure the post-magmatic origin, only transgranular microfractures, which extend over more than one phenocryst, or propagate from the phenocryst into the matrix, were considered. The matrix minerals are not fractured (Fig. 2.1d), probably because they are smaller than the plagioclase phenocrysts.

Two groups of microfractures, the radial and the concentric are common. Fractures in both the groups are characterised by uniform spacing and sub-vertical to steep dip angles (Fig. 2.10a, b). The overprinting relationships reveal that the radial microfractures are older than the concentric microfractures (Fig. 2.10b). Saponite, minor celadonite and carbonates along the fractures, in basalt breccia beneath the Lonar crater, are attributed to impact related hydrothermal activity [70]. However, no such minerals were found in the microfractures in basalts from crater rim and away from the rim. Neither was any conjugate shear microfractures observed.

A strong dominance of radial microfractures is notable up to a distance of twice the crater radius in the downrange direction, marked by light grey shade in figure 2.10c. The radial microfractures converge towards the crater centre. At the thin microscopic scale, the radial microfractures commonly occur in parallel sets, figure 2.10a. Similar radial microfractures are observed in the cross range, marked by dark grey shade in figure 2.10c, show radial microfractures similar to those in the samples collected in the downrange direction. However in the cross range, concentric microfractures are relatively more abundant than in the downrange. The concentric microfractures are characterized with traces parallel to the crater

rim, while at the microscopic scale, the traces are tangential to the crater rim. The microfractures in the up range have unstable orientation with respect to the impact crater (Fig. 2.10c).

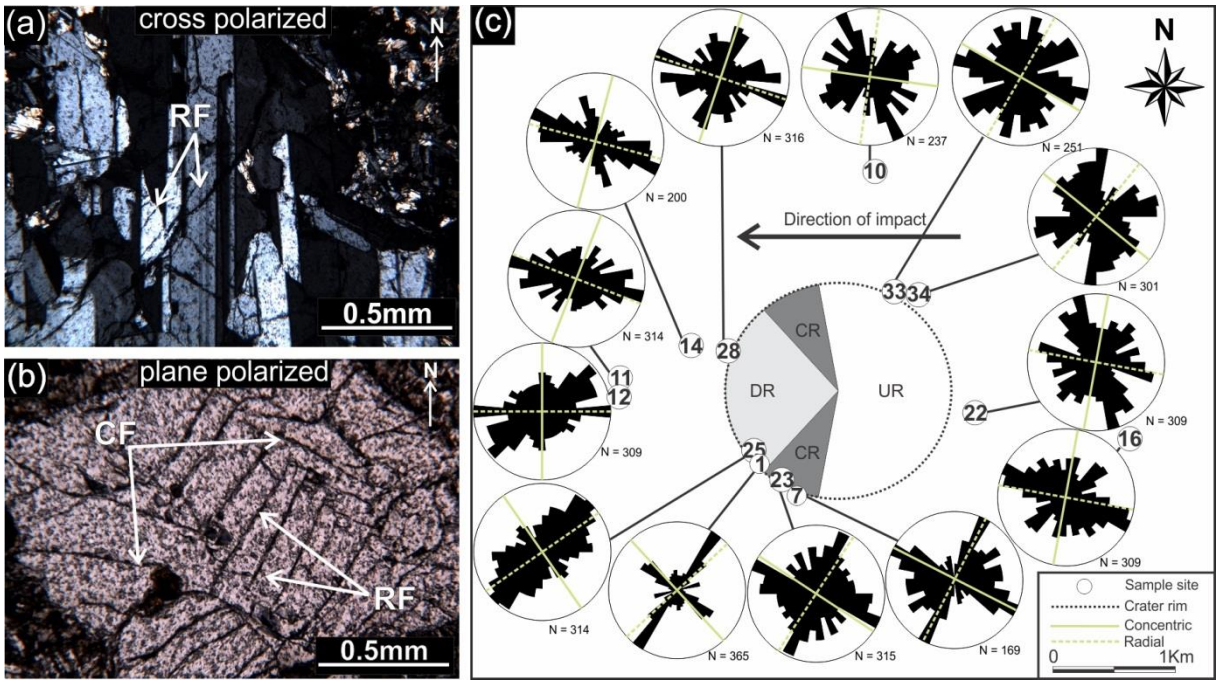

Figure 2.10. (a) Transmitted light photomicrograph (sample 1) showing the dominance of radial microfractures (RF) in plagioclase. (b) Transmitted light micrograph (sample 23) showing perpendicular and cross-cutting sets of radial (RF) and concentric (CF) microfractures. (c) Rose diagrams show orientation of microfractures recorded from thin sections. The green solid and dashed lines within the roses represent the radial and concentric (tangential) directions considering their sampling site with respect to the impact crater. The light grey section of the crater (dashed circle in the middle) marks the downrange direction, 'DR', with an abundance of radial microfractures, while the dark grey marks the cross range, 'CR', with an abundance of both radial and concentric microfractures. 'UR' marks the up range directions with respect to the east to west direction of impact.

2.4 Discussion

Recently published accounts for Lonar crater suggest that the magnetic fabrics, k_3 axes, are reoriented due to shock [57,90]. The results of our rock magnetic studies show that the magnetic fabrics in the Lonar crater basalt have a primary magmatic origin. Any hypothesis of the reorientation of the magnetic fabric axes is also inconsistent with the results from numerical and experimental simulations on the Lonar crater [6,7,12].

Review of published literature reveals, brittle deformation, fracturing, response to shock pressure depends upon the various rock properties such as grain size, porosity, pre-existing

fractures, density [8,42,91,142,143]. Moreover, in pressure range of 0.2 to 20 GPa, a direct correlation between shock pressure and fracture density is observed, in rocks with similar mineralogical and physical properties [8,9]. Therefore, microfractures may be used for a qualitative estimation of shock pressure.

2.4.1 Magnetic mineralogy and the origin of magnetic properties in Deccan Basalts

The dependence of AMS on the applied field is well established in situations where the target rocks contain titanomagnetite [122,123,138,144]. The lack of correlation between the applied field and AMS in the Lonar basalt is primarily due to the low temperature hydrothermal alteration of titanomagnetite into titanomaghemite [137]. Variations in the magnetic domain size, as observed in the Lockne basalts, leads to differences in their magnetic hardness (Fig. 2.2e). Depending upon the dominance of SD, PSD or MD grains, the basalts are, therefore, classified as magnetically hard, intermediate or soft.

As argued by Gattacceca et al. [10] and Mang et al. [11] an increase in coercivity implies brecciation of the magnetic minerals at shock pressures ≥3 GPa. In Lonar, the IRM and the AF demagnetization curves for the samples collected close to and far away from the crater are similar (Fig. 2.2d, 2.4). This similarity of coercivity implies that the shock waves were not strong enough to cause any significant microfracturing in the ferrimagnetic minerals of the target basalt and the level of shock pressure was < 3 GPa.

Origin of natural remanent magnetization in Deccan basalts at the Lonar crater

Our identification of two separate NRM components in the Lonar basalts is in agreement with earlier studies [12]. The LC component, observed in magnetically softer samples, demonstrates present day magnetic field orientation and may be attributed to either post-impact viscous remanent magnetization and/or chemical remanent magnetization [cf. 12].

On the other hand, the rocks with higher percentage of SD titanomagnetite show only a HC component. Arif et al. [90] conclude that the mean HC_HT component of shocked basalts from the Lonar crater rim, D = 120.5°, I = + 34.2°, are reoriented due to impact generated magnetic fields and therefore, are different from paleo-Deccan directions. However for this interpretation, the authors did not consider the data from more than half of their sampling sites, from SE, S and SW of the impact crater; and did not present data from NE part of the

crater. The interpretations [90] are based on the NRM direction calculated only from the N and NW segment of the crater. They attribute the reorientation to unidirectional impact generated magnetic field and infer that the basalts acquired an HC_HT magnetization component, systematically oriented in the uprange direction of the impact.

The HC component obtained in our study is similar to that in the unshocked Deccan basalt, calculated by Vandamme et al. [104] and Louzada et al. [12]. We argue that: (i) in laboratory experiments, impact generated magnetic fields generally exhibit significant bilateral anti-symmetry in both magnetic intensity and polarity [e.g., Fig. 3 in 145]. It is therefore expected that the shock induced remanent magnetization, if present, is non-unidirectional and not systematically oriented in uprange direction and (ii) the impact generated paleofields at Lonar were weak, not greater than several tens of μT [146]. Therefore, in agreement with Louzada et al. [12], it is suggested that the HC component, was acquired during cooling of the lava and the impact generated magnetic-field was not strong enough to overprint it.

Origin of magnetic fabrics in basalts near the Lonar crater

Low peak shock pressures may lead to rotation of only one of the susceptibility axes and render a random magnetic fabric [6,7,10]. As the impact direction at Lonar was east to west, the most intense shock waves are expected in the downrange, i.e., sectors I and VII of the crater (Fig. 2.6b). If strong enough the shock wave should, therefore, reorient either k_1 or k_3 westwards, at least in the western part of the crater (sectors I and VII). In contrast, the k_1 axis is more or less random in the western sectors (I, II, VII and VIII; Fig. 6a) and the k_3 axis plunges eastward in sectors I and II, and is randomly directed in sector VIII (Fig. 2.6b). The AMS study therefore implies that, the shock waves were not strong enough to reorient k_1 or k_3 axis in the Lonar crater.

In undeformed lava flows, the titanomagnetite crystallizes within silicate framework and reflects the direction of lava flow [147,148]. The correlation of shape, distribution and anisotropy of magnetic susceptibility, with silicate fabric may reveal the undeformed nature of the igneous rocks [149] and the magma flow directions [e.g., 115,150]. To investigate whether the magnetic fabrics in crater rim basalts are magmatic or affected by some secondary process, such as shock metamorphism or hydrothermal alteration, the SPO of plagioclase was compared with the AMS in three samples. In all the three samples, the AMS fabric is inverse

with respect to the SPO. According to published literature [151–153] this inverse relationship is attributed to dominance of SD magnetic grains (Fig. 2.2e). The inverse relationship between the two fabrics supports the inference that the magnetic fabrics have magmatic origin and have not undergone any rotation due to the impact.

The randomly striking and shallow dipping magnetic fabrics in the Lonar crater basalt are similar to those that have been reported in the pristine Deccan basalt from Malwa plateau by Schöbel and de Wall [147]. Such types of magnetic fabrics are also common in the pristine lava flows of other regions, e. g., Hawaii [154]. We infer, therefore, that the magnetic fabrics in Lonar basalt are related to primary lava flow rather than impact. The variations in the magnetic fabrics can be attributed to physical processes, such as magmatic deformation and/or the spatial location of the sample within a flow [115]. The overall low degree of magnetic anisotropy implies that the lava body did not experience flow related shearing after crystallization of titanomagnetite [154,155].

The same basalt flow, top most in the crater rim, was sampled by Misra et al. [57] and Arif et al. [90], as well as in the present study. However, the earlier studies [57,90]) lack any control on the sampling sites with respect to the overturned part of the topmost flow, whereas we sampled only the normal part of the topmost basalt flow. Moreover, in spite acknowledging that the topmost layer of the basalt flow, the overturned limb, shows radially outward dips, they fail to tilt-correct their AMS orientations. The impact induced outward tilting of the basalts may have been a contributing factor in the 'relative westward shift' of the k_3 axis observed by Arif et al. [90], especially in the western part of the crater. It is noteworthy that firstly, in the rocks from the NW and W sectors, and from the 'wall to the west of the crater rim (CRW)' that should have suffered maximum shock intensity, the k_3s vary in plunge from vertical (NW sector) to shallow northeastward (CRW), and moderate eastward to shallow northwestward plunge (W sector; Fig. 3 in Arif et al. [90]). Secondly, all around the crater rim, except in the SW sector (13.6% of all samples), the k_3 do not show any preferred orientation; while in the unshocked basalts from the Durga Tegri sampling site, the k_3 have a well clustered, moderate eastward plunge (Fig. 3 in Arif et al. [90]). The authors [90] do not present statistical parameters, such as k and α_{95}°, that may demonstrate the consistency of the arguable westward shift in k_3's orientation. The orientations of k_3 in the crater rim seem more or less random (Fig. 3 in Arif et al. [90]). Such random orientations would be in

accordance with the present results (Fig. 2.6, 2.7) and would agree to those from other craters [e.g., 156]. Moreover, values of P' in the unshocked basalts, 1.006 - 1.042 and in the shocked basalts, 1.004 (SE sector) - 1.042 (E sector), overlap and differ insignificantly by mere 1.93% [57,90]. In conclusion, the P' and k_3 orientations demonstrated by Misra et al. [57] in their figure 2 and 3 are close to present results (Fig. 2.6, 2.7, 2.8). However, we do not agree with their proposed shock induced re-orientation of k_3 and reduction in P'. Additionally, the comparison of the magnetic fabrics with the magmatic fabrics, figure 2.9, reveals that the magnetic fabrics are of magmatic origin and have not been reoriented.

Previous workers [5,57,62] report that the top most basalt flow in the crater rim have quaquaversal dips, probably due to shock induced outward tilting. However, our results show that, the k_3 from the crater rim are steeper and more tightly clustered than the k_3 away from the rim. We therefore propose that, because the Lonar impact event was small, the rocks in the crater rim were not significantly tilted outwards and only the topmost basalt flow was overturned, giving quaquaversal dips.

2.4.2 Microfractures

Transgranular microfractures having radial, concentric and random trends, with respect to the impact crater, are common throughout the Lonar basalt. Shock experiments demonstrate that the radial- and concentric fractures form during the compressive and the tensile phase of the shock wave respectively, and the strength of the shock is asymmetric, strongest being in the downrange direction [42,157,158]. The dominance of radial microfractures in the downrange direction may be due to a strong compressive phase of the outgoing shock wave. However, equal dominance of both concentric and radial microfractures in cross range direction is attributed decrease in intensity of the shock wave. The basalt in the uprange direction, i.e., east of the impact crater, experienced the lowest shock pressures and therefore an overall random trend of microfractures is observed.

Origin of microfractures

Kumar [62] grouped the fractures visible in the crater rim into pre-impact flow-parallel fractures and impact induced radial, concentric and conical fractures. The radial fractures have steep dips and strike perpendicular to the crater rim; the concentric fractures strike

parallel to the crater rim and dip towards the crater floor; and the conical fractures are similar to the concentric fractures in strike but dip away from the crater center [62]. It is important here that, the orientation of the fractures were not tilt-corrected for the radially outward dipping (angles averaging at ~ 20°) topmost basalt flow. It is therefore, possible that a tilt correction, which compensates for the radial outward dips of the basalt flow, will not affect the trends of the radial fractures but may render the concentric fractures as vertical. The trends of these two three fracture sets would then correspond with the microfracture trends from this study. Contrary to these interpretations, Maloof et al. [5] remark that the high angle fractures are not consistently radial to the crater center, but are similar to the spaced 60-120 and 90-90 joint sets. They further suggest that, the flow banding may be confused for fractures and that steeper quaquaversal dips in the upper crater wall are associated with rim-folded flow banding, and not with conical network of cracks [5]. However, Maloof et al. [5] admit that they do not have enough data to question Kumar's [62] results. Without statistical data, the interpretation of Maloof et al. [5] seems equivocal.

On the other hand, the most compelling argument in favour of an impact related origin of the microfractures is their symmetrical distribution around the crater, which may be explained by the expected shock wave intensities. Similar distribution of impact generated fractures is also reported from other natural impact craters, e.g. Meteor crater, USA [91].

The microfractures observed in the Lonar crater are similar to the micrometre scale radial and concentric fractures around impact craters formed by micrometeoroid impact on solar panels of a spacecraft [102]. In some micro-craters, the radial microfractures post-date the concentric microfractures, while in others the radial microfractures pre-date the concentric microfractures. The overprinting relationship between the radial and concentric fractures is a useful indicator of their genetic relationship [e.g., 102]. In the Lonar crater, the radial microfractures are older than the concentric microfractures. Both the radial and the concentric microfractures are suggested to have formed during different phases of a common shock wave. The radial microfractures formed during the initial compressive phase [42,92], parallel with the σ_1 (direction of maximum compression) of the shock wave while the younger concentric fractures were formed during the tensile phase of shock wave, due to sudden release of shock pressure [42,159–161].

Comparison with impact induced fractures in experimental

The most damaged rocks in a target lie in the crater wall and beneath the crater floor; while farther away from the crater the damage decreases substantially due to decay of the shock wave [30,42,49,162]. In Lonar, the radial- and concentric microfractures in the crater rim and radial microfractures away from the crater rim in the downrange direction are, respectively, similar to the two distinct microfractures in experimentally produced craters: (i) radial and concentric fractures around the crater rim, and, (ii) the "near surface fractures" up to a distance of several crater radii from the crater (Fig. 1.4) [92]. However, unlike the homogenous distribution of fractures around experimental crater, those in Lonar are distributed inhomogeneously, but symmetrically. Difference in the distribution may be attributed to a spherical shock wave front, generated by a vertical impact in the experiments, as compared to an inhomogeneous shock wave front, stronger in the downrange direction, generated by an inclined impact at Lonar crater.

3. Estimation of shock pressure at the Lockne crater

3.1 Petrography and microfabrics of the crystalline basement rocks

The target lithologies are grouped into metavolcanic, granite and dolerite rocks. The metavolcanics, consisting of fine grained quartz, plagioclase, are classified into ferrimagnetic and paramagnetic types (s. section 3.2). The former have substantially higher mafic mineral content and larger grain size than the latter (Fig. 3.1a, b, c). SEM and EDX studies of the ferrimagnetic metavolcanic rocks indicate intergrowths of chlorite and biotite with syngenetic magnetite and/or ilmenite (Fig. 3.1b). The metavolcanics have a pronounced metamorphic foliation and show deformational structures such as rotated porphyroblasts and pressure shadows that have a dextral shear sense (Fig 3.1a).

The granite is medium to coarse grained, composed of anhedral quartz, subhedral feldspar, along with lesser amounts of subhedral chlorite, biotite and epidote (Fig. 3.1d). They contain less than 5% of opaque phases mostly rutile, pyrite and leucoxene, and frequently show effects of semi-brittle/ductile deformation and shear zone fabrics such as S-C fabric and book-shelf structures [163,164,e.g., 165].

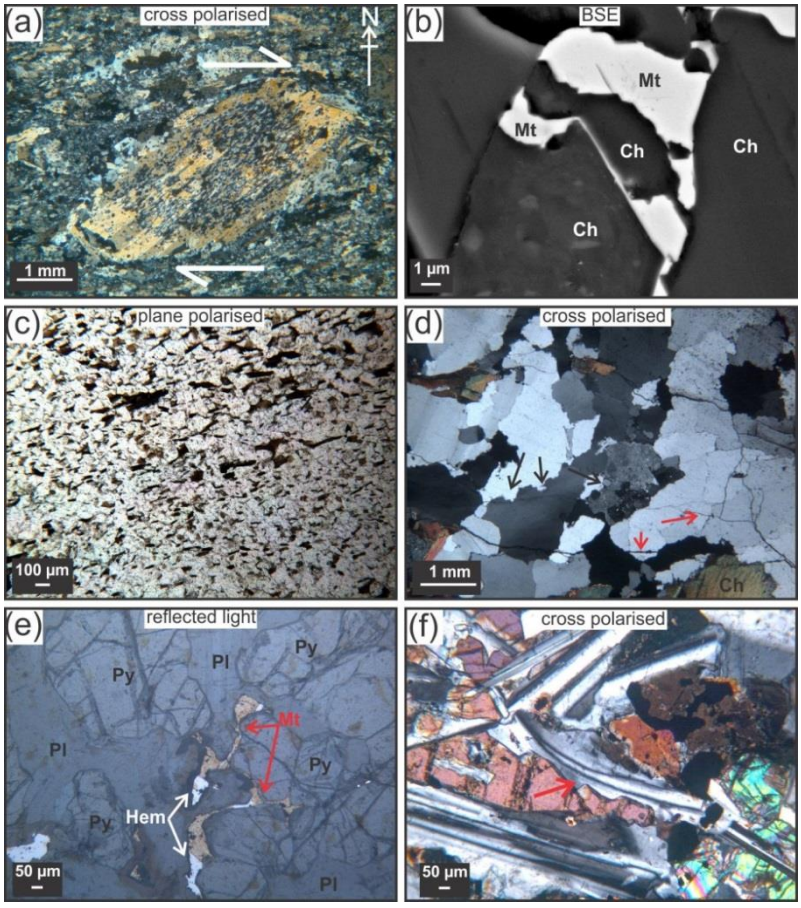

Figure 3.1 (a) Horizontal section (oriented in original position) of ferrimagnetic metavolcanic with plagioclase porhyroblast demonstrating dextral shear sense (sample 3). (b) Ferrimagnetic metavolcanic rock with intergrown titanomagnetite (Mt) and chlorite (Ch) (sample 3). (c) Paramagnetic metavolcanic rock with fine grained quartz and preferentially oriented biotite depicting metamorphic foliation (sample 30). (d) Granite showing grain boundary migration (black arrows) at quartz grain boundary and transgranular microfractures (red arrows). (e) Dolerite covered with ferrofluid showing intergrown pyroxene (Py), titanomagnetite (Mt) and hematite (Hem) surrounded by plagioclase (Pl). (f) Curved plagioclase crystal, red arrow, in dolerite.

The dolerite is medium to coarse grained. It has sub-ophitic texture of pyroxene, olivine and plagioclase. Magnetite, ilmenite, chalcopyrite, pyrrhotite and hematite are the most common opaque phases (Fig. AF7). Magnetite is commonly intergrown with ilmenite and sometimes altered to hematite (Fig. 3.1e). Although in dolerite, some plagioclase show curved crystals (Fig. 3.1f), probably plastically deformed during magmatic emplacement, in general zone fabrics or other post magmatic ductile deformational fabrics are not seen.

3.2 Magnetic mineralogy and AMS fabrics

The ferrimagnetic metavolcanic rocks have higher mean bulk magnetic susceptibility (k_m) (31.6 $*10^{-3}$ to 2.62 $*10^{-3}$ SI units) as compared to the paramagnetic metavolcanic rocks (k_m = 0.85 $*10^{-3}$ to 0.04 $*10^{-3}$ SI units, Table 3.1).

The χ-T curves of the ferrimagnetic metavolcanic, e.g., figure 3.2a, show a T_C and T_V at about 570° and -170°C respectively (Fig. AF8). This T_V is about 20°C lower than that of pure magnetite, and is, therefore, suggests of about 5 percent of the ulvöspinel component [132] or a vacancy concentration (δ) in pure magnetite of 0.012 per formula ($Fe_{3(1-\delta)}O_4$) unit [133]. In the heating cure, a subtle hump is observed between 250° and 350°C (Fig. 3.2a, Fig. AF8) which may indicate presence of minor amounts of maghemite. The maghemite is commonly destroyed during heating beyond 350° C, which leads to lower χ in the cooling curve (Fig. 3.2a)

The χ-T curve of the paramagnetic metavolcanic sample, e.g., figure 3.2b, has a parabolic shape suggesting the presence of only paramagnetic phases (Fig. AF8). Moreover, absence of ferrimagnetic minerals and, therefore, weak signal leads to considerable noise in the curve. Significantly higher χ, in the cooling curve, may be attributed to the formation of some new ferrimagnetic iron oxide phases during heating (Fig. 3.2b, Fig. AF8).

In granites, k_m varies from 0.1 $*10^{-3}$ to 0.2 $*10^{-3}$ SI, typical for paramagnetic behaviour (Table 3.1). Moreover, due to low k_m, the χ-T curve show considerable noise, similar to the paramagnetic metavolcanics, and do not show either a conspicuous T_C or T_V. However a slight decrease in susceptibility is observed between 400° and 500°C, figure 3.2c, which may be attributed to minor amounts of titanomagnetite and/or titanomaghemite, probably present as inclusions in silicate minerals.

Table 3.1. AMS data, representing mean of values from cores (n) collected from each site (sample no.), k_1d, k_2d and k_3d are the declination; k_1i, k_2i and k_3i are the inclination and k_1, k_2 and k_3 are the intensities of k_1, k_2 and k_3. See Table AT6 for AMS parameters of individual cores.

Site no.	N	Lithology	k_m (10^{-3})	k_{max}d°	k_{max}i°	k_{int}d°	k_{int}i°	k_{min} d°	k_{min} i°	k_{max}	k_{int}	k_{min}	P‘	T_{mean}
1	8	Granite	0.224	244	11	337	13	114	73	1.011	1.007	0.982	1.033	0.76
2	8	Dolerite	7.590	58	25	315	27	185	52	1.026	1.006	0.968	1.062	0.34
3	5	Ferrimagnetic Metavolcanic	6.420	296	21	116	69	26	0	1.037	1.017	0.946	1.102	0.58
4	7	Ferrimagnetic Metavolcanic	2.620	293	27	68	54	191	21	1.049	1.017	0.934	1.129	0.47
5	7	Granite	0.173	42	26	147	28	276	50	1.014	0.998	0.988	1.026	-0.27
6	6	Paramagnetic Metavolcanic	0.850	102	46	313	39	210	16	1.028	0.998	0.974	1.056	-0.11
7	5	Ferrimagnetic Metavolcanic	31.600	72	66	336	2	245	24	1.150	0.979	0.872	1.321	-0.17
8	5	Dolerite	6.910	291	1	21	19	197	71	1.029	1.000	0.971	1.060	0.02
9	6	Dolerite	7.130	258	1	349	34	167	57	1.021	1.006	0.973	1.050	0.39
10	7	Dolerite	11.200	313	3	222	20	50	70	1.015	1.000	0.985	1.030	0.03
11	6	Dolerite	2.950	219	17	128	3	28	73	1.006	1.003	0.991	1.016	0.61
12	6	Dolerite	9.980	343	20	249	10	136	67	1.021	1.000	0.980	1.042	-0.01
13	6	Dolerite	15.900	296	18	205	3	107	72	1.014	1.006	0.980	1.037	0.55
14	6	Granite	0.251	22	74	121	2	211	16	1.030	0.999	0.971	1.060	-0.04
15	8	Granite	0.151	25	27	168	58	286	17	1.047	0.994	0.959	1.092	-0.20
16	6	Ferrimagnetic Metavolcanic	10.800	324	5	158	85	54	1	1.064	1.036	0.901	1.196	0.68
17	6	Dolerite	24.000	280	30	177	20	59	52	1.013	1.002	0.985	1.028	0.20
18	7	Dolerite	12.600	166	4	258	27	69	63	1.012	1.005	0.983	1.030	0.56
19	5	Dolerite	1.090	195	21	95	24	321	58	1.006	1.002	0.992	1.015	0.45
20	6	Dolerite	15.300	277	39	174	16	67	47	1.021	1.002	0.977	1.045	0.18
21	8	Dolerite	30.300	274	10	4	1	98	81	1.025	1.003	0.972	1.055	0.19
22	5	Dolerite	18.800	344	26	246	15	129	60	1.006	1.001	0.993	1.013	0.25
23	8	Dolerite	44.800	324	1	54	8	226	82	1.024	0.997	0.978	1.048	-0.17
24	6	Dolerite	17.400	126	12	219	16	1	70	1.012	0.999	0.988	1.025	-0.07
25	7	Granite	0.101	294	10	33	42	194	46	1.007	0.998	0.995	1.012	-0.56
26	6	Paramagnetic Metavolcanic	0.044	189	75	333	13	65	9	1.042	1.039	0.919	1.155	0.95
27	6	Paramagnetic Metavolcanic	0.654	321	64	174	22	79	13	1.040	0.996	0.964	1.079	-0.15
28	14	Granite	0.141	245	2	336	22	149	68	1.013	1.003	0.983	1.031	0.33
29	6	Granite	0.189	292	15	25	13	155	70	1.001	1.000	0.999	1.002	0.39
30	8	Paramagnetic Metavolcanic	0.185	175	41	82	3	285	16	1.070	1.006	0.924	1.159	0.16
31	7	Dolerite	21.600	315	6	225	0	132	84	0.031	0.007	0.995	1.010	0.31
32	9	Dolerite	11.000	329	26	76	31	207	47	0.032	0.009	0.979	1.042	0.16
33	7	Dolerite	15.400	269	26	176	6	75	64	0.033	0.994	0.979	1.049	-0.35

Bulk magnetic susceptibility in the dolerite ranges from $1.09*10^{-3}$ to $24*10^{-3}$ SI indicating presence of varying amount of the ferrimagnetic mineral (Table 3.1). The χ-T curves show a T_V at temperatures between -160° and -150°C and a T_C at about 580°C, characteristic of multi-domain magnetite. While the high temperature curves are always reversible beyond T_C, reversibility is lost below T_C, probably due to development of some secondary, metastable ferrimagnetic phase during heating of the samples (Fig. 3.2d).

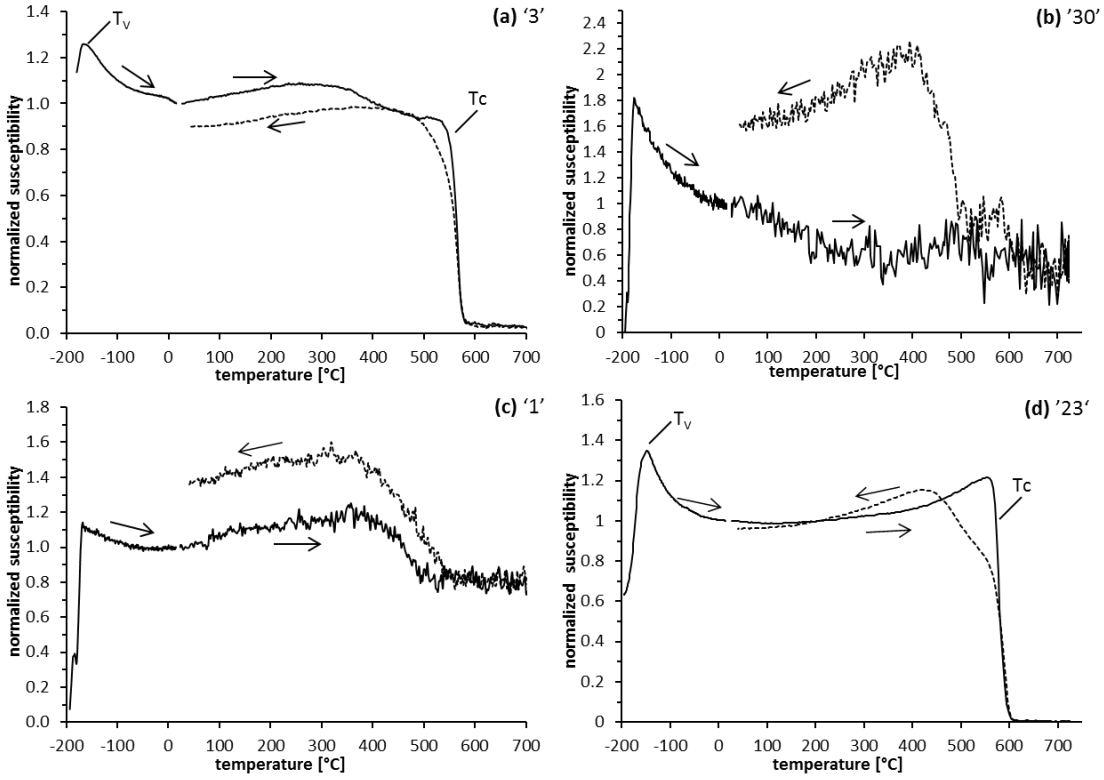

Figure 3.2. Susceptibility (normalised to susceptibility at 40° C) vs. temperature curves. (a) Ferrimagnetic metavolcanic, sample-3, shows distinct T_V (-170°C) and T_C (570°C). (b) Paramagnetic metavolcanic (sample 30) with parabolic shape and some secondary ferrimagnetic phase in the cooling curve. (c) Granite (sample 1) shows a subtle T_C between 400 - 500°C (d) Dolerite (sample 23) shows T_V (-160°C) and T_C (580°C). See appendix Figure AF8 for additional χ-T curves.

The oblate to prolate metavolcanic rocks have highest P' among all basement lithologies, averaging 1.152, which does not correlate with k_m as the average correlation coefficient is -0.136 (Fig. 3.3a, b). The magnetic foliations of the ferri- and para magnetic metavolcanic rocks trend approximately NW-SE, and NNW-SSE to NNE-SSW, respectively. In the ferri- and para magnetic metavolcanic rocks, k_1 have gentle and steep plunge respectively, however neither the k_1 nor the k_3 axes plunge in the direction of impact, i.e., westward (Fig. 3.4, 3.5a, d).

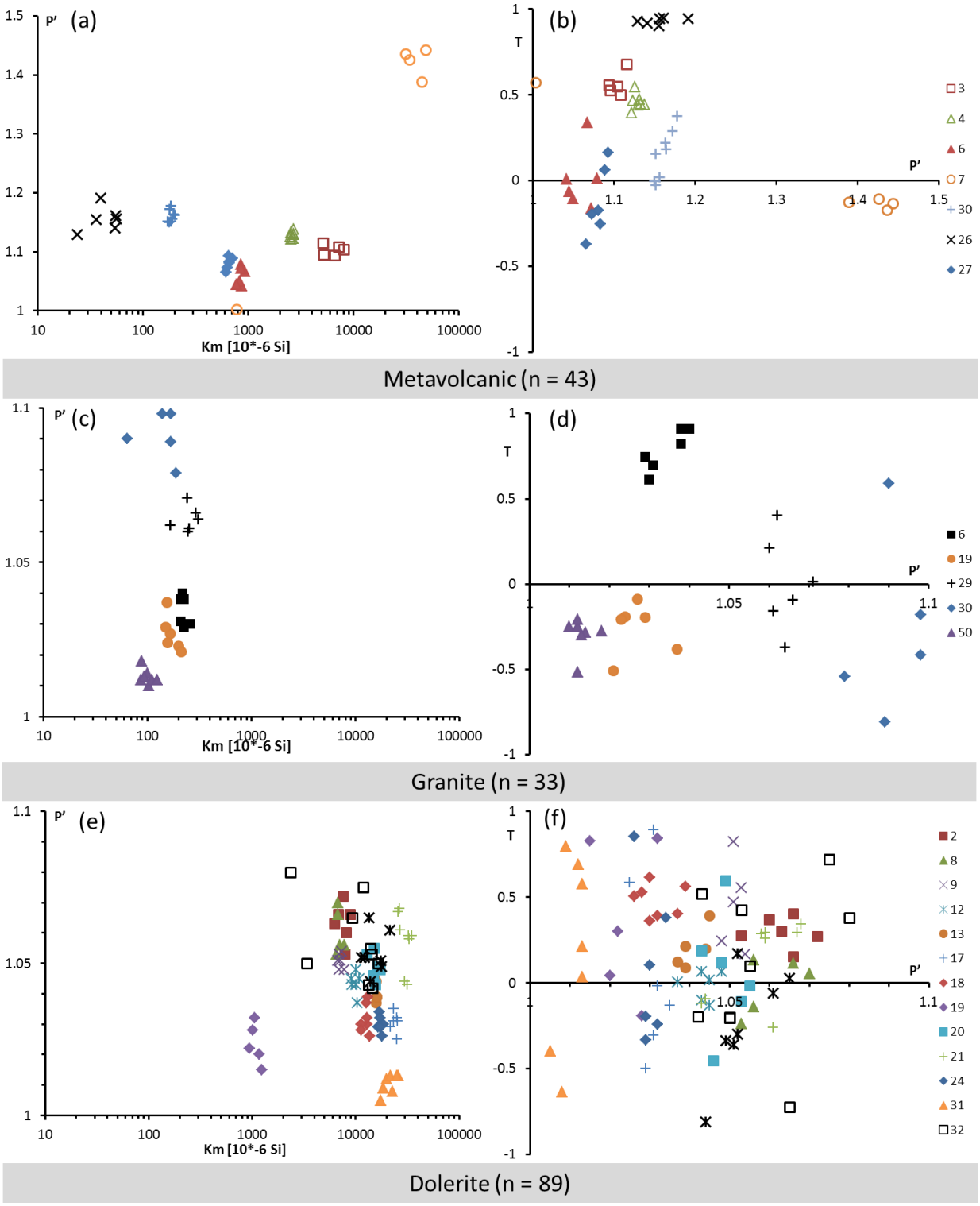

Figure. 3.3 Degree of anisotropy (P') vs. mean bulk susceptibility (k_m) (left) and shape factor (T) vs. P' (Jelinik's graphs) (right) for metavolcanic rocks, 'a' and 'b'; granites 'c, d', and dolerites 'e, f'. Each core collected from a particular sampling site is demonstrated by same symbol and in figures 'a' and 'b' the ferrimagnetic metavolcanic rocks are represented by open symbols.

Similarly, the granites show moderate to steep, oblate to prolate, randomly oriented magnetic fabrics, with P' averaging 1.045, which is independent of magnetic susceptibility (average correlation coefficient is -0.265; Fig. 3.3c, d, 3.4a, b) [166,e.g., 167–169]. The magnetic fabrics

are therefore regarded as random. It is important here, that the k_1 and the k_3 axes do not show a dominant eastward trend, which may have been a proof of shock related reorientation (Fig. 3.4a, 3.5b, e).

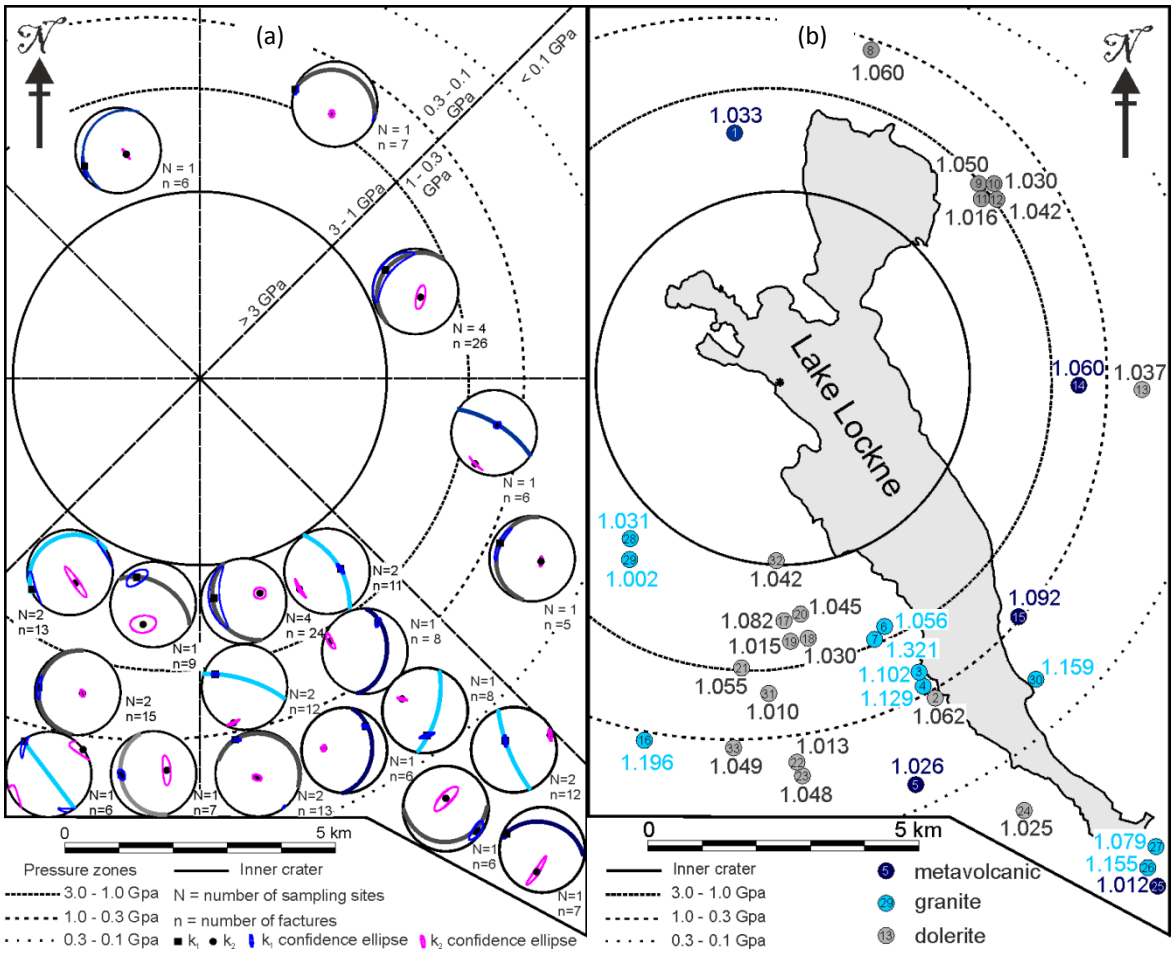

Figure 3.4 (a) Map of the Lockne area, divided into sectors based on direction and pressures, demonstrating magnetic foliations, k_1, k_3 and corresponding confidence ellipse of metavolcanic (blue), granite (violet) and dolerite (grey). The data is averaged over all the cores (n), collected from sampling site (N) in a particular sector (see Figure AF9 for data from individual sampling site). (b) Map demonstrating the degree of magnetic anisotropy averaged over all the samples from particular sampling site. The centre of the Lockne impact structure is marked by an asterisk.

In general the dolerites demonstrate oblate to prolate, gentle dipping magnetic fabrics with average P' in range of 1.043, which is independent of magnetic susceptibility (average correlation coefficient is -0.287) (Fig. 3.3e, f, 3.4b). The k_1 axes plunge gently ESE to WSW, while the k_3 axes have steep plunge in variable direction (Fig. 3.4, 3.5c, f); therefore, neither of the axes is preferentially eastward oriented.

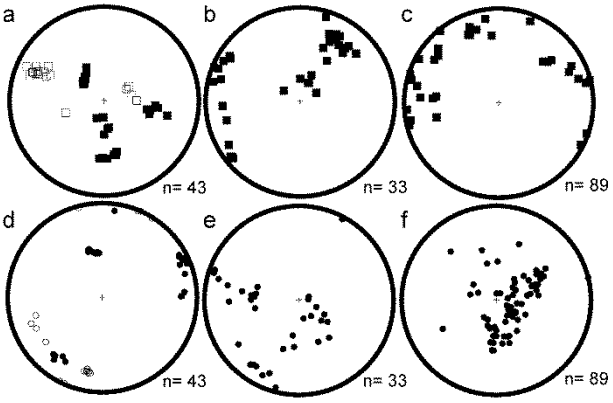

Figure 3.5 (a, b & c) Stereographic projections of k_1 of metavolcanic rocks (open squares represent the ferrimagnetic samples), granites and dolerites respectively. (d, e & f) stereographic projections of k_3 of metavolcanic (open circles represent the ferrimagnetic samples), granites and dolerites respectively. Individual cores, from each sampling site, are shown separately.

3.3 Microfractures

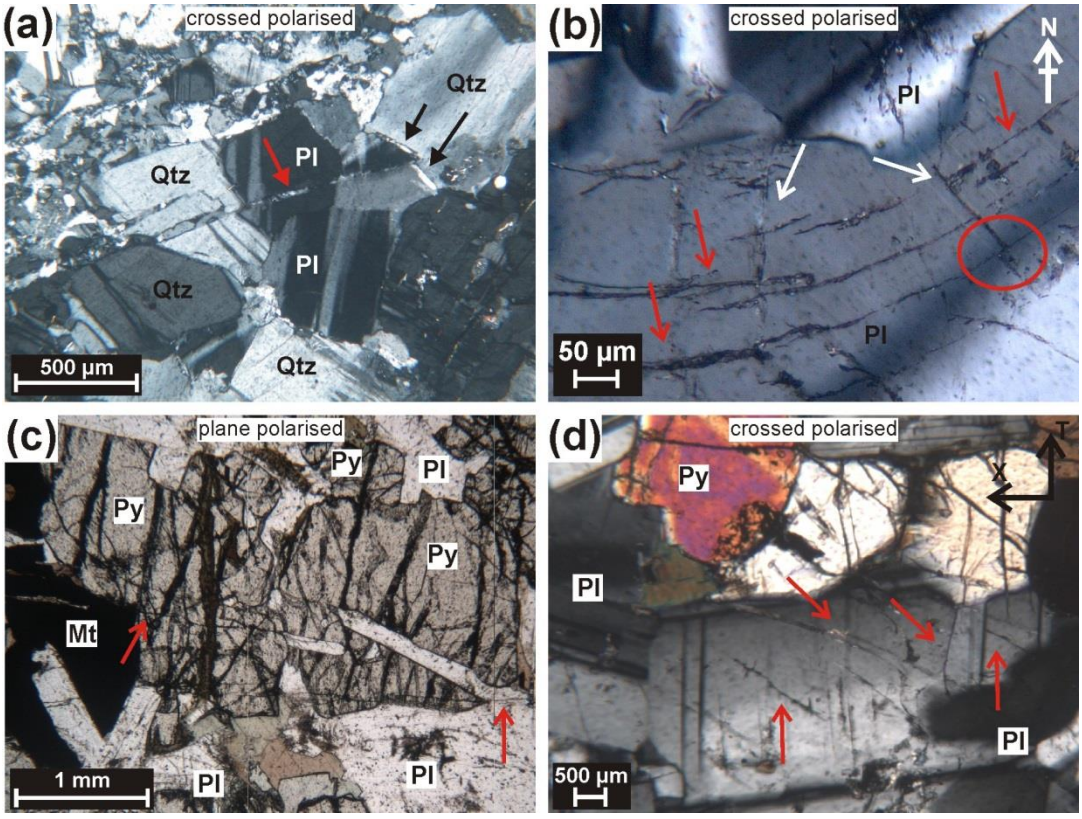

Figure 3.6 (a) Bulging recrystallization (black arrow) between quartz (Qtz) and plagioclase (Pl), cut by fracture (red arrow) filled by secondary siliceous minerals in granite. (b) Curved-concentric microfracture (red arrow) offset the straight radial ones (white arrow) in plagioclase (Pl) in dolerite. (c) Transgranular fractures across pyroxene (py) plagioclase (pl) and titanomagnetite (Mt) in dolerite. (d) Vertical and inclined microfractures. 'T' marks the top and 'X' marks 291° from north in dolerite.

Fractures in hand specimen are not very common, and a statistical analysis is difficult. However, in thin-sections they are more frequent and a more reliable quantification is possible. The metavolcanic rocks are too fine grained therefore, the study reports microfractures only from granites and dolerites. The microfractures may be divided into two

sets. (i) Those refilled by siliceous and micaceous minerals commonly show significant offset (Fig. 3.6a), which is uncommon for impact generated microfractures, formed at high strain rate. The microfractures probably formed during a pre-impact tectonic event. (ii) Those either filled by calcitic material or not filled by secondary mineral phase at all and showing no offset. The microfractures have straight traces that refract at grain boundaries. They are more common, smaller in length and probably younger than the former.

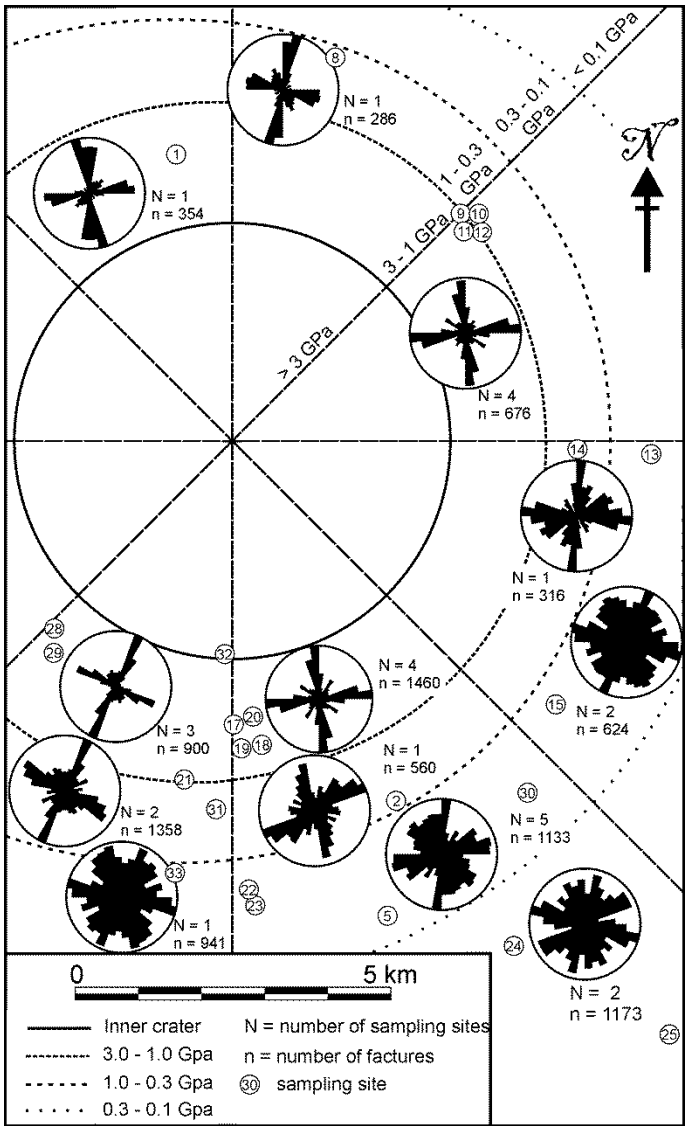

Figure 3.7 Distribution of microfractures (determined from sub-horizontal thin-sections) and shock pressure in rocks around the Lockne impact crater. The shock pressures are estimated after Lindström et al. [13]. The number of fractures used to prepare a rose diagram is indicated by 'n'. While, 'N' is the number of thin sections used. It is important here that, each thin section represents a different sampling site and entire area of the thin section was mapped.

The younger microfractures, in sub-horizontal thin-sections, are commonly arranged, at microscopic scale, in parallel sets having two distinct geometrical relationships with the impact crater, i.e., radial and concentric (Fig. 3.6b, c). In the rocks closest to the crater, that suffered shock pressures in the order of 3 – 1 GPa, the radial and concentric trends are prominent (Fig. 3.7). The trends weaken in the rocks relatively farther from the crater, that suffered lower shock pressures, in the order of 1 – 0.3 GPa. Random microfractures, with no distinguishable pattern, are common in the rocks farthest from the crater that experienced shock pressures ≤ 0.3 GPa. In one of the sample, close to the crater, concentric microfractures demonstrate curved traces, parallel to the crater (Fig. 3.6b). The overprinting relationship, i.e., concentric microfractures offsetting the radial microfractures, reveals that the

concentric microfractures are younger than the radial microfractures.

In sub-vertical thin-sections similar geometrical classification of the younger microfractures set is possible. They may be subdivided into two cross cutting subsets of oblique and vertical microfractures. The oblique microfractures, typically, dip away from the crater and are interpreted to be traces of conical microfractures which are typical of fracturing provoked by impact (Fig. 3.6d). The vertical subsets are interpreted as the manifestation of the radial and/or concentric microfractures.

3.4 Discussion

Generally, target rocks of craters are known to have magnetic fabrics, either overprinted by the shock or controlled by some other petrological features such as preferred orientation of ferrimagnetic minerals due to metamorphism. Only few magnetic studies on impact craters, e.g., Vredefort and Sudbury meteorite crater are well constrained, whereas, on other craters, e.g., Lonar crater, India the results are equivocal [12,90,156,170–173].

Beside changes in magnetic properties, high strain rate deformation in the target rocks is commonly manifested by brittle deformation, i.e., fracturing, around both experimental and natural impact craters. Dimensions of the crater and properties of the target play significant role in the distribution of the fractures [62,91,92,102,162]. Origin of shock-induced fractures is well understood in some craters, e.g., Meteor crater, El'gygytgyn crater, however, similar studies on others give contradicting results [5,62,91,174].

3.4.1 Origin of magnetic fabrics and relationship with shock pressure

The NW-SE trending foliation in ferrimagnetic metavolcanic rocks is attributed to elongated magnetite grains aligned parallel with the microscopic mylonitic foliation. Moreover, the magnetic foliation is coherent with the observed dextral shear sense (Fig. 3.1a), and parallel with the trends of regional shear zone (cf. Fig. 1.3). However, the foliations in paramagnetic metavolcanic rocks are different, i.e., NNW-SSE to NNE-SSW (Fig 3.4a, AF6). The two different fabrics in the metavolcanic rocks are interpreted as sub-fabrics developed during the same deformational event, i.e., Storsjön-Edsbyn deformation zone. The initial, simple shear dominated component led to the development of the paramagnetic fabrics, while the

ferrimagnetic fabrics and the metamorphic foliations evolved during the later pure shear dominated component of the common NE -SW oriented compressional event. In agreement, Mattsson and Elming [175] suggest that the Storsjön-Edsbyn deformation zone is a pure shear dominated transpression zone caused by a compressive stress from the present SSW. The magnetic fabrics, therefore, reflect a pre-impact, 1.82-1.80 Ga, Svecofennian tectonic event. We can, therefore, conclude that the magnetic fabrics in the metavolcanic rock owe their origin to the metamorphic events and not to the impact.

The magnetic fabrics in granite are prolate to oblate and variably oriented (Fig 3.4a, AF6) showing no preferred orientation, which was expected in case of shock induced reorientation [e.g., 90]. The k_1 and k_3 show gentle and steep plunges respectively, in variable directions (Fig. 3.5b, e). Therefore neither of them demonstrates a westward preferred orientation, sub parallel with the shock direction, as expected in case of reorientation of either of the axes.

The magnetic foliation in dolerite are gently dipping to horizontal, and the k_1 and k_3 show gentle and steep plunge respectively, in variable directions (Fig. 3.4a, 3.5c, d, AF6). In agreement to the regional flat-lying trend of the dolerite sills and dykes [83], the magnetic fabrics represent magmatic emplacement and simultaneous plastic deformation, which is also manifested in curved and deformed plagioclase crystals (Fig. 3.1f). As discussed earlier, shock related re-orientation should have resulted in a westward preferred orientation of k_1 or k_3, however absence of any preferred orientation strongly suggests lack of any shock effect.

We summarize that neither the k_1 nor the k_3 axes of the ferrimagnetic and the paramagnetic crystalline basement rocks show any preferred orientation (Fig. 3.5). Furthermore, we do not observe any change in the magnetic anisotropy of ferrimagnetic or paramagnetic rocks with respect to the distance from the crater (Fig. 3.4b).

After negating the possible reorientation of magnetic fabrics due to shock, we will attempt to predict shock pressure range in the rocks. The present results when interpreted in light of studies on target rocks of experimental and natural craters [6,7, section 1.5.1,10,90] suggest that the shock pressure were in the order of < 0.5 GPa, in the rocks around the inner crater. It is important here, that the analogues used, deal with target rocks with same magnetic mineralogy as ferrimagnetic metavolcanic and dolerite in Lockne.

In contradiction to our estimates of < 0.5 GPa, higher shock pressure, i.e., 3 to 1 GPa, is suggested by Lindström et al. [13] in rocks around the inner crater up to a distance of 2 km from it (Fig. 1.5). A possible explanation could be that they employed 2D shock pressure modelling with an objective of replicating the impact cratering processes [13]. The smallest particles considered are 10 cm in size and, therefore, the estimated shock pressures represents those in rocks at least 10 cm in size [13,14,176]. As commented by Sharp and Decarli [177], such modelling averages over local fluctuations. Accordingly, a microscale inhomogeneity in pressure will be overlooked by the models. However such inhomogeneity will affect the magnetic domains, which are micrometer size, and will be detected in AMS investigations.

3.4.2 Origin of the microfractures and comparison with experimental and natural impact craters

Around the Lockne crater, impact generated fractures are common in surface outcrops up to a distance of twice the radius of the inner crater [73]. They are distinguished, in thin-sections, from other, older microfracture sets based on the geometry and fillings of secondary phases (Fig. 3.6a).

Similar to the radial and concentric microfractures observed in the horizontal thin sections (Fig. 3.6b), Polanskey and Ahrens [92] demonstrate radial and concentric fractures through shock experiments. Commonly, the radial and concentric microfractures observed in experimental [92] and natural craters [62] are vertical. Correspondingly we interpret that the vertical microfractures observed in the vertical thin-sections (Fig. 3.6d) are traces of radial and concentric microfracture sets. However, the oblique microfractures in the vertical thin sections consistently dip away from the crater (Fig. 3.6d). The observations on the experimental and natural craters by Polanskey and Ahrens [92] and Kumar [62] suggests these oblique microfractures may represent traces of typical conical microfractures. These microfractures, in map view, show traces similar to the concentric microfractures, and are therefore not distinguished in horizontal thin sections. We therefore propose that Lockne impact provoked three types of microfracture sets, with distinct geometry, namely: radial, concentric and conical.

A review of the orientation of the microfractures from sub-horizontal thin-sections (Fig. 3.7) reveals that the orientation maxima of the microfractures become less prominent, with distance from the impact crater. This result is in accordance with those shown by Ahrens [162], and suggests that the damage is most significant in the crater wall, and is reduced farther away from the crater. It is noteworthy that the microfractures in the experiments (Fig. 1.4) extend up to several times the crater radius, only in the sub-surface [92]. However, at Lockne impact structure we observe them in sub-areal rocks extending much farther than expected from the shock experiments. A possible explanation may be that the post impact exhumation and erosion in Lockne area led to exposure of the fractured rocks present originally in the subsurface.

The crystalline basement rocks were overlain by few kilometres of Caledonian nappe, several tens of meters of Silurian sediments [86,178]. The fractures, resulting from pressure released due to exhumation [179–181], may be confused with those of an impact origin. However, contrary to the sub-horizontal pressure release fractures [182–184], those reported in this study are vertical or steeply inclined.

Chronology of microfractures and relationships with shock pressures

Radial and concentric fractures around micrometre scale impact craters on solar panels of a spacecraft demonstrate chronological relationships [102]. In some craters, the radial microfractures postdate the concentric microfractures and vice versa [91,102]. In Lockne, the concentric microfractures offset the radial ones and are, therefore, younger (Fig. 3.6b). Moreover, shock experiments reveal that the radial fractures are formed immediately behind the outgoing stress wave [92,105,185], whereas the concentric fractures are initiated by the tensile phase of the stress wave associated with sudden release of the impulsive force [42,105]. The overprinting relationship in Lockne, therefore, shows that the older radial microfractures formed during the initial compressive phase and the younger concentric microfractures formed during the tensile phase of the shock wave.

A comparison among the shock pressures, estimated by Lindström et al. [13] and microfracture trends reveals strong preferred orientation, i.e., radial and concentric, in rocks experiencing shock pressures, 3 – 1 GPa. Less preferred orientation is observed in rocks, suffering shock pressures, 1 - 0.3 GPa. The rocks farther than about 6.5 km from the crater centre, that suffered low shock pressures (<0.3 GPa) show random distribution of

microfractures. The observations are in agreement with Hörz [9] and Lambert [8], who demonstrate correlation between fracture density and shock pressure, ≥ 0.2 GPa, and suggest that below the pressure limit, the fractures cannot be characterized.

4. Shock induced shear zone and localization of stresses

4.1 Preamble

Impact craters form in a highly dynamic and complex system that subjects the target rocks to numerous interfering deformation mechanisms, occurring at different spatial scales. Among the various deformation mechanisms, those which lead to formation of high pressure-temperature (P-T) crystalline phases at grain interfaces are not completely understood [18,186].

Theoretical studies suggest that progress of shock waves across interfaces oriented perpendicular to the shock wave-front between materials with significant impedance contrasts may lead to local stress concentrations [16,43] or to localized shearing and heating [16,48]. In agreement to these theoretical studies, shock localization leading to phase transformations have been experimentally produced along interfaces between dunite and quartzite [18]. On the one hand, transformation of plagioclase to lingunite, at very high P-T, is well known in meteorites, e.g. Sixiangkou meteorite [20], Taiban chondrite [187]. On the other hand, natural lingunite has not yet been reported from terrestrial target rocks, even though more than 200 terrestrial impact craters have been identified [3]. However, shock localization and shearing resulting in melting and vaporization is already reported from the terrestrial target rocks of the Sudbury impact crater [17].

Therefore, the following questions need to be answered: “Is shock induced transformation of plagioclase and formation of its crystalline, high P-T, polymorphs possible in natural terrestrial impact target rocks?” and “What is the crucial deformation mechanism at interfaces, between minerals with contrasting mechanical properties, that may lead to such polymorphism even at relatively low peak shock P-T?”

We use the terms “peak pressure” and “peak temperature” for the averaged peak P-T values determined by using measurement techniques that average over the local variations. The terms “pressure spike” and “temperature spike” are used for the temporal, nanosecond-duration, peak in P-T at a sub-micrometre scale [177].

During the study of impact generated microfractures developed at augite-labradorite grain boundaries we observed for the first time, in terrestrial target rocks, natural lingunite. Lingunite, a tetrahedral, high P-T polymorph of Na-plagioclase was, for the first time synthesized by Liu [19] and was discovered in meteorites by Gillet, et al. [20]. To understand

the shock-induced phase transformations, we used a combination of scanning electron microscopy (SEM), micro-Raman spectroscopy, and transmission electron microscopy (TEM).

4.2 Microtextures in target dolerites from the Lockne impact structure

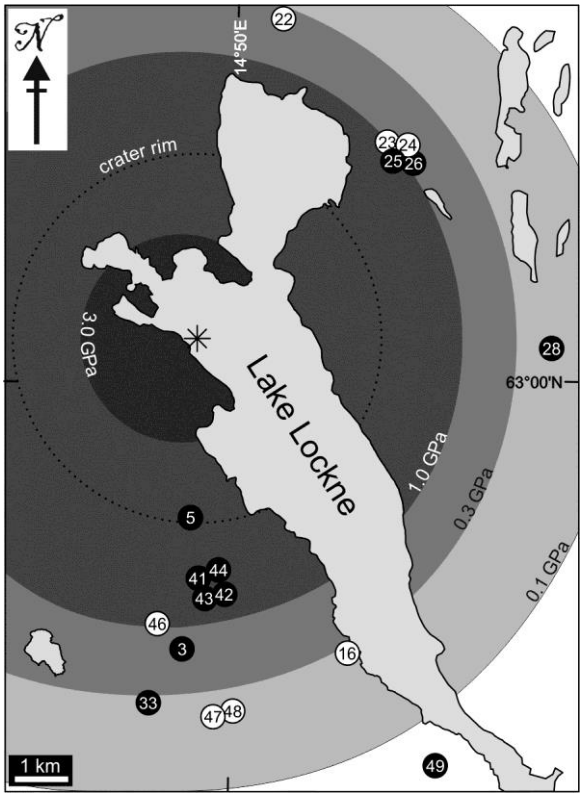

Figure 4.1 Map of the Lockne crater area showing the distribution of shock pressures, estimated after Lindström et al. [13]. The sample locations of dolerites are shown by dots. Black dots: lamellae of augite and plagioclase (s. Table AT7 for GPS locations). Sample '49' was used for further detailed investigations.

Table 4.1. Electron dispersive X-ray (EDX) analyses showing labradorite and bytownite.

Oxide	Labradorite		Bytownite	
	Weight %	error weight%	Weight %	error weight%
Na_2O	4.62	+/- 0.07	2.46	+/- 0.09
Al_2O_3	25.33	+/- 0.10	30.16	+/- 0.15
SiO_2	60.13	+/- 0.15	51.67	+/- 0.19
K_2O	0.81	+/- 0.04	-	-
CaO	9.12	+/- 0.07	15.71	+/- 0.13

The dolerites from the Lockne impact structure are characterized by a typical assembly of olivine (ol), augite (au) and plagioclase (Fig. 4.2a). Through energy dispersive X-ray spectroscopy (EDX) the plagioclase is classified into labradorite (la) and bytownite (byt) (Table 4.1). In many dolerites augite-plagioclase grain boundaries demonstrate a series of alternating augite and plagioclase lamellae (Figs. 4.1, 4.2).

This geometry is important because, as mentioned above, more intense effects of shock may be expected along the interface between augite and labradorite. For investigating shock effects on the interface, the sample 49 was selected as the augite and labradorite lamellae are best developed in it.

In fact, the augite and plagioclase lamellae are normal to the radial microfractures (Fig. 4.3) which converge at the crater centre and formed parallel with the propagation direction of the outward radiating shock wave (Fig. 4.3). The radial microfractures formed early, probably during the compressive phase of the shock wave (s. sect. 1.5.1, 3.3, 3.4.2). Although,

according to published data [13], the shock waves were relatively weak, occurrence of such microfractures emphasizes that the shock waves still caused some deformation.

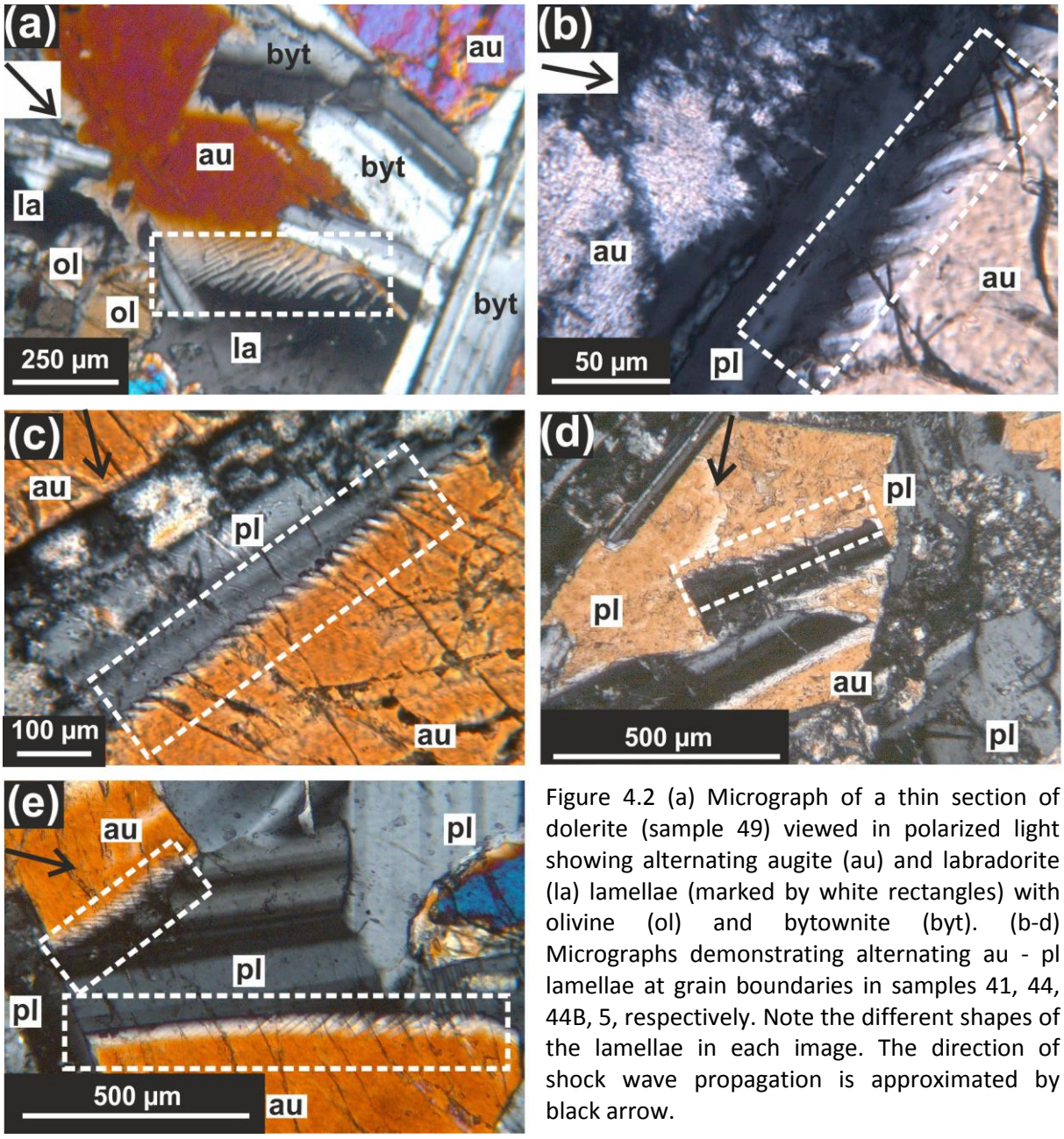

Figure 4.2 (a) Micrograph of a thin section of dolerite (sample 49) viewed in polarized light showing alternating augite (au) and labradorite (la) lamellae (marked by white rectangles) with olivine (ol) and bytownite (byt). (b-d) Micrographs demonstrating alternating au - pl lamellae at grain boundaries in samples 41, 44, 44B, 5, respectively. Note the different shapes of the lamellae in each image. The direction of shock wave propagation is approximated by black arrow.

The SEM observations reveal that the labradorite and augite lamellae are, in 2D, almost normal to the radial microfractures and to the shock propagation direction (Fig. 4.3). It is important here that the thin section and the micrographs are slightly oblique to the shock direction. The lamellae appear, therefore, as slightly oblique to the shock direction in the SEM images (Fig. 4.4a). However, when plotted in 3D, these augite and plagioclase lamellae are normal to the radial fractures and also to the shock direction (Fig. 4.3b). The geometry of the lamellae is comparable with those of concentric fractures experimentally shown by Ahrens

and Rubin [42]. These authors suggested that such concentric fractures form during to the decompressive phase of a shock wave, and are oriented normal to the shock direction and to the radial microfractures (s. sect. 1.5.1, 3.3, 3.4.2).

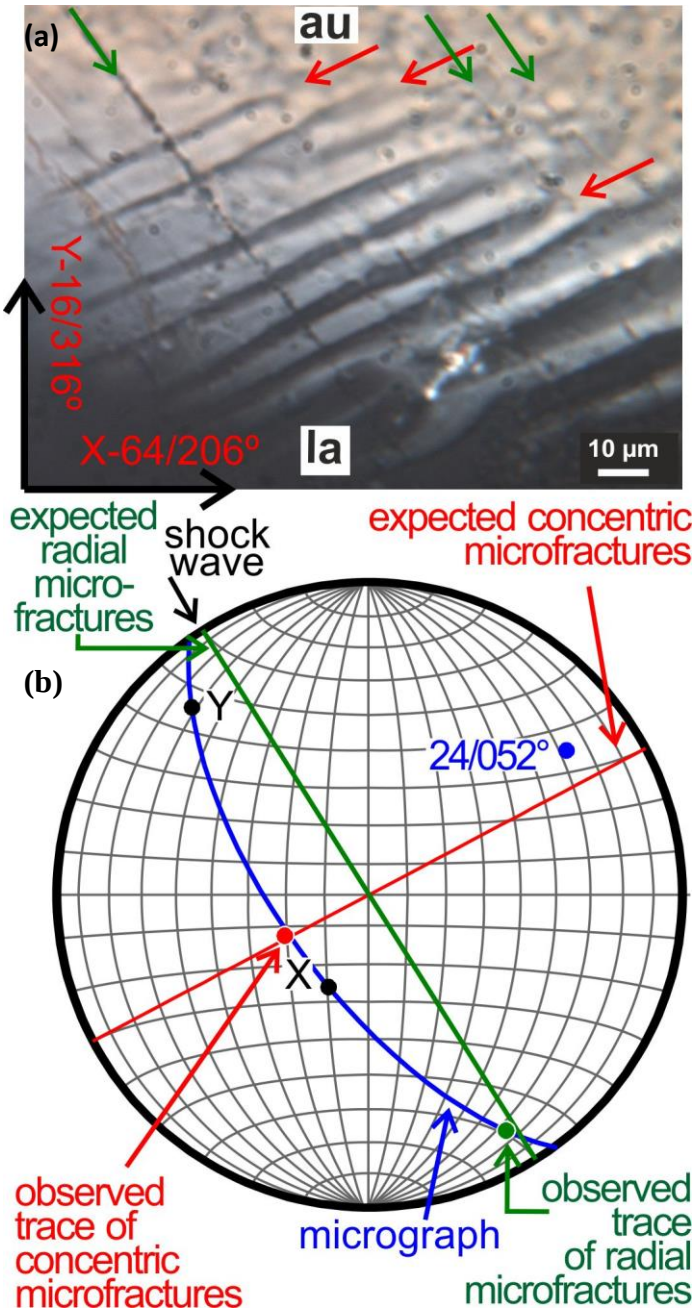

Fig. 4.3a Enlarged part of an area within white rectangle in figure 4.2a, showing impact generated radial and concentric microfractures with green and red arrows, respectively (sample 49, oriented in original position using X = 64°/206° and Y = 16°/316°).

Fig 4.3b Stereonet demonstrating the orientation of the above micrograph (blue arc), which was determined using 'X' and 'Y'. 24/052° is the pole to the micrograph. The stereonet also shows the direction of shock wave propagation (black arrow), determined on the basis of directional relationship between the centre of the impact crater and the position of sample 49 in figure 4.1. The rake of 'the trace of the radial and concentric fracture' was calculated with respect to 'X' in the above micrograph and is shown with red and green points, respectively Earlier workers show concentric microfractures develop perpendicular to and radial parallel with the shock direction. The expected concentric and radial microfractures are shown with red and green arcs, respectively.

Impact generated radial microfractures are present in augite lamellae but not in the labradorite lamella (Fig. 4.4b). The observation imply that the radial microfractures are overprinted by the younger labradorite lamellae, which formed by deformation that was active after the development of the radial microfractures. The evidence of an even later stage shock wave-induced deformation is the radial microfractures filled with labradorite from adjacent lamellae (Fig. 4.4b). The later stage, shock wave-induced, deformation may have pushed the labradorite from adjacent lamellae into the microfractures.

Table 4.2. Results from EDX analyses during SEM, showing major oxides of labradorite (1), augite (2), the respective lamellae (2, 4), and the labradorite-augite interface (5). Schematic positions of EDX analyses are shown in supplementary figure 3.

Oxide	Labradorite				Augite				Augite-Labradorite lamellae interface	
	Position 1		Position 2		Position 3		Position 4		Position 5	
	Weight %	error weight%	Weight %	error weight%	Weight %	error weight%	Weight %	error weight%	Weight %	error weight%
Na_2O	47.68S	---	5.14	+/- 0.12	---	---	---	---	5.22	+/- 0.14
MgO	---	---	---	---	11.37	+/- 0.16	11.76	+/- 0.13	1.27	+/- 0.09
Al_2O_3	3.82	+/- 0.12	25.71	+/- 0.19	2.43	+/- 0.08	2.3	+/- 0.07	20.25	+/- 0.13
SiO_2	13.61	+/- 0.19	59.1	+/- 0.28	50.63	+/- 0.18	50.9	+/- 0.16	61.73	+/- 0.22
K_2O	27.63	+/- 0.28	0.8	+/- 0.07	---	---	---	---	0.49	+/- 0.08
CaO	0.66	+/- 0.07	9.24	+/- 0.24	23.33	+/- 0.21	21.5	+/- 0.27	9.28	+/- 0.27
Fe_2O_3	---	---	---	---	11.07	+/- 0.61	12.28	+/- 0.56	1.76	+/- 0.26
TiO_2	---	---	---	---	1.16	+/- 0.11	1.26	+/- 0.11	---	---

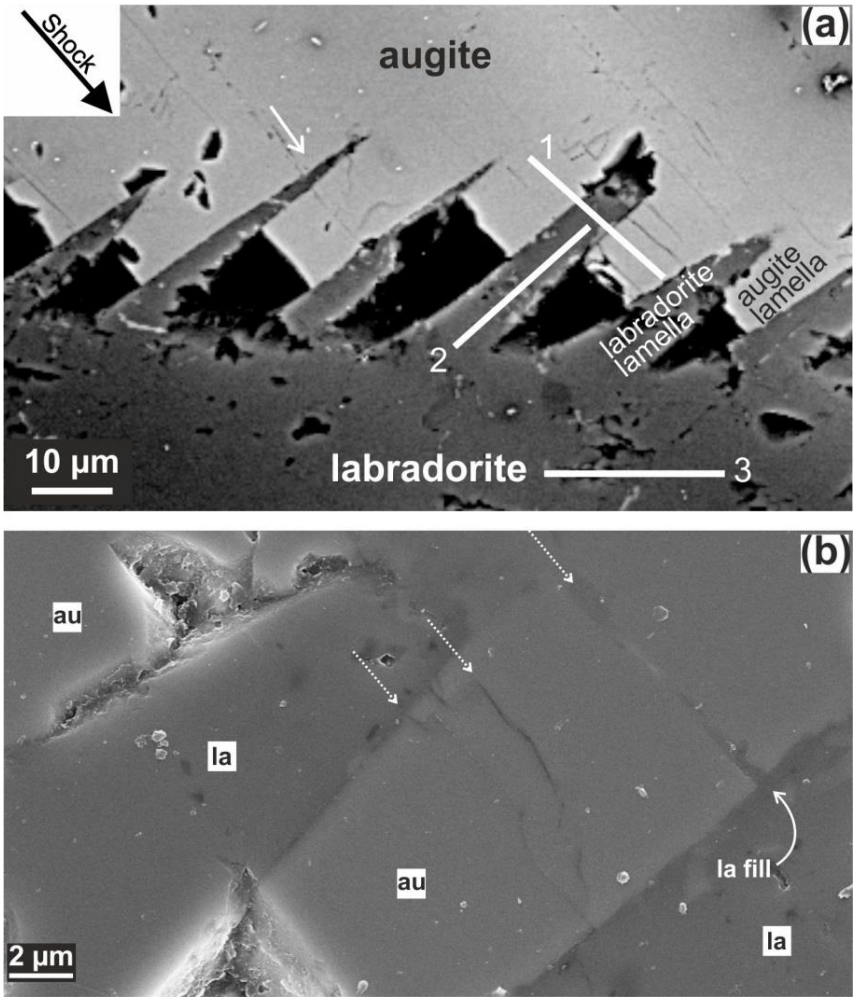

Figure 4.4 (a) BSE image showing the impact generated radial microfractures (white arrow) parallel with the shock direction. The augite and labradorite lamellae exhibit straight boundaries. White lines schematically mark the area from where focused ion beam TEM sections were prepared: 1 at augite-labradorite lamellae interface, 2 in the labradorite lamella and 3 in the bulk labradorite. (b) High resolution SEM image of augite (au) and labradorite (la) lamellae. The radial microfractures (white dashed arrows) in augite lamella cease in the adjacent labradorite lamellae. Curved arrow marks a radial microfracture filled with labradorite from adjacent lamella.

The fact that the bulk labradorite and augite grains and their respective lamellae are chemically identical (Table 4.2) precludes any chemical diffusion or re-melting and supports the idea that, the lamellae are deformational features, probably formed due to shock waves.

The chemical composition of the augite-labradorite lamellae interface is a mixture of augite and labradorite, and there is no evidence of a third mineral phase with different chemical composition at the interface (Table 4.2). Since a chemical analysis, such as EDX, is unable to detect possible shock induced polymorphs of either augite or labradorite, we used micro-Raman spectroscopy to identify such phases.

4.3 Micro-Raman spectroscopy of phase transformations

Two separate spatially-resolved investigations were done with micro-Raman spectroscopy (Fig. 4.5a). First, for investigating a possible phase transformation at the lamellae interface, Raman spectra were acquired from the bulk augite and labradorite (i.e. from points located away from the augite and labradorite lamellae) and from the augite - labradorite lamellae interface (Fig. 4.5a). Second, for checking if the labradorite lamellae are, indeed, impact generated fractures in augite, the Raman spectra were acquired within the lamellae as function of increasing distance from the bulk labradorite grain (Fig. 4.5a, Fig. AF8).

The spectra from bulk minerals are comparable to that of labradorite and augite reported elsewhere [188–190] and are in good agreement with our petrological and EDX results (Fig. 4.2, 4.5b, Table 4.2). The spectrum from the augite-labradorite lamellae interface shows active bands that may be attributed to either labradorite or augite (Fig. 4.5a). In addition, 820 cm^{-1} band is unique in spectrum from the interface. The 820 cm^{-1} band is neither characteristic of augite nor labradorite [188,compare with 189,190]. We compared this band with the published Raman spectra of possible high P-T transformation phases of labradorite and augite, such as quartz (SiO_2), stishovite (SiO_2), coesite (SiO_2), jadeite ($NaAlSi_2O_6$), wadeite ($K_2Si_4O_9$), lingunite ($NaAlSi_3O_8$-hollandite), kyanite (Al_2SiO_5), majorite ($Mg_3(Fe,Al,Si)_2(SiO_4)_3$), and pervoskite ($(Mg,Fe)SiO_3$) [190–194].

The comparisons reveal that the 820 cm^{-1} band is comparable with most intense band of the lingunite spectrum, which varies between 760 and 900 cm^{-1} (cf. figure 4.5d) [192]. The band, characteristic of SiO_6 octahedral stretching vibrations, corresponds to splitting of A_{1g} mode [192]. Moreover, shift of this particular band from its normal value of 760 cm^{-1} is indicative of in-situ pressure [192], which in turn suggests a deformed crystal lattice. The position of this 820 cm^{-1} band is indicative of about 19 GPa of in-situ pressure (Fig. 4.5d) [192].

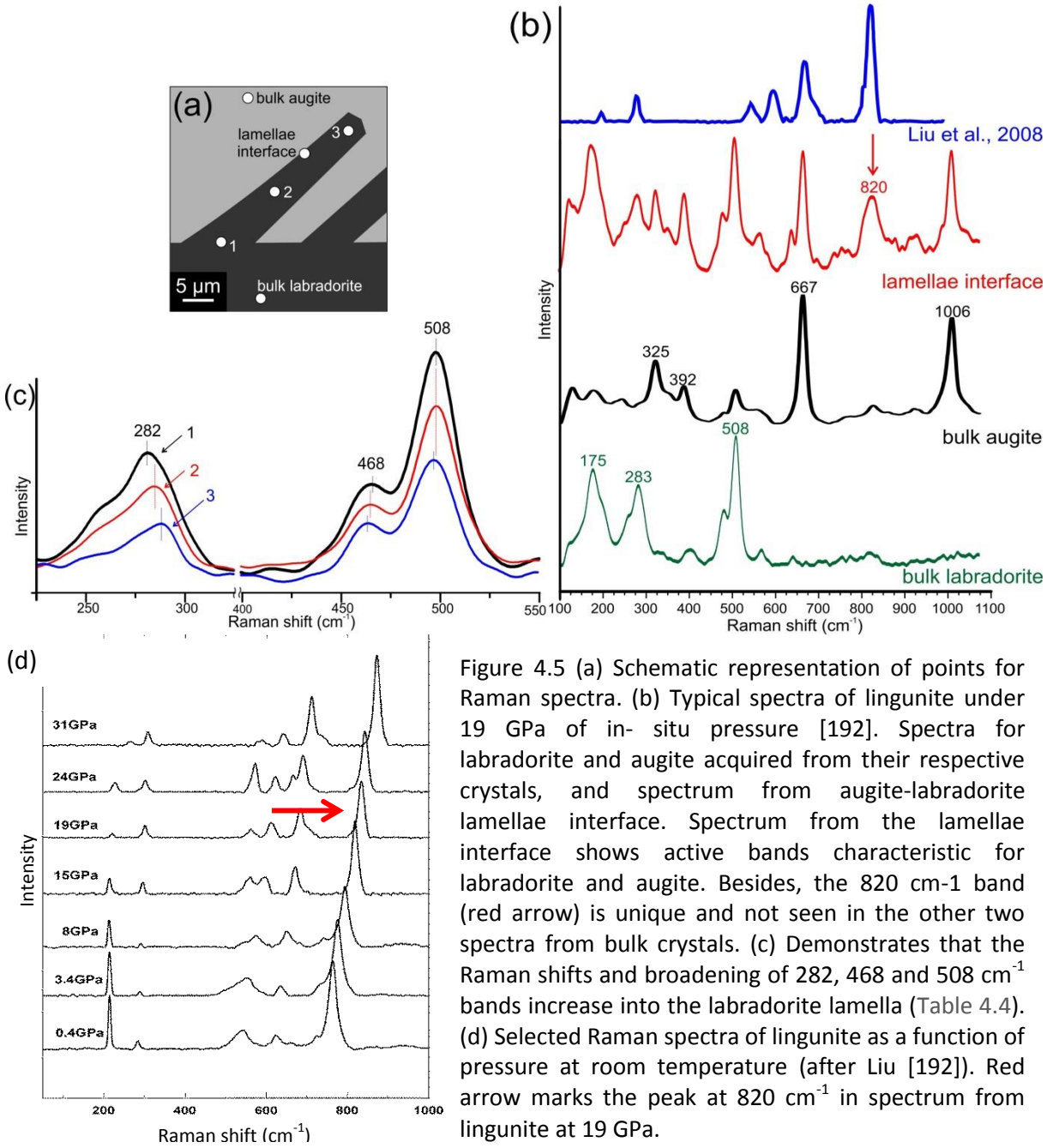

Figure 4.5 (a) Schematic representation of points for Raman spectra. (b) Typical spectra of lingunite under 19 GPa of in- situ pressure [192]. Spectra for labradorite and augite acquired from their respective crystals, and spectrum from augite-labradorite lamellae interface. Spectrum from the lamellae interface shows active bands characteristic for labradorite and augite. Besides, the 820 cm-1 band (red arrow) is unique and not seen in the other two spectra from bulk crystals. (c) Demonstrates that the Raman shifts and broadening of 282, 468 and 508 cm^{-1} bands increase into the labradorite lamella (Table 4.4). (d) Selected Raman spectra of lingunite as a function of pressure at room temperature (after Liu [192]). Red arrow marks the peak at 820 cm^{-1} in spectrum from lingunite at 19 GPa.

The broad shape of the 820 cm^{-1} band suggests either a deformed crystal lattice and/or semi-amorphization of the material with many, variably oriented nano-crystals [195]. It is important to note that the lingunite identified along the interface, is a polymorph of labradorite, and therefore cannot be identified in SEM images (Fig. 4.4) or detected by EDX-analysis (Table 4.2), which was done with a beam of actual diameter of 1-2 µm.

Three bands, 282 cm^{-1}, 468 cm^{-1} and 508 cm^{-1}, which are assigned to the external lattice modes, a mixed Si-O-Si (or Si-O-Al) bending/stretching and A_g vibrational mode respectively [188], are compared among the Raman spectra, obtained within the labradorite lamella as a

function of distance from the bulk grain (Fig. 4.5a, 4.5c). The bands broaden farther into the lamellae, such that the full width at half maximum (FWHM) at the edge of the labradorite lamella (pt. 3 in Fig. 4.5a) is 12 to 15% higher than FWHM at the other end (pt. 1 in Fig. 4.5a, Table 4.3). Moreover, the bands shift, gradually and symmetrically either to higher or to lower values on moving towards the labradorite lamella margin (Fig. 4.5c; Table 4.3). Shift of the bands either to higher or lower values is attributed to the anisotropic straining of labradorite, which is also common in other triclinic minerals [196]. The gradual broadening and Raman shift in labradorite lamellae emphasizes that the lamellae are deformed [195] and the deformation increases towards the margin of the lamella.

Position 1		Position 2		Position 3	
peak (cm^{-1})	FWHM	peak (cm^{-1})	FWHM	peak (cm^{-1})	FWHM
281	36.536	285	38.133	288	42.072
466	9.977	465	10.625	463	11.497
498	17.486	498	17.790	497	19.587

Table 4.3. The Raman active bands demonstrate an increase in FWHM and shift in position farther into the labradorite lamella. See Fig. 4.5a for position of analysis points 1, 2 and 3.

For cross checking the Raman spectroscopy results, i.e., presence of deformed lingunite, possibly in association with amorphous material at the lamellae interface, and increase in deformation farther into the labradorite lamellae, further structural investigations were done at the nm-scale using TEM. Moreover, we attempt to answer the question "What type of shock induced lattice defects, if present, accompany the deformation in lingunite and labradorite?"

4.4 Transmission electron microscopy of augite-labradorite lamellae boundary

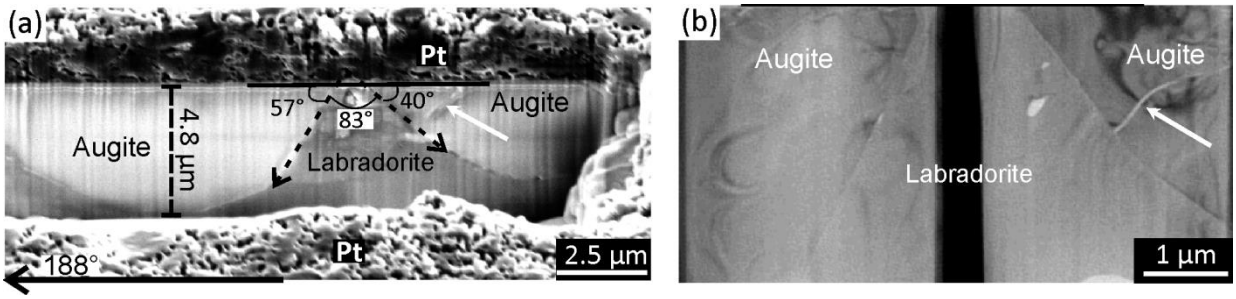

Figure 4.6 (a) 'TEM-1' section, oriented at 188° from north, before being removed from the rock thin-section, which is covered by layer of platinum (Pt). Vertical striations, observed on the TEM section are due to FIB milling. The section is thicker towards the bottom, and therefore the straight augite-labradorite lamella margins appear curved. The lamellae margin make angels of 57° and 40°, respectively, from the top surface of the TEM section (b) Overview TEM image of the 'TEM-1' section. Note the microfracture in augite, which is also seen in (a) is absent in labradorite. While acquiring this image the TEM section was not perpendicular to the camera and therefore the angle between the margins is less than 83°.

For high resolution TEM (HRTEM), three critical focused ion beam samples were prepared across the labradorite-augite lamellae interface, within the labradorite lamella and in labradorite bulk crystal (Fig. 4.5a).

Earlier, in the polarized light micrograph (Fig. 4.3a) and the SEM image (Fig. 4.4b) it is observed that the radial microfractures are present in augite lamellae but absent in labradorite lamellae. Similarly, in TEM (Fig. 4.6) the radial microfractures are present only in the augite lamellae.

Selective area electron diffraction (SAED) generated from augite part of 'TEM-1' lamella (Fig. 4.7d, 4.7e) was analysed by 'JEMS' software. The results reveal that the SAED pattern is generated from the $(\bar{1}01)$ face of the augite crystal. The c-axis of the augite is, therefore, perpendicular to the plane of the SAED and to the 'TEM-1' lamella.

SAED generated from labradorite part of 'TEM-1' lamella (Fig. 4.7a), demonstrates spots used to estimate 'hkl' indices, and corresponding interplanar distances (d1, d2 and d3), and angles (α13, α23 and α12; Fig. 4.7b and 4.7c). The parameters are well comparable with those calculated from the literature using 82-1450 powder diffraction file of a tetragonal hollandite, a = 9.873 Å and c = 2.851 Å, Botkovitz, et al., [197], (Table 4.4).

Table 4.4. Comparison of interpalanar distances, 'd (1, 2, 3)', in Å and angles, 'α (1 3, 2 3, 1 2)' in degrees, calculated from literature 'calc.' using shown 'hkl' indices and resulting zone axis 'uvw', with those observed in the study 'obs'. The parameters were calculated using 82-1450 powder diffraction file of a tetragonal hollandite, a = 9.873 Å and c = 2.851 Å, Botkovitz, et al. [197].

	D1	D2	D3	α13	α23	α12	H1	K1	L1	H2	K2	L2	H3	K3	L3	U	V	W
Calc.	6.55	1.46	1.31	53.1	10.3	63.4	1	1	0	-2	6	0	-1	7	0	0	0	-1
Obs.	6.55	1.41	1.28	53.1	8.2	61.3	1	1	0	-2	6	0	-1	7	0	0	0	-1

The augite-labradorite lamellae interface was investigated, through high resolution transmission electron microscopy (HRTEM), in further detail, figure 4.8, 4.9. HRTEM image demonstrates well-ordered augite crystal juxtaposing the randomly oriented, 60 to 150 nm^2 large, nano-crystals embedded in an amorphous phase (Fig. 4.8a). The fast Fourier transformation (FFT) diffractogram (Fig. 4.8a) of the HRTEM image (Fig. 4.8b) shows diffractions spots, characteristic of lingunite (1-1') and augite (2-2'). The spots, 1-1' and 2-2',

are used for generation of inverse fast Fourier transformation (IFFT) diffractograms of lingunite and augite respectively (Fig. 4.8c, 4.8d).

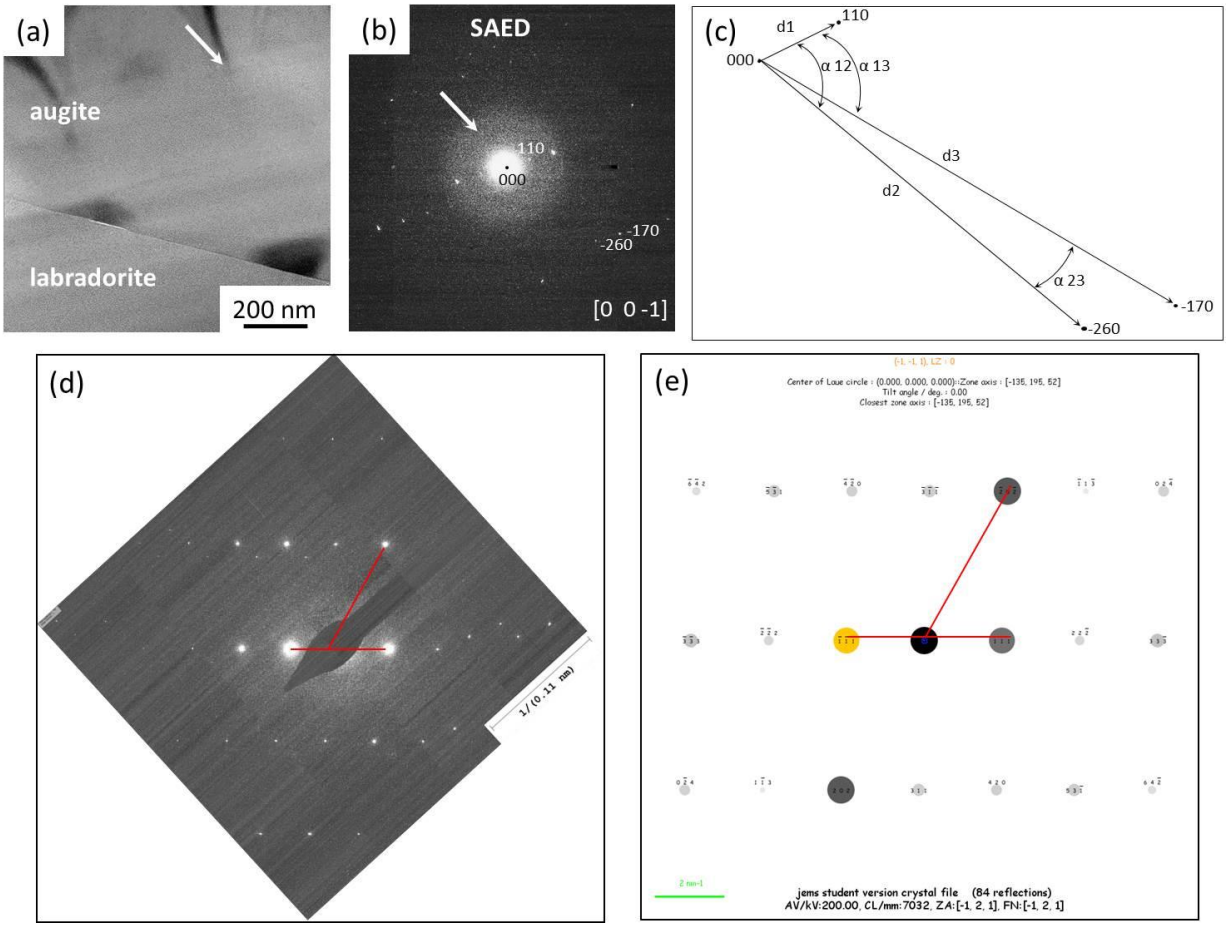

Figure 4.7 (a) TEM image of augite-lingunite interface, demonstrating bended contours (white arrow), which are more common in augite. The bended contours may represent stressed crystal lattice (b) SAED of the TEM section, from the labradorite side of the interface, demonstrating white halo (marked by the arrow) representing diffraction from amorphous material. The diffraction spots show a pattern typical for polycrystalline material. After calculating the interplanar distances and angles the spots are suggested to be of lingunite. (c) Schematic representation of the characteristic diffraction spots. (d) SAED from the augite part of the TEM section demonstrating diffraction spots forming a typical single crystal pattern of augite. The distribution of spots (red lines) was analysed by 'Jems software'. (d) Best fitting diffraction pattern calculated form Jems software. Note that the image has been enlarged keeping a constant aspect ratio.

The IFFT diffractogram representing augite, Fig. 4.8c, shows (100) planes that are separated from each other by 2.98 Å. This distance is slightly lower than values reported for synthetic augite (2.99 Å) by Sanc [198], probably due to additional amounts of Ca in crystal structure.

It is noteworthy that in the sample across the augite-labradorite lamellae interface, TEM-1, the augite crystal is situated above the labradorite crystal (Fig. 4.6). In a FIB station the ion beam source is present above the sample. The ion beam source was, therefore, closer to the

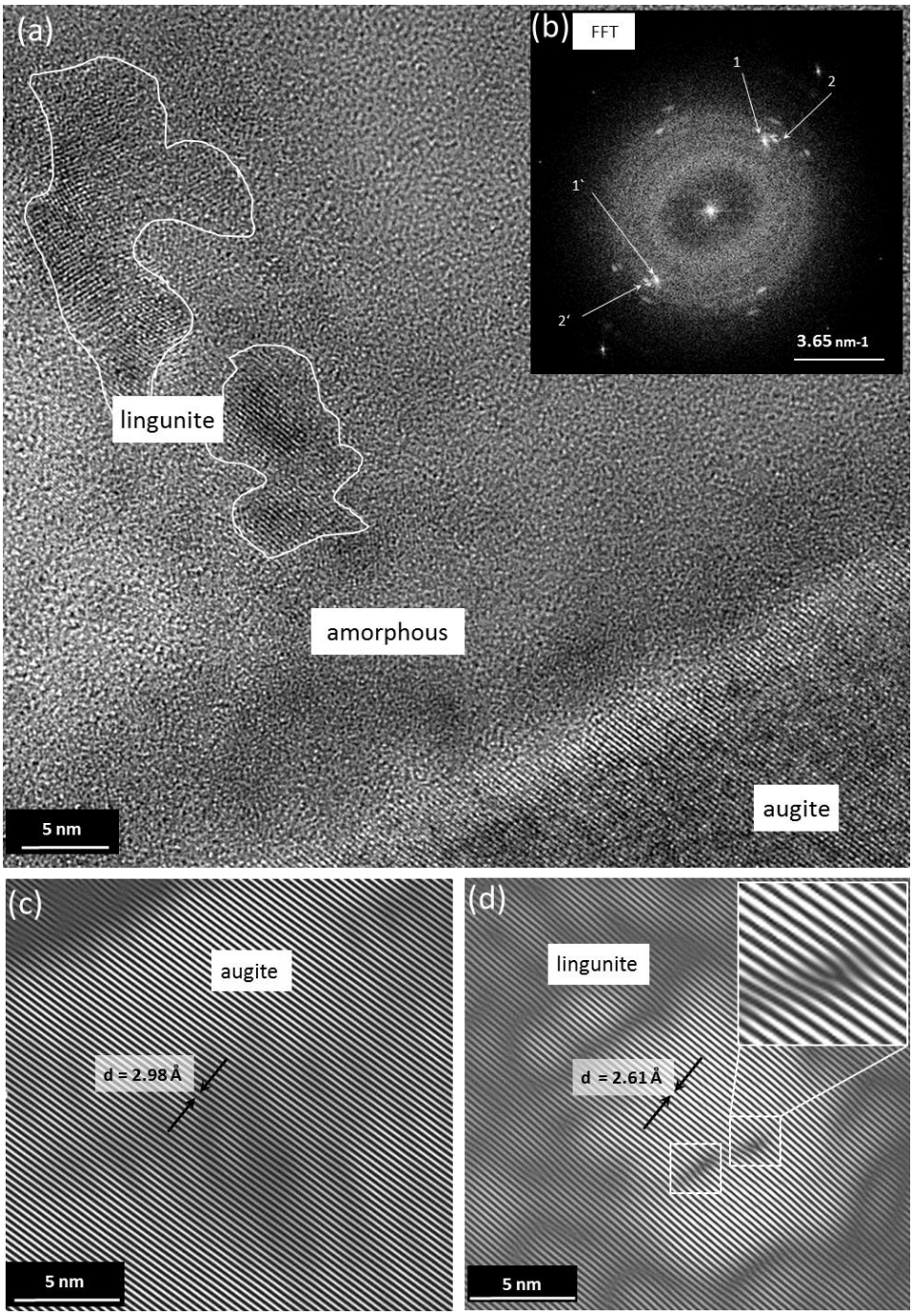

Figure 4.8 HRTEM analysis of the augite-labradorite lamellae interface. (a) Well-crystallized augite juxtaposing amorphous matrix with lingunite nano-crystals (some outlined by white contours). (b) FFT pattern containing characteristic 1´-1 and 2´-2 spots of lingunite and augite respectively. (c) IFFT pattern obtained using 2´-2 spots from (b) showing perfectly crystallized (100) planes. (d) IFFT pattern obtained using 1´-1 spots from (b (101) planes of lingunite containing numerous edge dislocations (e.g. see two dashed squares). An edge dislocation is enlarged in the inset.

augite. Moreover, the ion beam interacted first with the augite and thereafter with the labradorite. The augite crystal, therefore, experienced higher ion beam energy than labradorite crystal. The chance of amorphization of augite during FIB preparation is much more than that of labradorite. Since the augite is crystallized and the amorphous phase is present below augite, it can be concluded that the amorphous phase observed in HRTEM image (Fig. 4.7a) was not induced during FIB preparation and has a natural origin. The HRTEM image also shows that the boundary between augite and labradorite lamellae is not a two dimensional interface, but a contact zone, a 3 dimensional feature, marked by presence of

lingunite nano-crystals embedded in amorphous matrix. Therefore, the augite-labradorite lamellae interface is henceforth termed as the augite-labradorite lamellae contact zone.

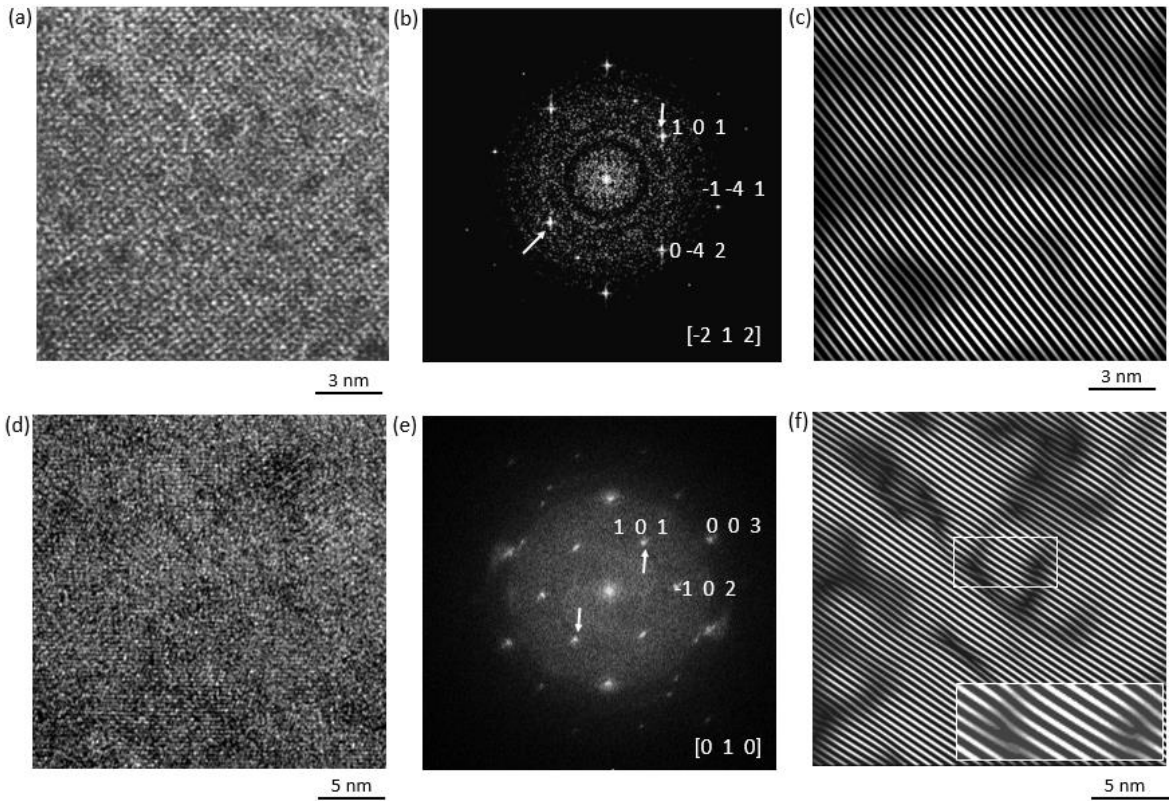

Figure 4.9. HRTEM analysis of 'TEM-3' and 'TEM-2' lamellae (refer to Fig. 4.4a for the positions of the TEM section). (a, b) HRTEM images from 'TEM-3' lamellae, i.e., the bulk labradorite and its FFT diffractogram showing sharp diffraction spots characteristic of labradorite. Arrows point towards (101) spots used for obtaining of IFFT diffractogram shown in Fig. 4.8c. (c) IFFT showing perfectly crystallized (101) planes. (c, d) HRTEM image from 'TEM-2' i.e., the labradorite lamella, and its FFT diffractogram showing diffused diffraction spots characteristic of labradorite. Arrows point towards (101) spots used for obtaining of IFFT diffractogram shown, Fig. 4.8f. (f) IFFT showing (101) planes and mosaic domains containing numerous edge dislocations, two of which are magnified in the inset.

Based on the FFT and the IFFT (Fig. 4.8b, 4.8d), the nano-crystals are classified as lingunite, with a = 9.262 Å and c = 2.720 Å. The lattice parameters were calculated from interplanar distances d_{110} = 6.55 Å, d_{-260} = 1.46 Å, d_{-170} = 1.31 Å and d_{101} = 2.61 Å (Fig. 4.7, 4.8d, Table 4.5). The lattice parameters compare well with those obtained by Liu [19] for pure $NaAlSi_3O_8$-hollandite (a = 9.30 Å and c = 2.73 Å) and by Gillet et al. [20] for natural $NaAlSi_3O_8$-hollandite (a = 9.263 Å and c = 2.706 Å). However, slightly lower parameters suggest that the crystal lattice is smaller than that of undeformed lingunite, and, therefore, compressed, as demonstrated by Liu [19]. A smaller crystal lattice indicates that the nano-crystals are deformed. Deformation of the lingunite crystal lattice is also revealed in IFFT diffractogram by the frequent edge dislocations (Fig. 4.8d).

These TEM results, i.e., randomly oriented deformed lingunite nano crystals, embedded in amorphous matrix confirm the Raman spectroscopy results and explain the broadening and shift of the 820 cm^{-1} band of lingunite (Fig. 4.5b). Moreover, in agreement with our Raman spectroscopy results, labradorite in the lamella, as compared to the bulk, is much more deformed (Fig 4.9).

4.5 Discussions

According to the published numerical models [13], the studied target rocks at Lockne impact structure suffered shock P-T in the order of ≤ 3 GPa and < 127°C (Fig. 4.1a). However, pertaining to the limitations of computing time, the smallest particles considered in such models are usually of the order of 10 cm [13]. Correspondingly, the estimations do not account for the possible shock-induced, submicroscopic, processes occurring at the interfaces between minerals with contrasting mechanical properties [177]. One such process predicted by theoretical studies, is the impedance contrast, and shearing at the interface, which may lead to local stress concentration [16,43] or to localized heating [16,48], when shock waves propagate across these interfaces.

For investigating shock effects on the interface, the sample 49 was selected as the augite and labradorite lamellae are best developed in it. The present results reveal occurrence of Lingunite nano-crystals at augite and labradorite lamellae interface in dolerite from the Lockne impact structure in Sweden. These results imply that, P-T spikes 10 to 20 times higher than expected peak shock P-T (< 3 GPa and < 127 °C [13]), may locally occur due to shock wave propagation in target rocks. Using the results from this study we suggest the following model for the formation of the high P-T phase, lingunite, at interface between weakly shocked minerals with contrasting mechanical properties.

It is well known that shock waves typically have two mutually resolved phases, namely compressive and decompressive [159,161], each of which causes distinct deformations. For example, a correlation between shock wave phases and different fracture geometries was shown by Polanskey and Ahrens [92], and Ahrens and Rubin [42].

The orientation of margin and trough of the labradorite lamella and the pre-impact boundary between the augite and labradorite grains can be estimated from the oriented micrograph

(Fig. 4.3a), SEM image (Fig. AF11), TEM section (Fig. 4.6a), and the orientational relationship among the shock wave, micrograph, radial microfractures (Fig. 4.10). These relationships may reveal critical information on the formation of the radial and the concentric microfractures and their relationship with the principal stress directions during the compressive and decompressive phases of the shock wave. In the equal area projection, figure 4.10, the shock direction and the orientation of micrograph, expected and observed concentric fractures is taken from figure 4.3b. Orientation of the trough of the labradorite lamella with respect to the micrograph is calculated using the distance from end of the labradorite lamellae, 8.9 µm, at which the TEM section is cut (Fig. AF11) and the thickness of the augite lamella, 4.8 µm, in the TEM section (Fig. 4.6a). The trough makes an angle of 33° from 'X' and dips about 51° from the plane of the micrograph (Fig. 4.10). The lineation of the TEM section on the micrograph makes a rake of 56° from 'X' (Fig. AF11). As the TEM section (cyan arc in fig. 4.10) is perpendicular to the micrograph, it was plotted by joining the rake (56° from X) and pole to the micrograph (24°/052°). The margins of the labradorite lamella or the labradorite-augite lamella interface make angles of 40° and 57° from the top of the TEM section (Fig. 4.6a). The lineations made by the labradorite lamella margins on the TEM section were therefore plotted at 40° and 57° from the two ends of the TEM section. The lamellae margins (purple arcs) were plotted by joining these two points with the trough of the labradorite lamellae. The pre-impact boundary between labradorite and augite will be represented by an arc formed by joining the trough of the lamellae to a line enveloping the end of the labradorite lamellae (Fig. AF11). The pre-impact boundary (black arc in figure 4.10) between labradorite and augite, thus plotted dips 56° due 195°.

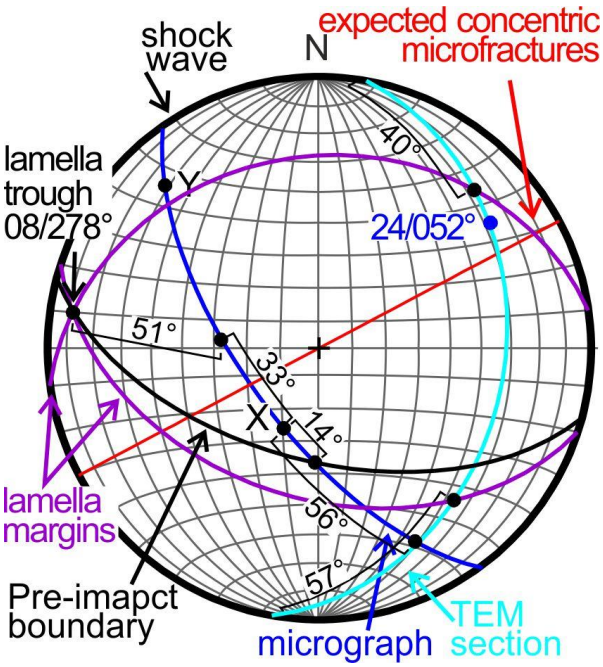

Fig 4.10 Stereonet demonstrating orientation of the micrograph (blue arc), expected concentric fractures (red arc) and TEM section (cyan arc). The trough and the margins of the labradorite lamella (purple arcs) are shown. The pre-impact augite-labradorite grain boundary is also shown.

We assume that the formation of alternating augite-labradorite lamellae is a three step process which corresponds to the phases of shock waves viz. initial compressive phase (step-1), followed by the decompressive phase (step-2) and a subsequent compressive phase (step-3). Each step may be represented in detail as following.

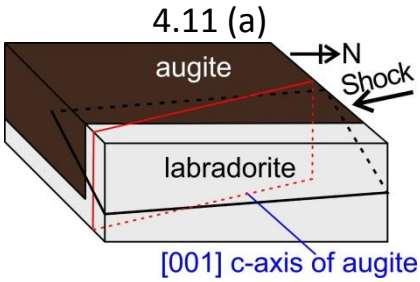

Figure 4.11 (a). Schematic representation of the augite-labradorite grain boundary before the shock-induced deformation. The direction of shock wave and [001] c-axis of augite is shown. Step-wise development the alternating augite and labradorite lamella is demonstrated through a vertical (red dashed line) section, that is parallel with the shock direction and with an oblique (white dashed lines) section that represents the view in the micrographs and SEM images (s. figure 4.3b for precise orientations).

4.5.1 Step 1. Compressive phase

Figure 4.1c and 4.3a show that the radial microfractures are parallel with the shock direction. This parallelism (Fig. 4.1c, Fig. 4.3a), when interpreted in light of experimental observations by Polanskey and Ahrens [92], suggests that, during the initial compressive phase of the shock wave, radial microfractures formed parallel with the direction of shock and with the σ_{1C}, which represents the maximum principal stress direction during compression phase (Fig. 4.11b).

Immediately preceding fracture, compressive forces may have provoked concentration of stresses at the labradorite-augite grain boundary. The grain boundary is a heterogeneity between the augite and labradorite, with large strength contrast [v = 0.293 and 0.243, respectively; 199]. Difference in strength may cause impedance contrast and result in shock localization [17,18]. The processes of shock localization and consequential stress and P-T concentrations are more significant for weak to moderate shock waves [16], as in present case. The highly localized concentration of P-T may, therefore, transform/compress labradorite into nano-crystals of lingunite (Fig. 4.7a) and, subsequently, into amorphous phase (Fig. 4.9a). Kubo et al. [200] suggest that the transformation of plagioclase into either a high P-T crystalline phase or an amorphous phase depends upon the kinetics. Sometimes, when the transformation into high P-T crystalline phase is sluggish, plagioclase, then transforms into an amorphous phase [200].

4.11 (b)

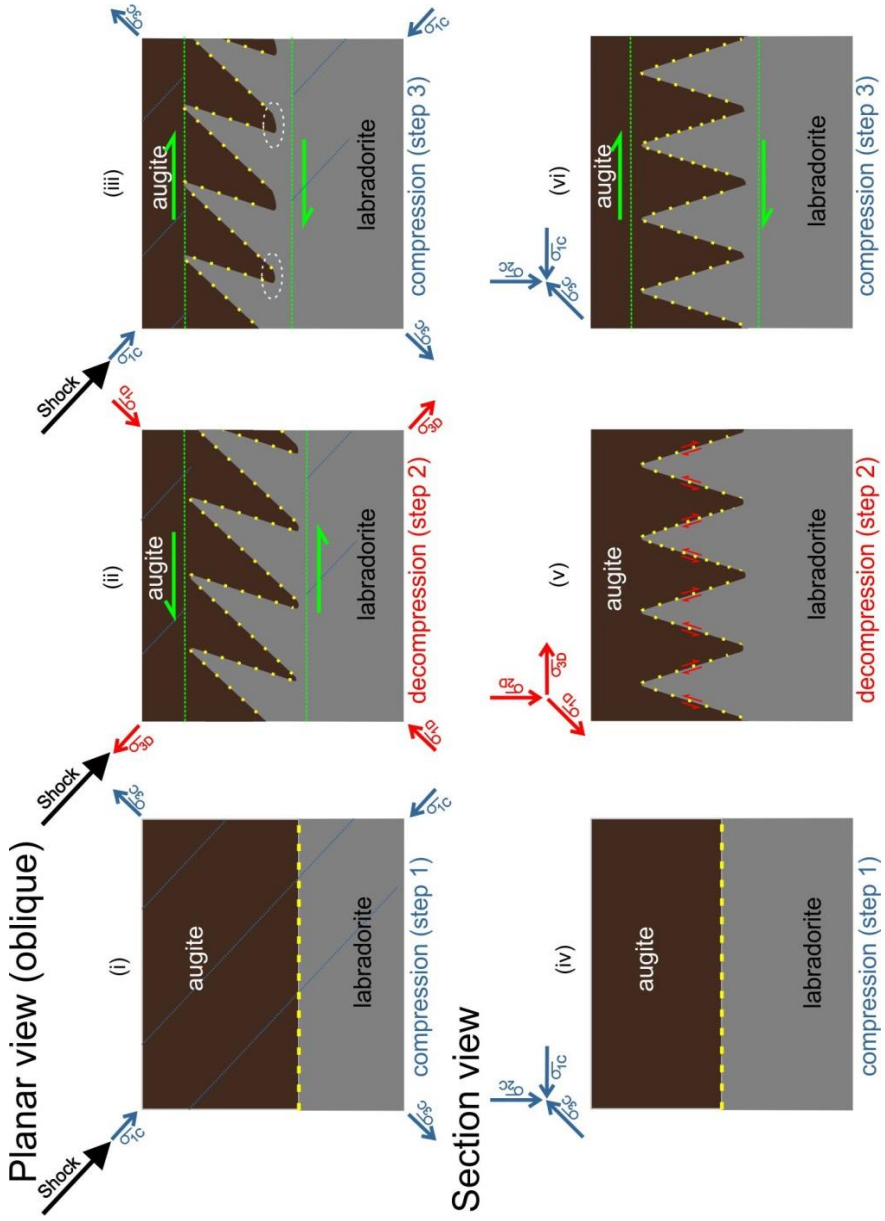

Figure 4.11 (b). Schematic demonstration of the 3-step structural evolution of alternating augite-labradorite lamellae and of lingunite nano-crystals embedded in amorphous matrix. The maximum and minimum stress directions during the compressive and the decompressive phase are represented by σ_{1C} and σ_{1D}; and σ_{1D} and σ_{3D}, respectively.

Step 1. Formation of lingunite nano-crystals (yellow dashes) and radial microfractures (blue lines) during the initial compressive phase of the shock wave. Step 2. In the decompressive phase direction of maximum and minimum principal stresses change, as shown by the arrows. Series of 'V' shaped concentric fractures, marked by relative upward movement of labradorite, develop (vertical section). Lingunite nano-crystals are pushed along the shear planes due to relative movement of augite and labradorite.

Step 3. In the compressive stage the maximum and minimum principal stress direction change The compressive stresses provoke shearing along the augite-labradorite grain boundary. The shear boundaries are shown by green dashed lines. Tips of the augite lamellae are sheared off (white dashed ellipse).

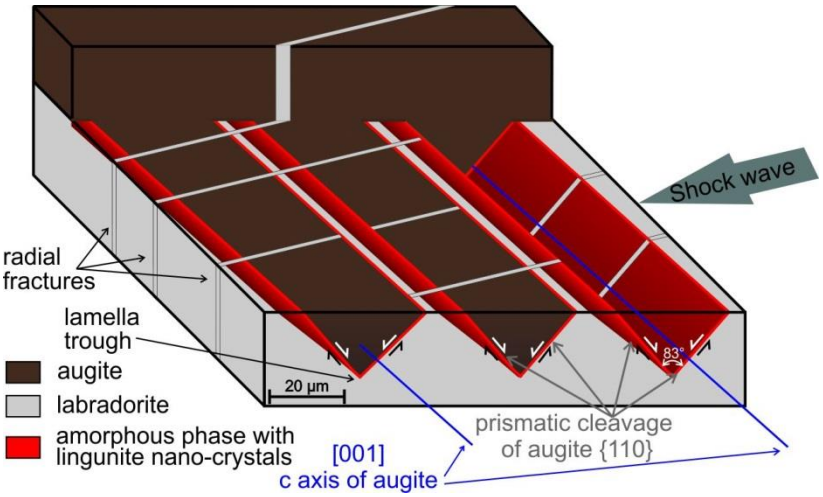

Figure 4.11 (c). Schematic diagram of relationship among the augite lamellae and the crystallographic properties revealed from the TEM results. From left, the first and second augite lamellae are as seen in the SEM images (Fig. 4.3). The right one, represents augite lamella visualized as hollow, i.e., without augite. The radial factures formed first, parallel with the shock direction. Thereafter, the {110} prismatic cleavage develops into concentric fractures. These fractures (and the lamellae margins) show an interplanar angle of about 83° (refer to Fig. 4.3b). The c-axis [001] of augite is parallel with the augite lamellae. Lingunite nano-crystals and the amorphous phase are present along the lamellae margins.

4.5.2 Step 2. Decompressive phase

During the decompressive phase of the shock wave the direction of maximum and minimum principal stresses σ_{1D} and σ_{3D}, change (Fig. 4.11b). The stresses cause fracturing and relative movement of augite and labradorite (section view in Fig. 4.11b) resulting in alternating lamellae (plan view in Fig. 4.11b). The regular shape of the fractures and consistent angle of 83° between adjacent fracture planes indicates some crystallographic control of either or both augite and labradorite on the geometry of the fractures. However, since augite is mechanically stronger than labradorite, augite may fracture while labradorite may behave in a ductile manner. This interpretation is based on the results obtained by Raman spectroscopy showing gradual broadening and shift of active bands closer to the labradorite lamella boundary (Fig. 4.5c) and HRTEM results revealing numerous dislocations in labradorite from the lamellae as compared to the bulk (Fig 4.9c, f). As the augite and labradorite move relative to each other (Fig. 4.11b), the lingunite nano-crystals which were initially present at the grain boundary (Fig. 4.11b), are pushed along the shear planes (Fig. 4.11b). Moreover, the pressure release may lead to expansion and transformation of some lingunite into amorphous phase.

Control of crystallographic orientation on the geometry of the concentric fractures

In 3 dimension, considering the cross-sectional view in figures 4.6a and 4.6b, the lamellae margin demonstrate a 'V'-shaped geometry and have an interplanar angle of about 83° (Fig.

4.6b). This angle is consistent with the angle between {110} prismatic cleavage planes of augite. The SAED pattern (Fig. 4.7d, e) of augite in the TEM section (Fig. 4.7a) reveals that the TEM section is along the ($\bar{1}$01) plane of augite. The c-axis [001] of augite is, therefore, perpendicular to the plane of the TEM section and parallel with the augite-labradorite lamellae (Fig 4.7, 4.11c). It is, therefore, possible that during the decompressive phase concentric fractures in augite developed along the {110} prismatic cleavage planes of augite. This hypothesis is supported by a comparison of geometry of the augite-labradorite lamellae interface (Fig. 4.12a) with a simplified augite crystal model from Mineral data.org [201] (Fig. 4.12b). If we consider the interface to be (100) plane, also representing the {110} prismatic cleavage, and the augite face visible in the TEM image to be ($\bar{1}$01) plane, the bulge in the interface is strikingly similar to geometry of an augite half-crystal (Fig. 4.12). The hypothesis is further supported by the fact that, the interfacial angles in the TEM image (α and β; Fig. 4.12a) and the crystal model (α' and β'; Fig. 4.12b), i.e. between (100) and (1$\bar{1}$0) (α=128°; α'=130°) and between (100) and (110) (β=137°; β'=138°) are very close.

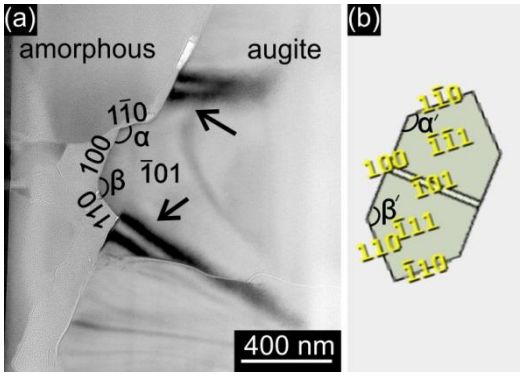

Figure 4.12. Visual comparison of a bulge in the augite crystal with a simplified augite crystal model from Mineral data.org [201]. The interfacial angle between (100) and (1$\bar{1}$0) plane in TEM image and the model are α and α', respectively. Similarly interfacial angle between (100) and (110) are β and β'. (a) TEM image of the lamellae interface showing orientation contrast in augite (arrow). (b) Augite crystal with Miller indices of visible faces.

Strong crystallographic control on the impact generated microfractures is, therefore, evident. Crystallographic orientation of augite is vital in development of fractures. The crystallographic orientation of augite with respect to the direction of shock may also control the geometry of the fractures. Variation in the orientation of augite crystal with respect to the shock direction may, result in various dimensions and geometries of the lamella, as observed in figure 4.2. For example, the concentric fractures (lamellae) will be most prominent if the, if the augite cleavage planes are perpendicular to the shock direction. The concentric fractures (lamellae) may be less prominent if the augite cleavage planes are oblique to the shock direction.

4.5.3 Step 3. Compressive phase

The decompressive phase of the shock wave (step 2) is followed by the compressive phase (step 3). The principal stress directions change such that they are now similar to the directions in step 1. Reversal of stress directions leads to apparent dextral shearing along the augite-labradorite grain boundary (s. step 3 in Fig. 4.11b).

The labradorite lamellae are shielded by surrounding, mechanically stronger augite. The tips of the labradorite lamellae, therefore, do not show significant effects of shearing. However, the augite lamellae are surrounded by mechanically weaker labradorite. Due to shearing, stresses concentrate at the tip of the augite lamellae. The tips of the augite lamellae are thus sheared-off and not preserved (s. step 3 in Fig. 4.11b, Fig. 4.4a).

4.5.4 Mode of concentric fracturing

In fracturing of mode I type or pure extension (opening), tensile stresses drive fracture perpendicular to the fracture plane [202] without any shear component. In contrast mode II and mode III have a shear component along the fracture plane. In mode II the direction of shear is along the direction of fracture propagation, unlike mode III, where the direction of shear is perpendicular to the direction of fracture propagation [202,203]. Previously published reports on impact induced fractures suggest that concentric fractures form during the decompressive phase of the shock wave due to instantaneous pressure release, perpendicular to the shock wave propagation direction (section 1.5.1) and to the direction of maximum tensile stresses (Fig. 4.13) [42,101]. The results from these studies [42,92,101] imply that the concentric fractures formed due to shock wave are mode I fractures without significant shear component.

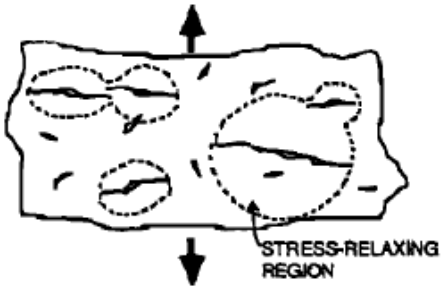

Fig. 4.13 Schematic diagram of tensile failure of rock under dynamic loading [after 101].

In contrast the present microscopic observations indicate that the concentric fractures have shear component (Fig. 3.6b). On investigating the orientational relationships between the concentric microfracture and the shock wave propagation direction, it is clear that although the concentric microfractures strike perpendicular to the shock

direction, the fractures planes are not perpendicular either to the shock wave propagation direction or to the direction of maximum tensile stress (σ_{3D}, step-2 in section view of figure 4.11b). Shearing along the propagation direction of the concentric fractures (step-2 in figure 4.11b) indicates that the concentric fractures may sometimes be mixed mode I and II [c.f. fig. 2.16 in 179]. Whether the concentric fractures are mode I or II may depend upon the orientation of the mechanical flaws. If the mechanical flaws are oriented oblique to the shock wave propagation direction shear component may develop [section 2.1.2.3 in 179,204]. The sudden increment in the tensile stresses would not allow the concentric fractures, which develop along obliquely oriented mechanical flaws, to rotate and reorient favourably with respect to the direction of maximum tensile stress, as observed when stresses are increased gradually, [fig. 2.5 in 179,205]. The shock wave induced concentric microfractures, therefore, may develop along mechanical flaws, even if the flaws are obliquely oriented to the direction of maximum tensile stress direction. This conclusions is in accordance with Rubin and Ahrens [101] who suggest that, in case of very rapidly increasing tensile stresses, fractures propagate from flaws that are 'poorly-oriented' with respect to the direction of maximum tensile stress (Fig. 4.13).

The concentric fractures formed along the cleavage planes instead of the most favourable direction, which is perpendicular to shock wave propagation direction, because the fracture surface energy along the cleavage planes is higher [section 1.5.2 in 179,206]. However since the cleavage planes are not favourably oriented, the concentric fractures have a shear component (discussed above), are formed in pairs (Fig. 4.11c), and intersect to form the labradorite lamella trough.

5. Conclusions

5.1 Rock magnetics, microfractures and shock pressures at the Lonar crater

For fulfilling the present objectives of estimating effects of shock effects through rock magnetics and microfractures a relatively young and pristine crater, the Lonar impact structure, was chosen. To test a potential effect of shock on the target rocks AMS, NRM, the Curie temperature, Verwey transition temperature and coercivity were used. The comparisons between magnetic- and magmatic-fabrics revealed that the magnetic fabrics are related to the lava flow history and were not reoriented due to the impact.

Two separate components of NRM were identified. The HC component shows NRM direction similar to that in the unshocked Deccan basalts. No evidence that may suggest the overprinting of HC component by the impact was found. The LC component, similar to that of the present day magnetic field, is attributed to either weathering or viscous remanent magnetization.

Experimental studies on Lonar basalt suggest that any change in the maximum susceptibility axis would require shock pressure as low as 0.5 GPa [6,7]. As shown in our study, there is a lack of change in the maximum susceptibility axis in the target basalts (Fig. 2.6a and 2.7b). Moreover, shock induced microfractures in feldspars, as observed in present study, are commonly observed at pressure over 0.2 GPa [8,9]. The peak shock pressure in Lonar crater rim was, therefore, in the range of 0.2 to 0.5 GPa. This is supported by the results of numerical modelling by Louzada et al. [12] who found <1 GPa peak shock pressure at the Lonar crater rim.

5.2 Magnetic fabrics, microfractures and shock pressures at the Lockne crater

The second part of present study investigates the magnetic fabrics and microfractures in crystalline target rocks of the Lockne impact structure in Sweden. Titanomagnetite is identified as the carrier of magnetic fabrics. Known analogues of shock effects on magnetic fabrics in rocks, with similar magnetic mineralogy, are employed to predict the shock pressure. Similarly, a comparison of the microfractures with published analogues reveals information on shock pressure. Finally the overprinting relationship of the microfractures gives important clues of, the Lockne impact generated, shock wave geometry.

The susceptibility axes and the magnetic anisotropies, show no change in any of the studied rocks, irrespective of their distance from the crater. On the other hand, the microfractures, in rocks between 3.5 km (the inner crater rim) and 6.5 km from the centre of the crater show impact generated microfractures. The results, when interpreted in light of experimental studies, suggest shock pressure in the range of 0.5 to 0.2 GPa in rocks up to about 6.5 km from the centre of the crater, and in the order of < 0.2GPa in the rocks farther away [6–10,162].

The overprinting relationship of the impact generated microfractures demonstrates that the radial and concentric microfractures formed during the initial compressive and following decompressive phase respectively.

5.3 Shock induced fractures, shear zones and shock localization

In the present work, numerous simultaneous and interfering deformation mechanisms, occurring at different spatial scales in dolerite of the Lockne impact structure were taken into account and investigated. Through unambiguous petrological evidences, a model of microfracturing during the compressive- and decompressive- phases of the shock waves is proposed. Strong control of augite crystallography over the geometry of the fractures is established.

Kenkmann et al [18] suggest shearing at grain boundaries may only be provoked if the shock waves are parallel with the boundary. However, we observe formation of concentric fractures due to shock induced shearing, even when grain boundary was not parallel with the shock propagation direction. This suggests that parallelism of shock and grain boundaries is not a necessary condition for shock induced shearing.

5.3.1 Shock localization

Classical methods of shock pressure estimations, such as numerical modelling and shock indicators, as well as those presently employed reveal peak pressures, which are averaged over an area of few square cm. However, contrary to the common understanding, these pressures are hardly representative of micrometre-scale phenomena. The third part of the work demonstrates that local fluctuations in stresses may lead to high concentration of P-T.

This intense concentration may, under favourable conditions, form polymorphs that have not been observed before in the naturally shocked terrestrial rocks.

Polymorphs of plagioclase such as lingunite in amorphous melts are common in meteorites, due to high shock P-T. The Tenham meteorite, is the closest example where nano crystals of hollandite structured plagioclase are embedded in an amorphous matrix with plagioclase composition [177].

Here, for the first time natural lingunite is discovered in terrestrial target rocks. Using the correlation shown by Liu [192] we establish that even in Lockne target rocks, that have suffered weak overall shock intensities, i.e., peak P-T in the order of < 3 GPa and < 127°C, physical interactions and localization of shock energy along grain boundaries may lead to P-T spikes that are 10 to 20 times higher than peak pressures as estimated by Lindström [13].

The identification of lingunite at augite-labradorite grain interfaces of this study confirms theoretical works predicting P-T spikes at heterogeneous interfaces. For example a recent calculation indicated pressure spike of 30 GPa in heterogeneous material at grain interfaces, where peak pressures were 3 GPa [177]. Therefore, the study of shock interactions at mineral interfaces may be used for constraining the temporal micro-scale variations in pressure. This study emphasizes the need of more high resolution investigations at nm scale of terrestrial impact target rocks for identification of high pressure indicators and high pressure mineral phases, which may be much more common than previously expected.

References

1. Ivanov, B. A. 2001. in *Chronology and evolution of Mars*. 87–104.
2. Stöffler, D. et al. 2006. Cratering history and lunar chronology. *Reviews in Mineralogy and Geochemistry*. **60(1)** 519–596.
3. Spray, J. and Hines, J. 2014. Earth impact database. *Planetary and Space Science Centre, University of New Brunswick, Canada*.
4. Herrick, R. R. and Pierazzo, E. 2003. Improving knowledge of impact cratering: Bringing together "Modelers" and "Observationalists." *Eos, Transactions American Geophysical Union*. **84(31)** 291. doi: 10.1029/2003EO310006
5. Maloof, A. C. et al. 2009. Geology of Lonar Crater, India. *Geological Society of America Bulletin*. **122(1-2)** 109–126. doi: 10.1130/B26474.1
6. Nishioka, I. and Funaki, M. 2008. Irreversible changes in anisotropy of magnetic susceptibility. Study of basalts from lunar crater and experimentally impacted basaltic andesite. in *Meteoritics & Planetary Science*. 5207.
7. Nishioka, I., Funaki, M. and Sekine, T. 2007. Shock-induced anisotropy of magnetic susceptibility: Impact experiment on basaltic andesite. *Earth, Planets and Space*. **59(2002)** 45–48.
8. Lambert, P. 1979. Fractures induced by shock in quartz and feldspar. *Mineralogical magazine*. **43(328)** 527–533.
9. Hörz, F. 1969. Structural and mineralogical evaluation of an experimentally produced impact crater in granite. *Contributions to Mineralogy and Petrology*. **21(4)** 365–377. doi: 10.1007/BF02672808
10. Gattacceca, J. et al. 2007. The effects of explosive-driven shocks on the natural remanent magnetization and the magnetic properties of rocks. *Physics of the Earth and Planetary Interiors*. **162(1-2)** 85–98. doi: 10.1016/j.pepi.2007.03.006
11. Mang, C., Kontny, A., Fritz, J. and Schneider, R. 2013. Shock experiments up to 30 GPa and their consequences on microstructures and magnetic properties in pyrrhotite. *Geochemistry, Geophysics, Geosystems*. **14(1)** 64–85. doi: 10.1029/2012GC004242
12. Louzada, K. L. et al. 2008. Paleomagnetism of Lonar impact crater, India. *Earth and Planetary Science Letters*. **275(3-4)** 308–319. doi: 10.1016/j.epsl.2008.08.025
13. Lindström, M., Shuvalov, V. and Ivanov, B. 2005. Lockne crater as a result of marine-target oblique impact. *Planetary and Space Science*. **53(8)** 803–815. doi: 10.1016/j.pss.2005.02.005
14. Shuvalov, V. V. 1999. Multi-dimensional hydrodynamic code SOVA for interfacial flows: Application to the thermal layer effect. *Shock Waves*. **9(6)** 381–390. doi: 10.1007/s001930050168
15. Shuvalov, V., Ormö, J. and Lindström, M. 2005. in *Impact tectonics*.
16. Grady, D. E. 1980. Shock deformation of brittle solids. *Journal of Geophysical Research*. **85(B2)** 913. doi: 10.1029/JB085iB02p00913
17. Gibson, H. M. and Spray, J. G. 1998. Shock-induced melting and vaporization of shatter cone surfaces: Evidence from the Sudbury impact structure. *Meteoritics & Planetary Science*. **33(2)** 329–336. doi: 10.1111/j.1945-5100.1998.tb01637.x
18. Kenkmann, T., Hornemann, U. and Stöffler, D. 2000. Experimental generation of shock-induced pseudotachylites along lithological interfaces. *Meteoritics & Planetary Science*. **35(6)** 1275–1290. doi: 10.1111/j.1945-5100.2000.tb01516.x
19. Liu, L. 1978. High-pressure phase transformations of albite, jadeite and nepheline. *Earth and Planetary Science Letters*. **37** 438–444.
20. Gillet, P. 2000. Natural NaAlSi3O8-Hollandite in the Shocked Sixiangkou Meteorite. *Science*. **287(5458)** 1633–1636. doi: 10.1126/science.287.5458.1633
21. French, B. M. 1988. *Traces of Catastrophe: A Handbook of Shock-Metamorphic Effects in Terrestrial Meteorite Impact Structure*. *Technical Report, LPI-Contrib-954*. **1** 120.

22. Chauhan, P. et al. 2012. Compositional and morphological analysis of high resolution remote sensing data over central peak of Tycho crater on the Moon: implications for understanding lunar interior. *Current Science (00113891)*. **102(7)**
23. Taylor, S. R. 1982. Planetary science: A lunar perspective.
24. Taylor, S. R. 2001. *Solar System evolution: a new perspective: An inquiry into the chemical composition, origin, and evolution of the Solar System*.
25. French, B. M. and Koeberl, C. 2010. The convincing identification of terrestrial meteorite impact structures: What works, what doesn't, and why. *Earth-Science Reviews*. **98(1-2)** 123–170. doi: 10.1016/j.earscirev.2009.10.009
26. Grieve, R. A. F. 1991. Terrestrial impact: The record in the rocks. *Meteoritics*. **26(3)** 175–194.
27. French, B. M. 1990. 25 years of the impact-volcanic controversy: Is there anything new under the Sun or inside the Earth? *Eos, Transactions American Geophysical Union*. **71(17)** 411–414.
28. French, B. M. 1968. Shock metamorphism as a geological process. *Shock metamorphism of natural materials*. 1–17.
29. Bhandari, N. and Srivastava, N. 2014. Active moon: evidences from Chandrayaan-1 and the proposed Indian missions. *Geoscience Letters*. **1(1)** 1–12.
30. Melosh, H. J. 1989. *Impact cratering: A geologic process*. **1** 253.
31. Reimold, W. U. and Koeberl, C. 2014. Impact structures in Africa: A review. *Journal of African Earth Sciences*. **93** 57–175. doi: 10.1016/j.jafrearsci.2014.01.008
32. Srivastava, N. 2008. Titanium estimates of the central peaks of lunar craters: Implications for sub-surface lithology of moon. *Advances in Space Research*. **42(2)** 281–284.
33. Grieve, R. A. F. and Masaitis, V. L. 1994. The economic potential of terrestrial impact craters. *International Geology Review*. **36(2)** 105–151.
34. Johnson, K. S. and Campbell, J. A. 1997. *Ames structure in northwest Oklahoma and similar features: origin and petroleum production (1995 symposium): proceedings of a symposium held March 28-29, 1995, in Norman, Oklahoma*. **(100)**
35. Guy-Bray, J. V. 1972. *New developments in Sudbury geology*. **(10)**
36. Giblin, P. E. et al. 1984. *The geology and ore deposits of the Sudbury structure*.
37. Alvarez, L. W., Alvarez, W., Asaro, F. and Michel, H. V. 1980. Extraterrestrial cause for the cretaceous-tertiary extinction. *Science (New York, N.Y.)*. **208(4448)** 1095–108. doi: 10.1126/science.208.4448.1095
38. Peninsula, Y. et al. 1991. Geology Chicxulub Crater : A possible Cretaceous / Tertiary boundary impact crater on the Chicxulub Crater : A possible Cretaceous / Tertiary boundary impact crater on the Yucatán Peninsula , Mexico. doi: 10.1130/00917613
39. Osinski, G. R. and Pierazzo, E. 2012. *Impact cratering: processes and products*. 316.
40. O'Keefe, J. D. and Ahrens, T. J. 1989. Impact production of C02 by the Cretaceous/Tertiary extinction bolide and the resultant heating of the Earth. *Nature*. **338(6212)** 247–249. doi: 10.1038/338247a0
41. Pope, K. O., Baines, K. H., Ocampo, A. C. and Ivanov, B. A. 1997. Energy, volatile production, and climatic effects of the Chicxulub Cretaceous/Tertiary impact. *Journal of Geophysical Research: Planets (1991–2012)*. **102(E9)** 21645–21664.
42. Ahrens, T. J. and Rubin, A. M. 1993. Impact-induced tensional failure in rock. **98(92)** 1185–1203. doi: 10.1029/92JE02679
43. Rinehart, J. S. 1968. *Intense destructive stresses resulting from stress wave interactions*. *Shock Metamorphism of Natural Materials. Mono Book Corp., Baltimore, Maryland*. 31–42.
44. Stöffler, D., Bischoff, A., Buchwald, V. and Rubin, A. E. 1988. Shock effects in meteorites. *Meteorites and the early solar system*. **1** 165–202.
45. Stöffler, D., Keil, K. and Edward R.D, S. 1991. Shock metamorphism of ordinary chondrites. *Geochimica et Cosmochimica Acta*. **55(12)** 3845–3867. doi: 10.1016/0016-7037(91)90078-J
46. Bischoff, A. and Stöffler, D. 1992. Shock metamorphism as a fundamental process in the evolution of planetary bodies: information from meteorites. *European journal of mineralogy*. **4(4)** 707–755.

47. Chen, M., McCauley, J. W. and Hemker, K. J. 2003. Shock-induced localized amorphization in boron carbide. *Science (New York, N.Y.)*. **299(5612)** 1563–6. doi: 10.1126/science.1080819
48. Coffey, C. S. 1991. The localization of energy and plastic deformation in crystalline solids during shock or impact. *Journal of Applied Physics*. **70(8)** 4248. doi: 10.1063/1.349151
49. O'Keefe, J. D. and Ahrens, T. J. 1993. Planetary cratering mechanics. *Journal of Geophysical Research: Planets (1991–2012)*. **98(E9)** 17011–17028.
50. Gault, D. E., Oberbeck, V. R. and Quaide, W. L. 1968. *Impact cratering mechanics and structures*.
51. Reimold, W. and Koeberl, C. 2008. Catastrophes, extinctions and evolution: 50 years of impact cratering studies. *Golden Jubilee Memoir of the Geological society of India*. **(66)** 69–110.
52. Maxwell, D. E. 1977. Simple Z model for cratering, ejection, and the overturned flap. in *Impact and Explosion Cratering: Planetary and Terrestrial Implications*. **1** 1003–1008.
53. Grieve, R. R. A. F., Dence, M. R. and Robertson, P. B. 1977. Cratering processes-As interpreted from the occurrence of impact melts. *Impact and explosion cratering: Planetary and terrestrial implications; Proceedings of the Symposium on Planetary Cratering Mechanics, Flagstaff, Ariz., September 13-17, 1976. (A78-44030 19-91)*. **1** 791–814.
54. Grieve, R. a. F. and Cintala, M. J. M. 1982. A method for estimating the initial impact conditions of terrestrial cratering events, exemplified by its application to Brent crater, Ontario. *Lunar and Planetary Science Conference*. **(934)** 1607–1621.
55. Fredriksson, K., Noonan, A. and Nelen, J. 1973. Meteoritic, lunar and Lonar impact chondrules. *The Moon*. **7(April)** 475–482.
56. Sengupta, D., Bhandari, N. and Watanabe, S. 1997. Formation age of Lonar meteor crater, India. *Revista de Fisica Aplicada e Instrumentacao*. **12(1)** 1–7.
57. Misra, S. et al. 2010. Structural and anisotropy of magnetic susceptibility (AMS) evidence for oblique impact on terrestrial basalt flows: Lonar crater, India. *Bulletin of the Geological Society of America*. **122** 563–574. doi: 10.1130/B26550.1
58. Jourdan, F., Moynier, F., Koeberl, C. and Eroglu, S. 2011. 40Ar/39Ar age of the Lonar crater and consequence for the geochronology of planetary impacts. *Geology*. **39(7)** 671–674.
59. Fredriksson, K., Dube, A., Milton, D. J. and Balasundaram, M. S. 1973. Lonar lake, India: an impact crater in basalt. *Science*. **180(4088)** 862–864. doi: 10.1126/science.180.4088.862
60. Fudali, R. F., Milton, D. J., Fredriksson, K. and Dube, A. 1980. Morphology of Lonar Crater, India: Comparisons and implications. *The Moon and the Planets*. **23(4)** 493–515. doi: 10.1007/BF00897591
61. Grieve, R. a. F. et al. 1989. Test of a geometric model for the modification stage of simple impact crater development. *Meteoritics*. **88(2)** 83–88. doi: 10.1111/j.1945-5100.1989.tb00948.x
62. Kumar, P. S. 2005. Structural effects of meteorite impact on basalt: Evidence from Lonar crater, India. *Journal of Geophysical Research*. **110(B12)** B12402. doi: 10.1029/2005JB003662
63. Gilbert, G. K. 1896. The origin of hypotheses, illustrated by the discussion of a topographic problem. *Science*. **3(53)** 1–13. doi: 10.1126/science.3.53.1
64. La Touche, T. H. D. and Christie, W. A. K. 1912. The geology of the Lonar Lake. *Records of the Geological Survey of India*. **41** 266–275.
65. Lafond, E. C. and Deitz, R. S. 1964. Lonar Crater, India, a meteorite crater? *Meteoritics*. **2(2)** 111–116.
66. Subrahmanyam, B. 1985. Lonar crater, India: a crypto-volcanic origin. *Journal of the Geological Society of India*. **26(5)** 326–335.
67. Murali, A. 1987. Tektite-like bodies at Lonar Crater, India: Implications for the origin of tektites. *Journal of Geophysical Research*. **92(B4)** E729–E735.
68. Nayak, V. 1972. Glassy objects (impactite glasses?) a possible new evidence for meteoritic origin of the Lonar Crater, Maharashtra State, India. *Earth and Planetary Science Letters*. **14(1)** 1–6. doi: 10.1016/0012-821X(72)90070-2
69. Nayak, V. K. 1993. Maskelynite from the Indian impact crater at Lonar. *Journal of the Geological Society of India*. **41(4)** 307–312.

70. Hagerty, J. and Newsom, H. 2003. Hydrothermal alteration at the Lonar Lake impact structure, India: Implications for impact cratering on Mars. *Meteoritics & Planetary Science*. **381(3)** 365–381.
71. Kieffer, S. W. et al. 1976. Shocked basalt from Lonar impact crater, India, and experimental analogues. in *Lunar and Planetary Science Conference Proceedings*. **7** 1391–1412.
72. Ghosh, S. 2003. Is Lonar astrobleme an example of cometary impact. *Indian Minerals*. **57(3)** 105–114.
73. Sturkell, E. F. F. 1998. The marine Lockne impact structure, Jämtland, Sweden: a review. *Geologische Rundschau*. **87(3)** 253–267. doi: 10.1007/s005310050208
74. Lindström, M., Sturkell, E. F. F., Törnberg, R. and Ormouml;, J. 2009. The marine impact crater at Lockne, central Sweden. *GFF*. **118(4)** 193–206. doi: 10.1080/11035899609546255
75. Sturkell, E. F. F. and Ormö, J. 1998. Magnetometry of the marine, Ordovician Lockne impact structure, Jämtland, Sweden. *Journal of Applied Geophysics*. **38(3)** 195–207. doi: 10.1016/S0926-9851(97)00031-1
76. Kousa, J., Lukkarinen, H. and Lundqvist, T. 2000. Proterozoic crystalline rocks. *Description to the Bedrock Map of Central Fennoscandia (Mid-Norden), Geol. Surv. Finland, Spec. Pap*. **28** 25–75.
77. Claesson, S. and Lundqvist, T. 1995. Origins and ages of Proterozoic granitoids in the Bothnian Basin, central Sweden; isotopic and geochemical constraints. *Lithos*. **36(2)** 115–140. doi: 10.1016/0024-4937(95)00010-D
78. Högdahl, K. and Sjöström, H. 2001. Evidence for 1.82 Ga transpressive shearing in a 1.85 Ga granitoid in central Sweden: implications for the regional evolution. *Precambrian Research*. **105(1)** 37–56. doi: 10.1016/S0301-9268(00)00102-9
79. Lindström, M. and Sturkell, E. F. F. 1992. Geology of the Early Palaeozoic Lockne impact structure, Central Sweden. *Tectonophysics*. **216(1-2)** 169–185. doi: 10.1016/0040-1951(92)90164-2
80. Patchett, P. J., Bylund, G. and Upton, B. G. J. 1978. Palaeomagnetism and the Grenville orogeny: New Rb-Sr ages from dolerites in Canada and Greenland. *Earth and Planetary Science Letters*. **40(3)** 349–364. doi: 10.1016/0012-821X(78)90159-0
81. Ernst, R. E. and Buchan, K. L. 2001. Large mafic magmatic events through time and links to mantle-plume heads. *SPECIAL PAPERS-GEOLOGICAL SOCIETY OF AMERICA*. 483–576.
82. Söderlund, U. et al. 2005. U-Pb baddeleyite ages and Hf, Nd isotope chemistry constraining repeated mafic magmatism in the Fennoscandian Shield from 1.6 to 0.9 Ga. *Contributions to Mineralogy and Petrology*. **150** 174–194. doi: 10.1007/s00410-005-0011-1
83. Bergman, S., Sjöström, H. and Högdahl, K. 2006. Transpressive shear related to arc magmatism: The Paleoproterozoic Storsjön-Edsbyn Deformation Zone, central Sweden. *Tectonics*. **25(1)** n/a–n/a. doi: 10.1029/2005TC001815
84. Gorbatschev, R., Solyom, Z. and Johansson, I. 1979. The Central Scandinavian Dolerite Group in Jämtland, central Sweden. *Geologiska Foereningan i Stockholm. Foerhandlingar*. **101(3)** 177–190. doi: 10.1080/11035897909448572
85. Sturkell, E. F. F., Broman, C., Forsberg, P. and Torssander, P. 1998. Impact-related hydrothermal activity in the Lockne impact structure, Jamtland, Sweden. *European Journal of Mineralogy*. **10(3)** 589–606.
86. Kenkmann, T. et al. 2007. Coupled effects of impact and orogeny: Is the marine Lockne crater, Sweden, pristine? *Meteoritics & Planetary Science*. **42(11)** 1995–2012. doi: 10.1111/j.1945-5100.2007.tb00556.x
87. Lindqvist, J. E. and Andréasson, P. G. 1987. Illite crystallinity and prograde metamorphism in thrust zones of the Scandinavian Caledonides. *Science Géologique Bulletin*. **40** 217–230.
88. Gee, D. G. and Kumpulainen, R. 1980. *An excursion through the Caledonian mountain chain in central Sweden from Östersund to Storlien*.
89. Lindström, M., Ormö, J., Sturkell, E. and Dalwigk, I. von. 2005. in *Impact tectonics*. doi: 10.1007/3-540-27548-7_14

90. Arif, M., Basavaiah, N., Misra, S. and Deenadayalan, K. 2012. Variations in magnetic properties of target basalts with the direction of asteroid impact: Example from Lonar crater, India. *Meteoritics and Planetary Science*. **47(8)** 1305–1323. doi: 10.1111/j.1945-5100.2012.01395.x
91. Kumar, P. S. and Kring, D. a. 2008. Impact fracturing and structural modification of sedimentary rocks at Meteor Crater, Arizona. *Journal of Geophysical Research*. **113(E9)** E09009. doi: 10.1029/2008JE003115
92. Polanskey, C. and Ahrens, T. 1990. Impact spallation experiments: Fracture patterns and spall velocities. *Icarus*. **155(87)** 140–155.
93. Arakawa, M., Shirai, K. and Kato, M. 2000. Shock wave and fracture propagation in water ice by high velocity impact. *Geophysical Research Letters*. **27(3)** 305. doi: 10.1029/1999GL010841
94. Field, J. E. 1971. Brittle fracture: its study and application. *Contemporary Physics*. **12(1)** 1–31.
95. Fourney, W. L., Barker, D. B. and Holloway, D. C. 1984. Mechanisms of fragmentation in brittle materials. in *Shock waves in condensed matter--1983: proceedings of the American Physical Society topical conference held in Santa Fe, New Mexico, July 18-21, 1983*. **82** 153.
96. Selberg, H. L. 1952. Transient compression waves from spherical and cylindrical cavities. *Arkiv for Fysik*. **5(1-2)** 97–108.
97. Shibuya, T. and Nakahara, I. 1968. The Semi-Infinite Body Subjected to a Concentrated Impact Load on the Surface. *Bulletin of JSME*. **11(48)** 983–992. doi: 10.1299/jsme1958.11.983
98. Swain, M. V and Hagan, J. T. 1980. Rayleigh wave interaction with, and the extension of, microcracks. *Journal of Materials Science*. **15(2)** 387–404.
99. Melosh, H. 1984. Impact ejection, spallation, and the origin of meteorites. *Icarus*. **59(2)** 234–260. doi: 10.1016/0019-1035(84)90026-5
100. Sammis, C. G. and Ashby, M. F. 1986. The failure of brittle porous solids under compressive stress states. *Acta Metallurgica*. **34(3)** 511–526.
101. Rubin, A. M. and Ahrens, T. J. 1991. Dynamic tensile-failure-induced velocity deficits in rock. *Geophysical Research Letters*. **18(2)** 219–222. doi: 10.1029/91GL00214
102. Graham, G. a. et al. 2004. Mineralogy and microanalysis in the determination of cause of impact damage to spacecraft surfaces. *Geological Society, London, Special Publications*. **232(1)** 137–146. doi: 10.1144/GSL.SP.2004.232.01.13
103. Nakazawa, S. et al. 1997. Hugoniot equation of state of basalt. *Planetary and Space Science*. **45(11)** 1489–1492. doi: 10.1016/S0032-0633(97)00070-6
104. Vandamme, D., Courtillot, V., Besse, J. and Montigny, R. 1991. Paleomagnetism and age determinations of the Deccan Traps (India): Results of a Nagpur-Bombay Traverse and review of earlier work. *Reviews of Geophysics*. **29(2)** 159. doi: 10.1029/91RG00218
105. Ai, H. a. and Ahrens, T. J. 2006. Simulation of dynamic response of granite: A numerical approach of shock-induced damage beneath impact craters. *International Journal of Impact Engineering*. **33(1-12)** 1–10. doi: 10.1016/j.ijimpeng.2006.09.046
106. Ormö, J. 2002. Numerical modeling for target water depth estimation of marine-target impact craters. *Journal of Geophysical Research*. **107** 1–9. doi: 10.1029/2002JE001865
107. Lindström, M., Ormö, J. and Sturkell, E. 2007. Water-blow and resurge breccias at the Lockne marine-target impact structure. *Geological Society of America*. **2437(03)** 43–54. doi: 10.1130/2008.2437(03)
108. Ormö, J., Sturkell, E. and Lindström, M. 2007. Sedimentological analysis of resurge deposits at the Lockne and Tvären craters: Clues to flow dynamics. *Meteoritics & Planetary Science*. **42(11)** 1929–1943. doi: 10.1111/j.1945-5100.2007.tb00551.x
109. Sturkell, E. F. F. 1998. Resurge morphology of the marine Lockne impact crater, Jämtland, central Sweden. *Geological Magazine*. **135(September 2000)** 121–127. doi: 10.1017/S0016756897007875
110. Stöffler, D. 1971. Progressive metamorphism and classification of shocked and brecciated crystalline rocks at impact craters. *Journal of Geophysical Research*. **76(23)** 5541.
111. Ghosh, S. and Bhaduri, S. K. 2003. Petrography and petrochemistry of impact melts from Lonar Crater. *Buldana district, Maharashtra, India, Indian Miner*. **57** 1–26.

112. Srivastava, P., Sangode, S. J. and Torrent, J. 2015. Mineral magnetic and diffuse reflectance spectroscopy characteristics of the Deccan volcanic bole beds: Implications to genesis and transformations of iron oxides. *Geoderma*. **239** 317–330.
113. Mussi, A., Cordier, P., Mainprice, D. and Frost, D. J. 2010. Transmission electron microscopy characterization of dislocations and slip systems in K-lingunite: Implications for the seismic anisotropy of subducted crust. *Physics of the Earth and Planetary Interiors*. **182(1-2)** 50–58. doi: 10.1016/j.pepi.2010.06.013
114. Anchuela, O. 2006. Magma flow directions in Azores basaltic dykes from AMS data: preliminary results from Corvo island. *Geogaceta*. **(1)** 83–86.
115. Bascou, J., Camps, P. and Marie Dautria, J. 2005. Magnetic versus crystallographic fabrics in a basaltic lava flow. *Journal of Volcanology and Geothermal Research*. **145(1-2)** 119–135. doi: 10.1016/j.jvolgeores.2005.01.007
116. Sen, K. and Mamtani, M. A. 2006. Magnetic fabric, shape preferred orientation and regional strain in granitic rocks. *Journal of structural geology*. **28(10)** 1870–1882.
117. Launeau, P. and Robin, P.-Y. F. 1996. Fabric analysis using the intercept method. *Tectonophysics*. **267(1-4)** 91–119. doi: 10.1016/S0040-1951(96)00091-1
118. Soffel, H. C. 1991. *Paläomagnetismus und Archäomagnetismus*. doi: 10.1007/978-3-642-76547-6
119. Dunlop, D. J. and Özdemir, Ö. 2001. *Rock magnetism: fundamentals and frontiers*. **3**
120. Butler, R. F. 1992. *Paleomagnetism: magnetic domains to geologic terranes*. **319**
121. Dubey, A. K. Understanding an Orogenic Belt.
122. De Wall, H. and Nano, L. 2004. The Use of Field Dependence of Magnetic Susceptibility for Monitoring Variations in Titanomagnetite Composition - A Case Study on Basanites from the Vogelsberg 1996 Drillhole, Germany. *Studia Geophysica et Geodaetica*. **48(4)** 767–776. doi: 10.1023/B:SGEG.0000045482.80307.1c
123. Wall, H. De. 2000. The Field-Dependence of AC Susceptibility in Titanomagnetites: Implications for the Anisotropy of Magnetic Susceptibility. *Geophysical research letters*. **27(16)** 2409.
124. Maiti, S., Meena, N. K., Sangode, S. J. and Chakrapani, G. J. 2005. Magnetic susceptibility studies of soils in Delhi. *JOURNAL-GEOLOGICAL SOCIETY OF INDIA*. **66(6)** 667.
125. Sangode, S. J., Kumar, R. and Ghosh, S. K. 1999. Palaeomagnetic and rock magnetic perspectives on the post-collision continental sediments of the Himalaya, India. *Geol. Soc. India Memoir*. **44** 221–248.
126. Kirschvink, J. L. 1980. The least-squares line and plane and the analysis of palaeomagnetic data. *Geophysical Journal International*. **62(3)** 699–718. doi: 10.1111/j.1365-246X.1980.tb02601.x
127. Tarling, D. and Hrouda, F. 1993. *Magnetic anisotropy of rocks*.
128. Jelinek, V. 1981. Characterization of the magnetic fabric of rocks. *Tectonophysics*. **79(3)** T63–T67.
129. Long, D. A. and Long, D. A. 1977. *Raman spectroscopy*. **206**
130. Larkin, P. 2011. *Infrared and Raman spectroscopy; principles and spectral interpretation*.
131. Haggerty, S. E. 1976. Oxidation of opaque mineral oxides in basalts. *Oxide minerals*. Hg1–Hg100.
132. Moskowitz, B., Jackson, M. and Kissel, C. 1998. Low-temperature magnetic behavior of titanomagnetites. *Earth and Planetary Science Letters*. **157(3-4)** 141–149.
133. Aragón, R., Buttrey, D., Shepherd, J. and Honig, J. 1985. Influence of nonstoichiometry on the Verwey transition. *Physical Review B*. **31(1)** 430–436. doi: 10.1103/PhysRevB.31.430
134. Senanayake, W. E. and McElhinny, M. W. 1981. Hysteresis and susceptibility characteristics of magnetite and titanomagnetites: interpretation of results from basaltic rocks. *Physics of the Earth and Planetary Interiors*. **26(1-2)** 47–55. doi: 10.1016/0031-9201(81)90096-0
135. Dunlop, D. J. 2002. Theory and application of the Day plot (M rs / M s versus H cr / H c) 1. Theoretical curves and tests using titanomagnetite data. *Journal of Geophysical Research*. **107(B3)** 2056. doi: 10.1029/2001JB000486

136. Dunlop, D. J. 2002. Theory and application of the Day plot (M rs / M s versus H cr / H c) 2. Application to data for rocks, sediments, and soils. *Journal of Geophysical Research*. **107(B3)** 2057. doi: 10.1029/2001JB000487
137. Oliva-Urcia, B., Kontny, A., Vahle, C. and Schleicher, A. M. 2011. Modification of the magnetic mineralogy in basalts due to fluid-rock interactions in a high-temperature geothermal system (Krafla, Iceland). *Geophysical Journal International*. **186** 155–174. doi: 10.1111/j.1365-246X.2011.05029.x
138. Jackson, M., Moskowitz, B., Rosenbaum, J. and Kissel, C. 1998. Field-dependence of AC susceptibility in titanomagnetites. *Earth and Planetary Science Letters*. **157(3-4)** 129–139.
139. Finlay, C. C. et al. 2010. International Geomagnetic Reference Field: the eleventh generation. *Geophysical Journal International*. **183(3)** 1216–1230. doi: 10.1111/j.1365-246X.2010.04804.x
140. Launeau, P. and Robin, P.-Y. F. P. 2005. Determination of fabric and strain ellipsoids from measured sectional ellipses—implementation and applications. *Journal of Structural Geology*. **27(12)** 2223–2233. doi: 10.1016/j.jsg.2005.08.003
141. Robin, P.-Y. F. 2002. Determination of fabric and strain ellipsoids from measured sectional ellipses — theory. *Journal of Structural Geology*. **24(3)** 531–544. doi: 10.1016/S0191-8141(01)00081-5
142. Ahrens, T. J. and O'Keefe, J. D. 1977. Equations of state and impact-induced shock-wave attenuation on the Moon. *Impact and explosion cratering*. **639** 656.
143. Huffman, A. R., Brown, J. M., Carter, N. L. and Reimold, W. U. 1993. The microstructural response of quartz and feldspar under shock loading at variable temperatures. *Journal of Geophysical Research*. **98** 22171. doi: 10.1029/93JB01425
144. Hrouda, F. 2002. Low-field variation of magnetic susceptibility and its effect on the anisotropy of magnetic susceptibility of rocks. *Geophysical Journal International*. **150(3)** 715–723. doi: 10.1046/j.1365-246X.2002.01731.x
145. Crawford, D. A. and Schultz, P. H. 1993. The production and evolution of impact-generated magnetic fields. *International Journal of Impact Engineering*. **14(1-4)** 205–216. doi: 10.1016/0734-743X(93)90021-X
146. Weiss, B. P. et al. 2010. Paleomagnetism of impact spherules from Lonar crater, India and a test for impact-generated fields. *Earth and Planetary Science Letters*. **298(1-2)** 66–76. doi: 10.1016/j.epsl.2010.07.028
147. Schöbel, S. and de Wall, H. 2014. AMS-NRM interferences in the Deccan basalts: Toward an improved understanding of magnetic fabrics in flood basalts. *Journal of Geophysical Research: Solid Earth*. **119(4)** 2651–2678. doi: 10.1002/2013JB010660
148. Park, J. K., Tanczyk, E. I. and Desbarats, A. 1988. Magnetic fabric and its significance in the 1400 Ma Mealy diabase dykes of Labrador, Canada. *Journal of Geophysical Research: Solid Earth (1978–2012)*. **93(B11)** 13689–13704.
149. Hargraves, R. B., Johnson, D. and Chan, C. Y. 1991. Distribution anisotropy: the cause of AMS in igneous rocks? *Geophysical Research Letters*. **18(12)** 2193–2196.
150. Wada, Y. 1992. Magma flow directions inferred from preferred orientations of phenocryst in a composite feeder dike, Miyake-Jima, Japan. *Journal of Volcanology and Geothermal Research*. **49(1-2)** 119–126. doi: 10.1016/0377-0273(92)90008-2
151. Potter, D. K. and Stephenson, A. 1988. Single-domain particles in rocks and magnetic fabric analysis. *Geophysical Research Letters*. **15(10)** 1097–1100.
152. Rochette, P., Jackson, M. and Aubourg, C. 1992. Rock magnetism and the interpretation of anisotropy of magnetic susceptibility. *Reviews of Geophysics*. **30(3)** 209. doi: 10.1029/92RG00733
153. Rochette, P., Aubourg, C. and Perrin, M. 1999. Is this magnetic fabric normal? A review and case studies in volcanic formations. *Tectonophysics*. **307(1-2)** 219–234. doi: 10.1016/S0040-1951(99)00127-4
154. Cañón-Tapia, E., Walker, G. P. L. and Herrero-Bervera, E. 1997. The internal structure of lava flows—insights from AMS measurements II: Hawaiian pahoehoe, toothpaste lava and "a"ā.

Journal of Volcanology and Geothermal Research. **76(1-2)** 19–46. doi: 10.1016/S0377-0273(96)00073-X

155. Cañón-Tapia, E., Walker, G. P. L. and Herrero-Bervera, E. 1996. The internal structure of lava flows—insights from AMS measurements I: Near-vent a'a. *Journal of Volcanology and Geothermal Research*. **70(1-2)** 21–36. doi: 10.1016/0377-0273(95)00050-X
156. Carporzen, L., Gilder, S. A. and Hart, R. J. 2005. Palaeomagnetism of the Vredefort meteorite crater and implications for craters on Mars. *Nature*. **435(7039)** 198–201. doi: 10.1038/nature03560
157. Pierazzo, E. and Melosh, H. 1999. Hydrocode modeling of Chicxulub as an oblique impact event. *Earth and Planetary Science Letters*. **165** 163–176.
158. Pierazzo, E. and Melosh, H. J. 2000. Understanding oblique impacts from experiments, observations, and modeling. *Annual review of earth and planetary sciences*. **28** 141–67. doi: 10.1146/annurev.earth.28.1.141
159. Ewing, W. M., Jardetzky, W. S., Press, F. and Beiser, A. 1957. *Elastic Waves in Layered Media*. *Physics Today*. **10(12)** 27. doi: 10.1063/1.3060203
160. Norris, L. 2012. STRESS WAVE PROPAGATION IN SOLIDS. *High-Velocity Impact Phenomena*. 23.
161. Virieux, J. 1986. P-SV wave propagation in heterogeneous media: Velocity-stress finite-difference method. *GEOPHYSICS*. **51(4)** 889–901. doi: 10.1190/1.1442147
162. Ahrens, T. J. 2002. Depth of Cracking beneath Impact Craters: New Constraint for Impact Velocity. *AIP Conference Proceedings*. **620(2002)** 1393–1396.
163. Srivastava, H. B., Hudleston, P. and Earley III, D. 1995. Strain and possible volume loss in a high-grade ductile shear zone. *Journal of Structural Geology*. **17(9)** 1217–1231.
164. Srivastava, H. B., Sahai, A. and Lal, S. N. 2000. Strain and crystallographic fabric in mesoscopic ductile Shear Zones of Garhwal Himalaya. *Gondwana Research*. **3(3)** 395–404.
165. Hudleston, P. J. and Srivastava, H. B. 1997. in *Evolution of Geological Structures in Micro-to Macro-scales*. 259–271.
166. Mamtani, M. A. and Greiling, R. O. 2005. Granite emplacement and its relation with regional deformation in the Aravalli Mountain Belt (India)—inferences from magnetic fabric. *Journal of structural geology*. **27(11)** 2008–2029.
167. Majumder, S. and Mamtani, M. A. 2009. Magnetic fabric in the Malanjkhand Granite (central India)—implications for regional tectonics and Proterozoic suturing of the Indian shield. *Physics of the Earth and Planetary Interiors*. **172(3)** 310–323.
168. Sen, K., Majumder, S. and Mamtani, M. A. 2005. Degree of magnetic anisotropy as a strain intensity gauge in ferromagnetic granites. *Journal of the Geological Society*. **162(4)** 583–586.
169. Sen, K., Dubey, A. K., Tripathi, K. and Pfänder, J. A. 2012. Composite mesoscopic and magnetic fabrics of the Paleo-Proterozoic Wangtu Gneissic Complex, Himachal Himalaya, India: Implications for ductile deformation and superposed folding of the Himalayan basement rocks. *Journal of Geodynamics*. **61** 81–93.
170. Hart, R. J. et al. 1995. Magnetic anomaly near the center of the Vredefort structure: Implications for impact-related magnetic signatures. *Geology*. **23(3)** 277–280.
171. Cloete, M. et al. 1999. Characterization of magnetite particles in shocked quartz by means of electron- and magnetic force microscopy: Vredefort, South Africa. *Contributions to Mineralogy and Petrology*. **137(3)** 232–245. doi: 10.1007/s004100050548
172. Carporzen, L., Gilder, S. and Hart, R. 2006. Origin and implications of two Verwey transitions in the basement rocks of the Vredefort meteorite crater, South Africa. *Earth and Planetary Science Letters*. **251(3-4)** 305–317. doi: 10.1016/j.epsl.2006.09.013
173. Agarwal, A., Kontny, A., Srivastava, D. and Greiling, R. O. 2014. *Shock pressure estimates in target basalts of a pristine crater: a case study in the Lonar crater, India*. doi: under review
174. Gurov, E. P., Koeberl, C. and Yamnichenko, A. 2007. El'gygytgyn impact crater, Russia: Structure, tectonics, and morphology. *Meteoritics & Planetary Science*. **42(3)** 307–319. doi: 10.1111/j.1945-5100.2007.tb00235.x

175. Mattsson, H. J. and Elming, S.-Å. 2001. Magnetic fabrics and paleomagnetism of the Storsjön–Edsbyn deformation zone, central Sweden. *Precambrian Research*. **107(3-4)** 265–281. doi: 10.1016/S0301-9268(00)00145-5
176. Shuvalov, V. 2003. in *Impact markers in the stratigraphic record*. 121–135.
177. Sharp, T. G. and Decarli, P. S. 2006. in *Meteorites and the early solar system II*. **943** 653–677.
178. Högström, A. E. S. et al. 2010. Concentric impact structures in the Palaeozoic of Sweden – the Lockne and Siljan craters. *GFF*. **132(1)** 65–70. doi: 10.1080/11035890903469971
179. Bahat, D. 1991. *Tectonofractography*. doi: 10.1007/978-3-642-76162-1_5
180. Bahat, D. 1986. Joints and en échelon cracks in Middle Eocene chalks near Beer Sheva, Israel. *Journal of Structural Geology*. **8(2)** 181–190. doi: 10.1016/0191-8141(86)90108-2
181. Leith, K., Moore, J. R., Amann, F. and Loew, S. 2014. Subglacial extensional fracture development and implications for Alpine Valley evolution. *Journal of Geophysical Research: Earth Surface*. **119(1)** 62–81. doi: 10.1002/2012JF002691
182. Bahat, D. 1989. Fracture stresses at shallow depths during burial. *Tectonophysics*. **169(1-3)** 59–65. doi: 10.1016/0040-1951(89)90183-2
183. Bahat, D. 1999. Single-layer burial joints vs single-layer uplift joints in Eocene chalk from the Beer Sheva syncline in Israel. *Journal of Structural Geology*. **21(3)** 293–303. doi: 10.1016/S0191-8141(98)00118-7
184. Leith, K., Moore, J. R., Amann, F. and Loew, S. 2014. In situ stress control on microcrack generation and macroscopic extensional fracture in exhuming bedrock. *Journal of Geophysical Research: Solid Earth*. **119(1)** 594–615. doi: 10.1002/2012JB009801
185. Collins, G. S., Melosh, H. J. and Ivanov, B. a. 2004. Modeling damage and deformation in impact simulations. *Meteoritics and Planetary Science*. **39(2)** 217–231. doi: 10.1111/j.1945-5100.2004.tb00337.x
186. Kenkmann, T., Poelchau, M. H. and Wulf, G. 2014. Structural geology of impact craters. *Journal of Structural Geology*. **62** 156–182. doi: 10.1016/j.jsg.2014.01.015
187. Acosta-Maeda, T. E., Scott, E. R. D., Sharma, S. K. and Misra, A. K. 2013. The pressures and temperatures of meteorite impact: Evidence from micro-Raman mapping of mineral phases in the strongly shocked Taiban ordinary chondrite. *American Mineralogist*. **98(5-6)** 859–869. doi: 10.2138/am.2013.4300
188. Mernagh, T. P. 1991. Use of the laser Raman microprobe for discrimination amongst feldspar minerals. *Journal of Raman Spectroscopy*. **22(8)** 453–457. doi: 10.1002/jrs.1250220806
189. Freeman, J. J. et al. 2008. Characterization of natural feldspars by Raman spectroscopy for future planetary exploration. *The Canadian Mineralogist*. **46(6)** 1477–1500. doi: 10.3749/canmin.46.6.1477
190. RRUFF database. 2014. RRUFF.
191. Liu, L. and El Gorsey, A. 2007. High-Pressure Phase Transitions of the Feldspars, and Further Characterization of Lingunite. *International Geology Review*. **49(9)** 854–860. doi: 10.2747/0020-6814.49.9.854
192. Liu, L. et al. 2008. Raman spectroscopic study of K-lingunite at various pressures and temperatures. *Physics and Chemistry of Minerals*. **36(3)** 143–149. doi: 10.1007/s00269-008-0264-0
193. Ozawa, S. et al. 2009. Transformation textures, mechanisms of formation of high-pressure minerals in shock melt veins of L6 chondrites, and pressure-temperature conditions of the shock events. *Meteoritics & Planetary Science*. **44(11)** 1771–1786. doi: 10.1111/j.1945-5100.2009.tb01206.x
194. Baziotis, I. P. et al. 2013. The Tissint Martian meteorite as evidence for the largest impact excavation. *Nature communications*. **4** 1404. doi: 10.1038/ncomms2414
195. Zhang, W. F. et al. 2000. Raman scattering study on anatase TiO 2 nanocrystals. *Journal of Physics D: Applied Physics*. **33(8)** 912–916. doi: 10.1088/0022-3727/33/8/305

196. Fritz, J., Greshake, a. and Stoffler, D. 2005. Micro-Raman spectroscopy of plagioclase and maskelynite in Martian meteorites: Evidence of progressive shock metamorphism. *Antarctic Meteorite Research*. **18** 96–116.
197. Botkovitz, P. et al. 1994. Electrochemical and Neutron Diffraction Study of a Prelithiated Hollandite-Type Li x MnO 2 Phase. *Molecular Crystals and Liquid Crystals Science and Technology. Section A. Molecular Crystals and Liquid Crystals*. **244(1)** 233–238. doi: 10.1080/10587259408050110
198. Sanc, I. 1990. Sanc, I. *The International Centre for Diffraction Data*.
199. Bass, R. F. 1995. *Probabilistic techniques in analysis*.
200. Kubo, T. et al. 2010. Plagioclase breakdown as an indicator for shock conditions of meteorites. *Nature Geoscience*. **3(1)** 41–45. doi: 10.1038/ngeo704
201. Ralph, J. and Ida, C. 2014. Mineral data.
202. Younes, A. I. and Engelder, T. 1999. Fringe cracks: key structures for the interpretation of the progressive Alleghanian deformation of the Appalachian plateau. *Geological Society of America Bulletin*. **111(2)** 219–239.
203. Kanninen, M. F. and Popelar, C. L. 1985. Advanced fracture mechanics.
204. Kerkhof, F. 1973. General Lecture Wave fractographic investigations of brittle fracture dynamics. in *Proceedings of an international conference on Dynamic Crack Propagation*. 3–35.
205. Preston, F. W. 1931. THE PROPAGATION OF FISSURES IN GLASS AND OTHER BODIES WITH SPECIAL REFERENCE TO THE SPLIT-WAVE FRONT. *Journal of the American Ceramic Society*. **14(6)** 419–427.
206. Beall, G. H. et al. 1986. Effect of test method and crack size on the fracture toughness of a chain-silicate glass-ceramic. *Journal of materials science*. **21(7)** 2365–2372.

Abbreviations

δ: vacancy concentration

σ_1: maximum stress direction

σ_{1c}: **σ_1** during compression

σ_{1D}: **σ_1** during de-compression

χ: bulk magnetic susceptibility

χ_{Hd}: field dependence parameter for χ

χ-T: temperature dependent low-field χ

P'_{Hd}: field dependence parameter for P'

AF: alternating field

AMS: anisotropy of magnetic susceptibility

BSE: backscattered electrons

D: declination in degrees

EDX: energy-dispersive X-ray spectroscopy

FIB: focused ion beam

H: external magnetic field

HC: high coercivity component of NRM

Hc: coercive force

Hcr: coercivity

HRTEM: high resolution TEM

J: magnetization

J_i: induced magnetization

I: inclination in degress

IRM: isothermal remnant magnetization

K_1: longest axis of SPO ellipsoid

K_2: intermediate axis of SPO ellipsoid

K_3: shortest axis of SPO ellipsoid

k_1: longest axis of AMS ellipsoid

k_2: intermediate axis of AMS ellipsoid

k_3: shortest axis of AMS ellipsoid

k_m: mean magnetic susceptibility

LC: low coercivity component of NRM

MD: multi-domain

MDF: median destructive field

M_{rs}: remanent magnetization

M_s: saturation remanence

NRM: natural remanent magnetization

P': magnetic anisotropy

PLM: polarized light microscopy

PSD: Pseudo-single-domain

Q: Königsberger ratio

R_C: crater radius

SD: Single domain

SE: secondary electron

SPO: shape preferred orientation

T_C: Curie temperature

TEM: transmission electron microscopy

T_{mean}: shape parameter

Ti: titanium

T_V: Verwey transition temperature

Appendix

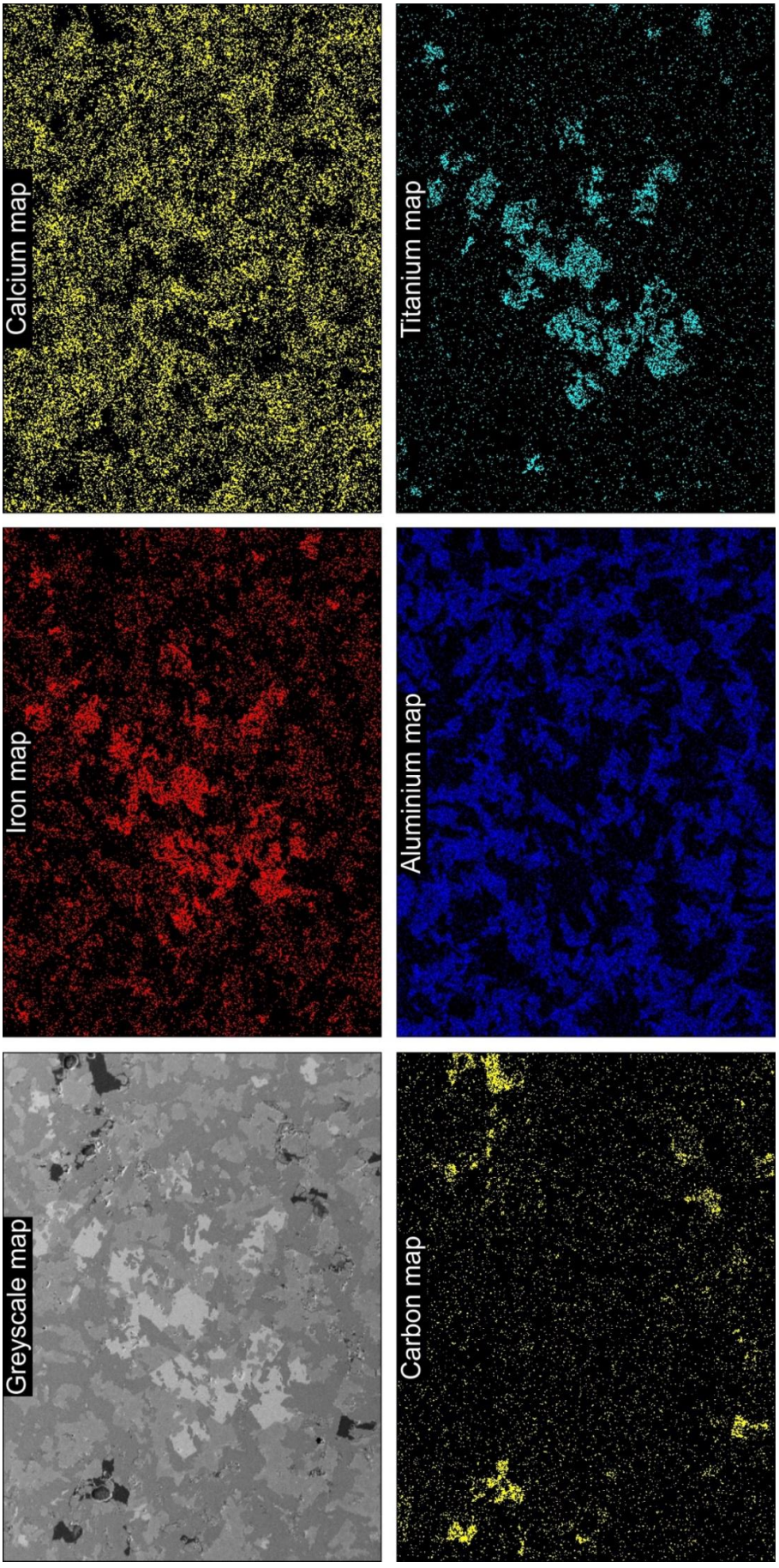

Figure Af1: Elemental mapping of basalt thin sections. Elemental maps show relative abundance of an element in the thin-section (sample 1).

Figure Af1: Elemental mapping of basalt thin sections. Elemental maps show relative abundance of an element in the thin-section (sample 5).

Figure Af1: Elemental mapping of basalt thin sections. Elemental maps show relative abundance of an element in the thin-section (sample 8).

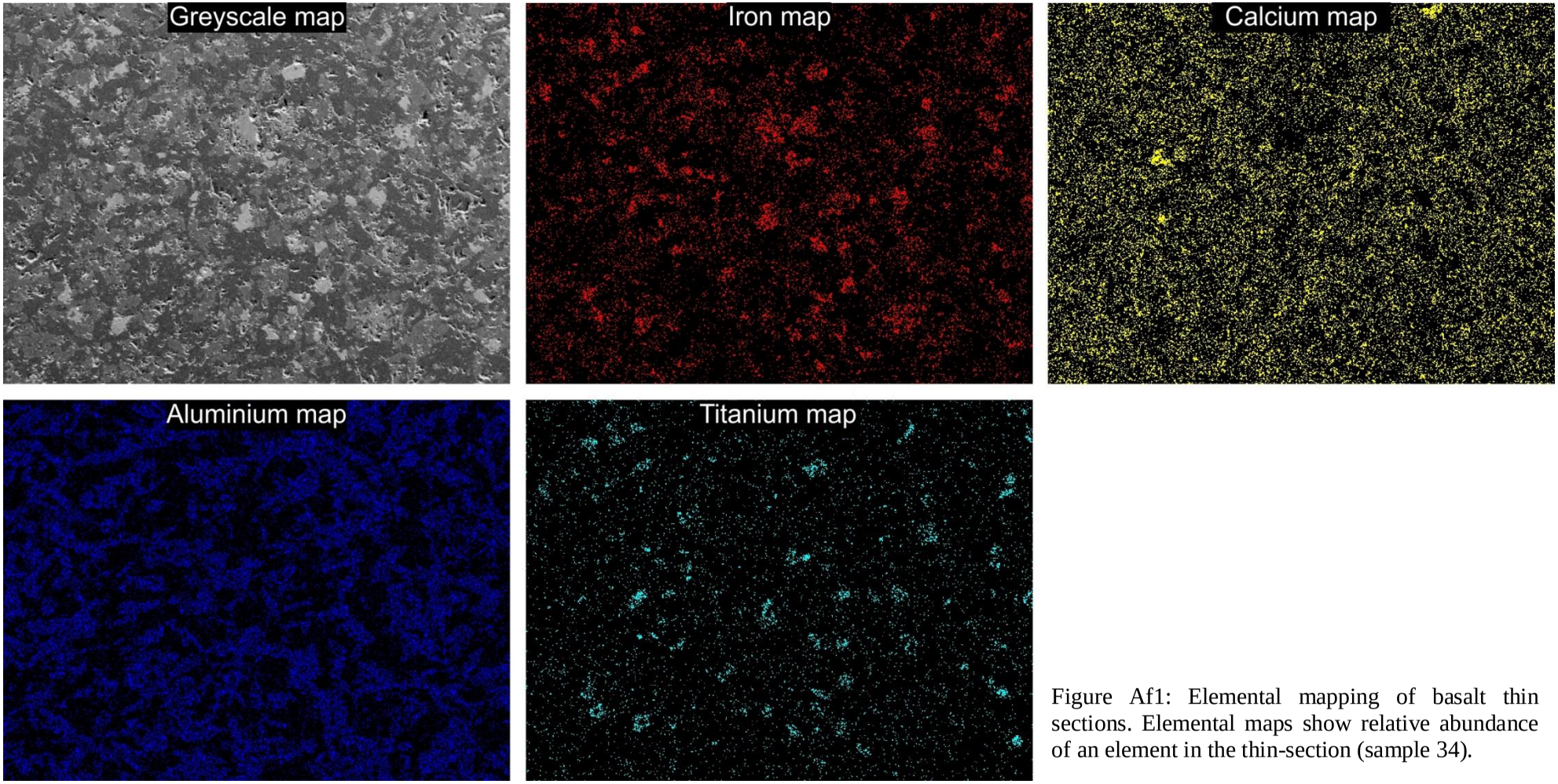

Figure Af1: Elemental mapping of basalt thin sections. Elemental maps show relative abundance of an element in the thin-section (sample 34).

Table AT1. AMS data, representing mean of values from cores (n) collected from each site (sample no.), k_1d, k_2d and k_3d are the declination; k_1i, k_2i and k_3i are the inclination and k_1, k_2 and k_3 are the intensities of maximum (k_1), intermediate (k_2) and minimum (k_3) susceptibility axes of AMS ellipsoid. k_m= mean susceptibility. P'=corrected degree of magnetic anisotropy. T_{mean}= shape parameter. $k_m = (k_1+k_2+k_3)/3$; $P' = \exp \sqrt{[2(\eta_1-\eta_m)^2+(\eta_2-\eta_m)^2+(\eta_3-\eta_m)^2]}$; $T_{mean} = (2\eta_2-\eta_1-\eta_3)/(\eta_1-\eta_3)$;Here $\eta_1=\ln k_1$; $\eta_2=\ln k_2$; $\eta_3=\ln k_3$ and $\eta_m=(\eta 1.\ \eta 2.\ \eta 3)^{1/3}$ k_2 [127].

Sample No	k_m (10^{-3} SI	k_1	k_2	k_3	k_1d	k_1i	k_2d	k_2i	k_3d	k_3i	P`	T
1.1	26.020	1.004	1.001	0.995	17	62	286	1	195	28	1.009	0.35
1.2	25.860	1.003	1.002	0.995	42	60	291	12	195	27	1.009	0.77
1.3	25.060	1.003	1.001	0.996	13	55	276	5	182	35	1.007	0.44
1.4	27.630	1.003	1.001	0.996	46	56	288	18	188	28	1.008	0.34
1.5	28.880	1.003	1.001	0.995	41	58	291	12	194	29	1.008	0.53
1.6	26.380	1.004	1.002	0.995	61	49	294	28	188	27	1.009	0.52
1.7	25.210	1.003	1.001	0.996	46	59	288	16	190	26	1.008	0.34
1.8	26.980	1.002	1.002	0.996	28	59	288	6	194	30	1.007	0.81
3.1	22.870	1.004	1.002	0.994	336	77	211	8	120	11	1.010	0.62
3.2	21.350	1.003	1.001	0.996	93	57	344	12	246	30	1.008	0.50
3.3	22.910	1.003	1.002	0.995	342	77	203	10	112	8	1.009	0.75
3.4	19.180	1.004	1.001	0.996	126	57	340	28	241	15	1.009	0.17
3.5	19.670	1.004	1.001	0.995	345	57	181	32	86	7	1.009	0.27
3.6	20.100	1.004	1.001	0.995	112	62	340	20	243	19	1.009	0.28
4.1	46.070	1.011	1.001	0.988	283	46	162	26	54	32	1.024	0.17
4.2	43.950	1.007	1.003	0.990	265	31	151	33	27	41	1.017	0.59
4.3	41.880	1.005	1.003	0.992	275	27	161	38	30	40	1.014	0.59
4.4	43.590	1.011	1.003	0.986	292	42	150	41	41	20	1.025	0.32
4.5	46.690	1.011	1.003	0.987	266	34	158	25	40	46	1.025	0.33
5.1	34.900	1.011	1.005	0.985	331	7	61	6	191	81	1.028	0.51
5.2	31.280	1.013	1.004	0.983	303	10	35	7	161	78	1.032	0.41
5.3.1	37.650	1.012	1.004	0.984	292	0	22	15	202	75	1.029	0.46
5.3.2	37.660	1.012	1.004	0.984	292	0	22	15	202	75	1.029	0.46
5.4	31.260	1.010	1.004	0.985	86	3	355	10	190	80	1.026	0.54
6.1	26.630	1.006	1.005	0.989	13	50	125	17	228	35	1.019	0.84
6.2	27.020	1.007	1.004	0.989	349	28	106	41	236	36	1.019	0.70
6.3	26.980	1.007	1.005	0.988	176	16	293	58	78	27	1.020	0.80
6.4	27.580	1.006	1.005	0.989	181	17	294	52	80	33	1.019	0.81
6.5	25.050	1.006	1.005	0.989	190	31	327	50	86	22	1.019	0.77
7.1.1	18.630	1.004	1.001	0.995	94	4	4	3	241	85	1.009	0.27
7.1.2	18.630	1.004	1.001	0.995	94	4	4	3	242	85	1.009	0.27
7.2.1	21.010	1.002	1.001	0.996	315	7	45	1	141	83	1.007	0.67
7.2.2	21.010	1.002	1.001	0.996	314	5	44	1	144	85	1.007	0.68
7.3	18.850	1.003	1.002	0.995	306	3	216	1	97	87	1.009	0.65
8.1	38.000	1.006	1.003	0.992	151	29	268	39	36	37	1.015	0.57
8.2	35.590	1.004	1.002	0.994	315	2	224	36	47	54	1.010	0.72
8.3	33.850	1.004	1.003	0.994	145	26	259	41	32	38	1.011	0.81
8.4	34.950	1.005	1.003	0.992	154	23	259	32	35	49	1.014	0.77
8.5	35.310	1.003	1.001	0.996	141	19	248	40	31	44	1.007	0.35
10.1	71.140	1.005	1.000	0.995	80	62	292	24	196	13	1.011	0.00
10.2	80.070	1.005	1.000	0.995	94	61	288	29	194	6	1.010	0.11
10.3	79.870	1.007	0.998	0.994	125	73	300	17	31	1	1.013	-0.39
10.4	74.720	1.005	1.001	0.994	88	74	288	15	197	5	1.012	0.33
10.5	70.490	1.003	1.000	0.997	113	72	279	18	11	4	1.006	0.23
11.1	20.040	1.005	1.002	0.992	91	25	186	10	297	63	1.014	0.54
11.2	45.390	1.006	1.002	0.993	305	35	45	15	154	51	1.013	0.42
11.3	41.880	1.006	1.001	0.993	114	32	207	4	304	58	1.013	0.27

11.4	18.730	1.007	1.003	0.991	87	21	186	23	319	58	1.017	0.48
11.5	17.800	1.006	1.002	0.992	12	22	269	28	134	53	1.014	0.52
12A.1	47.930	1.008	1.002	0.990	37	26	131	9	239	63	1.018	0.28
12A.2	51.110	1.009	1.001	0.991	34	28	127	6	229	61	1.018	0.10
12A.3	49.180	1.009	1.002	0.989	47	25	139	3	235	64	1.020	0.27
12A.4	45.380	1.010	1.002	0.989	43	23	134	3	231	67	1.021	0.24
12B.1	53.870	1.011	1.001	0.988	355	40	109	26	222	39	1.023	0.16
12B.2	45.420	1.012	1.001	0.987	357	42	99	14	204	45	1.025	0.15
13.1	31.900	1.002	1.000	0.998	321	39	119	49	222	11	1.004	0.31
13.2	29.470	1.005	1.000	0.996	285	53	162	23	59	28	1.009	-0.01
13.3	29.540	1.006	1.000	0.994	277	54	53	28	155	21	1.012	-0.02
13.4	31.790	1.004	0.999	0.997	360	47	128	30	236	28	1.006	-0.35
13.5	31.520	1.005	1.001	0.993	286	42	63	39	173	23	1.012	0.30
13.6	28.790	1.005	1.002	0.993	262	24	45	61	165	16	1.013	0.46
14.1	64.750	1.002	1.000	0.999	63	34	314	26	195	45	1.003	-0.32
14.2	55.790	1.004	1.001	0.995	294	4	26	30	197	60	1.010	0.42
14.3	58.340	1.003	1.000	0.997	40	12	309	5	197	77	1.005	0.16
14.4	65.900	1.003	1.000	0.997	84	1	353	37	175	53	1.006	0.11
14.5	61.970	1.006	1.000	0.994	264	11	358	19	145	68	1.012	0.11
14.6	63.570	1.003	1.001	0.996	293	8	25	16	178	72	1.007	0.44
15.1	45.390	1.006	1.004	0.990	185	31	340	56	88	11	1.018	0.77
15.2	61.450	1.010	1.006	0.985	167	39	8	49	266	11	1.027	0.69
15.3	43.560	1.007	1.005	0.988	329	35	194	45	77	24	1.022	0.76
15.4	47.400	1.006	1.004	0.989	212	59	354	26	93	16	1.019	0.78
15.5	48.640	1.007	1.006	0.987	355	7	247	69	87	19	1.023	0.83
16.1	76.100	1.003	1.001	0.997	229	26	46	64	138	1	1.006	0.44
16.2	69.300	1.004	1.001	0.996	35	65	251	21	156	14	1.009	0.16
16.3	75.500	1.002	1.001	0.997	24	65	225	24	131	8	1.005	0.29
16.4	72.100	1.002	1.001	0.997	240	17	26	70	147	11	1.005	0.45
16.5	72.300	1.003	0.999	0.998	10	73.5	249	8	157	15	1.006	-0.58
17.1.1	53.600	1.018	1.011	0.971	146	26	272	51	42	27	1.052	0.70
17.1.2	53.600	0.102	1.011	0.971	148	28	273	47	40	29	1.052	0.70
17.2.1	64.900	1.011	0.100	0.986	283	26	150	55	24	22	1.025	0.37
17.2.2	64.900	1.011	0.100	0.987	285	27	153	53	28	23	1.025	0.38
17.3.1	60.600	1.015	1.010	0.975	149	36	277	41	36	29	1.045	0.72
17.3.2	60.600	1.016	1.010	0.975	148	35	277	42	36	28	1.045	0.72
18.5	14.950	1.006	1.002	0.991	125	1	216	38	34	52	1.016	0.44
18.1	19.050	1.007	1.003	0.991	295	3	202	35	29	55	1.017	0.48
18.2	18.770	1.007	1.002	0.991	305	2	213	42	36	48	1.017	0.37
18.3	21.670	1.008	1.003	0.990	297	7	201	39	36	50	1.019	0.41
18.4	21.890	1.008	1.002	0.990	298	3	207	33	32	57	1.018	0.30
19.1	20.750	1.007	1.002	0.991	13	28	247	47	120	29	1.017	0.37
19.2	17.220	1.007	1.001	0.993	26	9	286	47	125	41	1.014	0.14
19.3	19.540	1.007	1.001	0.991	26	17	281	38	135	47	1.016	0.26
19.4	18.630	1.007	1.001	0.992	12	26	253	45	121	34	1.016	0.19
19.5	19.780	1.007	1.001	0.992	12	17	262	47	116	38	1.015	0.25
20.1	21.460	1.007	1.001	0.992	202	15	314	54	102	32	1.015	0.27
20.2	23.230	1.007	1.002	0.991	199	3	295	59	107	31	1.016	0.46
20.3	17.880	1.008	1.000	0.992	180	40	281	13	25	47	1.016	-0.05
20.4	27.680	1.007	1.003	0.990	202	12	311	56	105	31	1.018	0.50
20.5	18.550	1.006	1.002	0.992	197	9	302	57	102	32	1.015	0.42
21.1	40.610	1.006	1.005	0.989	5	2	96	24	270	66	1.019	0.79
21.2	38.850	1.006	1.004	0.990	1	4	93	26	263	64	1.018	0.67
21.3	38.760	1.005	1.004	0.991	14	10	112	38	272	50	1.017	0.81
21.4	39.450	1.006	1.004	0.991	180	1	89	37	271	53	1.016	0.74
21.5	37.460	1.004	1.002	0.995	25	15	126	34	276	52	1.009	0.53

22.1.1	27.000	1.007	1.000	0.993	358	53	154	35	252	12	1.014	-0.11
22.1.2	26.990	1.007	1.000	0.993	358	54	155	33	252	11	1.014	-0.09
22.2	27.140	1.008	0.999	0.993	357	45	151	42	254	13	1.015	-0.14
22.3	27.410	1.009	0.998	0.994	17	49	185	41	280	6	1.015	-0.42
22.4	27.330	1.007	0.998	0.995	15	60	170	28	266	11	1.013	-0.37
23.1	38.670	1.007	1.000	0.993	150	8	57	22	259	67	1.014	0.01
23.2	36.510	1.008	1.000	0.992	145	1	54	10	241	80	1.016	0.01
23.3	38.030	1.007	1.001	0.992	149	0	59	16	240	74	1.015	0.10
23.4	38.510	1.008	1.001	0.992	334	1	64	10	240	80	1.016	0.19
23.5	36.360	1.007	1.001	0.992	149	10	57	11	279	75	1.016	0.11
23.6	36.490	1.008	1.000	0.992	145	3	54	28	241	62	1.016	0.01
24.1	54.600	1.017	0.999	0.984	177	42	329	44	74	14	1.034	-0.10
24.2	47.020	1.014	0.998	0.988	166	52	342	38	73	2	1.026	-0.21
24.3	51.530	1.018	0.999	0.983	183	48	342	40	81	11	1.035	-0.08
24.4	55.100	1.024	0.998	0.979	191	38	345	49	91	13	1.046	-0.14
24.5	56.730	1.016	1.003	0.981	180	48	354	42	87	3	1.036	0.24
25.2	46.120	1.009	1.003	0.988	212	22	120	6	15	67	1.022	0.45
25.1	56.320	1.007	1.001	0.993	205	38	114	1	23	52	1.014	0.22
25.3	55.000	1.007	1.004	0.990	161	18	260	26	40	58	1.018	0.64
25.4	52.740	1.007	1.000	0.994	178	41	84	5	349	48	1.013	-0.11
25.5	47.650	1.009	1.002	0.989	231	20	138	8	27	68	1.021	0.32
25.6	53.020	1.010	1.005	0.986	225	24	131	7	26	65	1.026	0.58
25.7	45.720	1.004	1.002	0.994	188	31	287	13	37	55	1.011	0.56
25.8	49.000	1.006	1.003	0.991	255	25	163	4	65	64	1.016	0.64
26.1	30.210	1.004	1.001	0.995	5	55	101	4	193	35	1.009	0.24
26.2	30.440	1.003	1.002	0.996	345	15	117	68	251	15	1.008	0.72
26.3	31.280	1.003	1.002	0.995	305	10	50	55	208	33	1.009	0.85
26.4	30.500	1.004	1.002	0.994	14	55	117	9	213	33	1.010	0.75
26.5	32.100	1.003	1.003	0.994	334	27	89	40	221	39	1.010	0.86
26.6	31.800	1.004	1.001	0.996	20	35	119	13	226	52	1.008	0.18
27.1	30.660	1.006	1.003	0.992	167	14	262	22	47	63	1.015	0.53
27.2	33.050	1.008	1.002	0.989	181	19	278	19	51	63	1.020	0.39
27.3	32.980	1.008	1.003	0.989	171	13	265	17	45	69	1.020	0.55
27.4	33.010	1.008	1.004	0.988	179	21	277	19	45	61	1.022	0.55
27.5	30.660	1.006	1.003	0.991	174	16	270	21	49	63	1.017	0.58
28.2	54.980	1.012	1.005	0.982	305	66	148	23	54	8	1.032	0.54
28.1	56.190	1.013	1.007	0.980	285	74	151	11	59	11	1.036	0.59
28.3	44.100	1.010	1.005	0.985	258	81	151	3	61	9	1.026	0.61
28.4	52.890	1.012	1.005	0.984	188	67	325	18	60	15	1.029	0.50
28.5	47.790	1.007	1.003	0.990	291	82	153	6	62	6	1.018	0.55
29.1	48.550	1.007	1.002	0.991	341	31	216	43	92	31	1.017	0.44
29.2	45.630	1.006	1.004	0.991	337	36	206	42	88	27	1.016	0.76
29.3	48.810	1.007	1.003	0.990	344	16	227	58	83	27	1.018	0.51
29.4	38.750	1.005	1.004	0.991	337	34	218	36	96	36	1.015	0.84
29.5	49.490	1.010	1.003	0.987	3	35	228	45	111	24	1.024	0.45
30.1	29.910	1.005	1.002	0.993	200	41	319	29	72	35	1.013	0.58
30.2	30.030	1.004	1.003	0.994	327	7	233	28	70	61	1.011	0.84
30.3	30.130	1.005	1.001	0.994	218	30	318	16	73	55	1.012	0.22
30.4.1	30.600	1.004	1.003	0.994	199	6	294	38	101	51	1.011	0.86
30.4.2	30.640	1.004	1.003	0.994	230	28	335	27	101	50	1.011	0.86
31.1	51.550	1.011	1.004	0.985	277	45	148	32	39	28	1.028	0.44
31.2	54.590	1.009	1.006	0.986	262	58	144	17	45	27	1.026	0.74
31.3	51.450	1.009	1.007	0.984	260	51	137	23	34	29	1.028	0.80
31.4	52.230	1.010	1.005	0.986	270	52	143	25	40	27	1.026	0.56
31.5	56.820	1.011	1.006	0.984	276	48	134	35	29	20	1.030	0.64
31.6	53.500	1.017	1.001	0.982	271	37	129	46	17	19	1.036	0.08

31.7	59.530	1.014	1.004	0.983	278	37	153	37	35	31	1.032	0.39
31.8	48.320	1.008	1.008	0.984	298	22	177	52	41	29	1.028	0.96
31.9	50.350	1.009	1.007	0.984	273	45	144	32	35	27	1.028	0.78
32.1	30.090	1.007	1.003	0.990	63	8	333	0	242	82	1.019	0.52
32.2	31.200	1.007	1.004	0.990	78	11	169	5	285	78	1.019	0.65
32.3	32.340	1.005	1.003	0.992	59	11	150	7	271	77	1.014	0.71
32.4	29.590	1.007	1.003	0.991	69	4	160	11	318	78	1.017	0.51
32.5	28.690	1.006	1.004	0.990	64	9	332	13	188	74	1.017	0.78
33.1	32.740	1.005	1.004	0.991	162	21	254	6	358	68	1.016	0.85
33.2	31.660	1.005	1.005	0.991	148	13	241	15	17	70	1.017	0.95
33.3.1	33.120	1.005	1.004	0.992	164	24	72	5	331	66	1.015	0.77
33.3.2	33.110	1.005	1.004	0.991	167	24	74	5	333	66	1.015	0.75
33.4	31.950	1.005	1.004	0.991	177	23	268	2	3	67	1.015	0.77
34.1	39.410	1.007	1.005	0.988	143	10	236	16	23	71	1.021	0.77
34.2	34.970	1.006	1.005	0.989	243	3	152	17	341	73	1.019	0.82
34.3	55.270	1.006	1.004	0.990	222	19	124	22	349	60	1.017	0.79
34.4	48.970	1.006	1.005	0.990	228	8	136	17	344	71	1.018	0.86
34.5	46.620	1.007	1.006	0.987	128	9	223	28	22	61	1.023	0.94
34.6	55.770	1.007	1.004	0.990	224	12	130	19	344	67	1.018	0.67

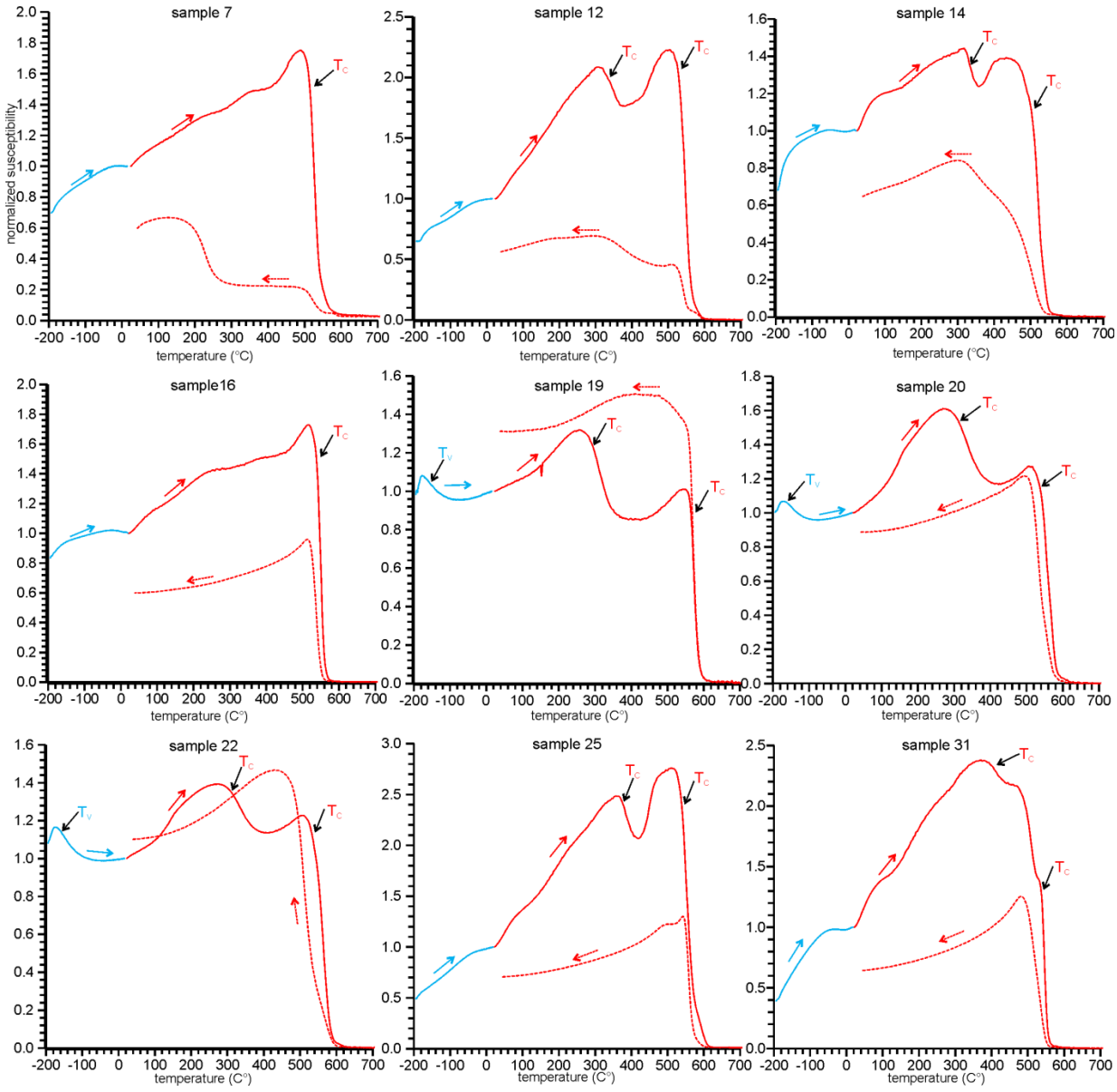

Figure AF2. Magnetic susceptibility (normalised by the susceptibility at 40°C) vs. temperature curves.

Table AT2. A comparison of bulk susceptibility of individual cylinder samples with different applied field. $\chi_{Hd}[\%]=[(\chi_{300A/m} - \chi_{50A/m})/\chi_{300 A/m}])*100$

Sample	Bulk Susceptibility		χhd
	50A/m	300A/m	
4.2	0.215	0.222	3.15315
26.4	0.166	0.166	-0.06035
19.2	0.095	0.095	-0.47574
25.8	0.250	0.257	2.53115
22.2	0.149	0.149	-0.06702
6.2	0.148	0.148	-0.06748
34.2	0.190	0.190	0.15773
8.2	0.185	0.188	1.49095
3.6	0.109	0.110	0.18248
24.4	0.260	0.280	6.86695
1.7	0.138	0.138	0.07267
7.1	0.103	0.102	-0.88496
14.4	0.349	0.349	-0.02865
31.7	0.296	0.301	1.56198
12A.2	0.244	0.245	0.12265
16.1	0.408	0.408	0.12243
27.4	0.177	0.177	0.16949
20.1	0.119	0.118	-0.42265
11.5	0.099	0.098	-0.46848

Table AT3. A Comparison of P’ from individual cylinder samples with different applied field. $P'_{Hd} = [(P'_{300A/m} – P'_{50A/m})/P'_{300 A/m}])*100$.

Sample	P`		$P'_{Hd\ \%}$
	300 A/m	50 A/m	
1.1	1.009	1.008	0.0991
1.2	1.009	1.008	0.0991
1.4	1.008	1.008	0.0000
1.6	1.009	1.009	0.0000
1.7	1.008	1.008	0.0000
4.1	1.024	1.017	0.6836
4.2	1.017	1.013	0.3933
4.3	1.014	1.013	0.0986
7.1	1.009	1.009	0.0000
3.1	1.010	1.010	0.0000
3.2	1.008	1.008	0.0000
3.3	1.009	1.009	0.0000
3.4	1.009	1.009	0.0000
3.5	1.009	1.009	0.0000
3.6	1.009	1.009	0.0000
8.1	1.015	1.015	0.0000
8.2	1.010	1.009	0.0990
8.3	1.011	1.011	0.0000
19.2	1.014	1.014	0.0000
19.3	1.016	1.017	-0.0984
19.5	1.015	1.015	0.0000
22.1	1.014	1.014	0.0000
22.2	1.015	1.016	-0.0985
22.3	1.015	1.015	0.0000
25.2	1.022	1.017	0.4892
25.4	1.013	1.013	0.0000
25.5	1.021	1.016	0.4897
25.8	1.016	1.013	0.2953
34.1	1.021	1.020	0.0979
34.2	1.019	1.017	0.1963
34.4	1.018	1.017	0.0982
34.5	1.023	1.022	0.0978

Table AT4. Compilation AF demagnetization data from 23 samples used for NRM studies. 'N.A.' marks the skipped steps

Applied field [mT]	NRM field [A/m]																							
	1	4	6	8	10	11	12	13	14	16	18	19	20	21	25	26	27	28	29	30	31	33	34
0	8.152	2.343	4.384	3.404	2.743	2.804	1.801	3.014	4.126	1.775	2.642	5.125	2.688	4.113	1.432	5.475	6.302	2.391	8.636	6.367	10.310	5.564	3.379
2.5	8.153	2.216	N.A.	3.277	2.577	2.845	1.780	3.053	4.038	1.730	2.636	5.144	2.691	3.827	1.121	5.444	6.253	2.362	8.585	6.377	12.070	5.585	3.432
5	7.695	1.746	4.554	2.963	2.456	2.836	1.288	3.186	2.741	1.116	2.628	5.122	2.667	3.534	0.998	5.483	5.683	1.980	6.236	N.A.	7.625	5.565	N.A.
10	6.429	0.772	4.635	2.290	1.197	2.788	0.614	3.314	1.038	0.772	2.607	5.039	2.627	3.324	0.787	5.404	3.170	1.595	1.627	5.733	1.275	5.369	3.308
15	5.553	0.694	4.633	1.973	1.432	2.764	N.A.	3.273	0.423	0.484	2.499	4.877	2.529	3.073	0.594	5.246	2.684	1.395	0.684	5.386	0.535	5.107	3.162
25	3.693	0.432	3.951	1.810	0.884	2.487	0.427	3.032	0.115	0.238	2.143	4.287	2.277	2.302	0.386	4.613	2.071	1.079	0.266	4.578	0.181	4.296	2.660
35	2.506	0.286	3.043	1.423	0.605	2.124	0.343	2.417	0.147	0.139	1.806	3.585	1.909	1.773	0.257	3.880	1.431	0.770	0.174	3.629	0.045	3.448	1.872
50	1.508	0.167	1.980	0.940	0.388	1.665	0.269	1.919	0.177	0.091	1.396	2.532	1.492	1.289	0.142	2.693	0.862	0.417	0.126	2.423	0.024	2.340	0.962
70	0.936	0.095	1.233	0.442	0.260	1.227	0.209	1.218	0.175	0.076	1.081	1.510	1.114	1.029	0.084	1.583	0.461	0.177	0.082	1.456	0.019	1.426	0.319
90	0.558	0.075	0.880	0.085	0.192	0.958	0.172	0.713	N.A.	0.059	0.844	1.248	0.892	0.754	0.049	0.972	0.304	0.121	N.A.	0.875	0.020	0.829	0.169
110	0.421	0.053	0.672	0.088	0.131	0.803	0.151	0.469	0.151	0.052	0.712	0.804	0.755	0.649	0.053	0.667	0.230	0.087	0.058	0.597	0.027	0.779	N.A.
130	0.341	0.051	0.560	0.078	0.150	0.722	0.129	0.356	0.139	0.049	0.626	0.651	0.669	0.573	0.052	0.524	0.172	0.038	0.062	0.427	0.035	0.648	0.147
160	0.283	0.053	0.465	0.091	0.137	0.656	0.117	0.288	0.122	0.045	0.555	0.656	0.667	0.517	0.058	0.390	0.148	0.079	0.046	0.278	0.041	0.484	0.138

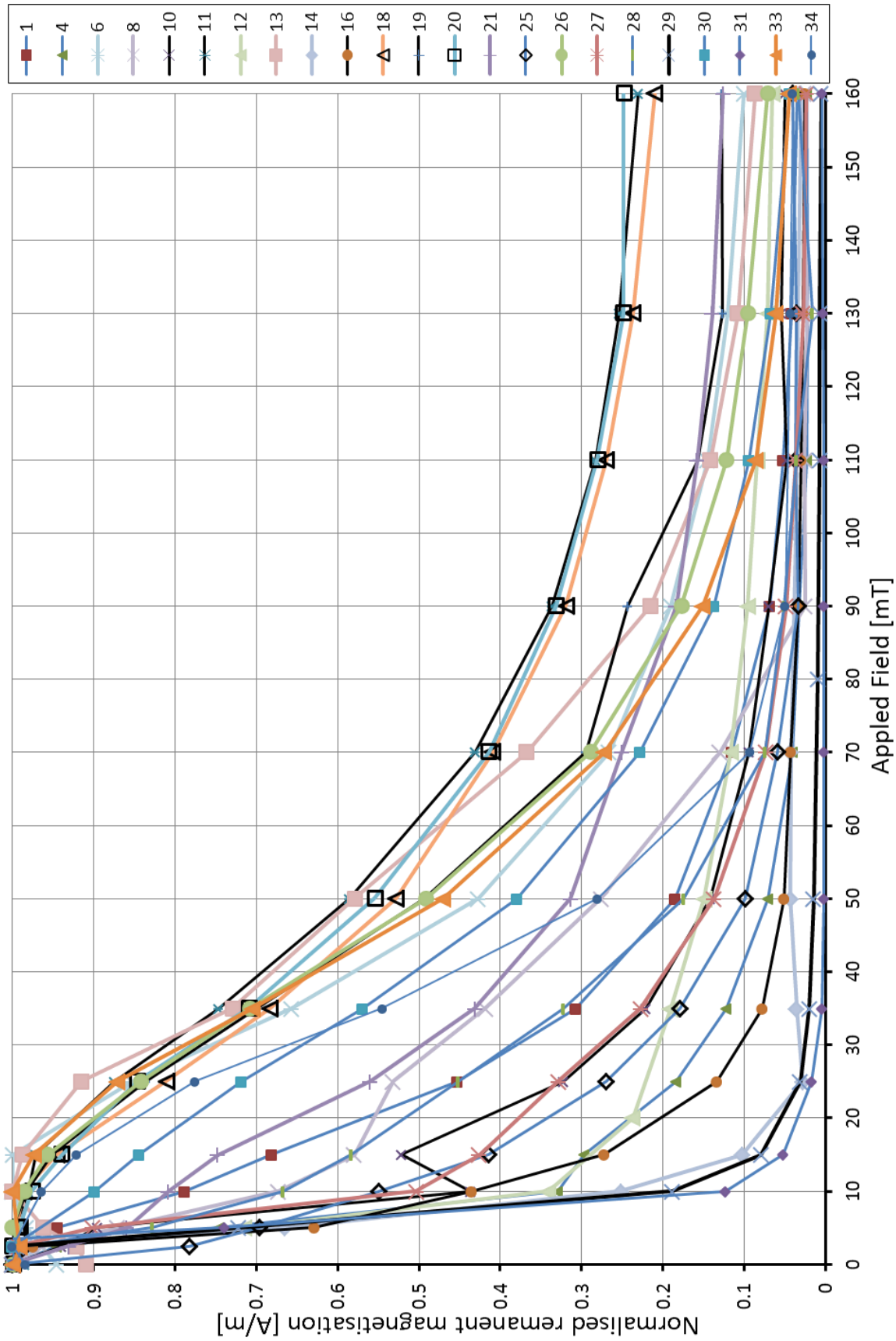

Figure AF3. Normalised remanent magnetisation versus applied field of samples

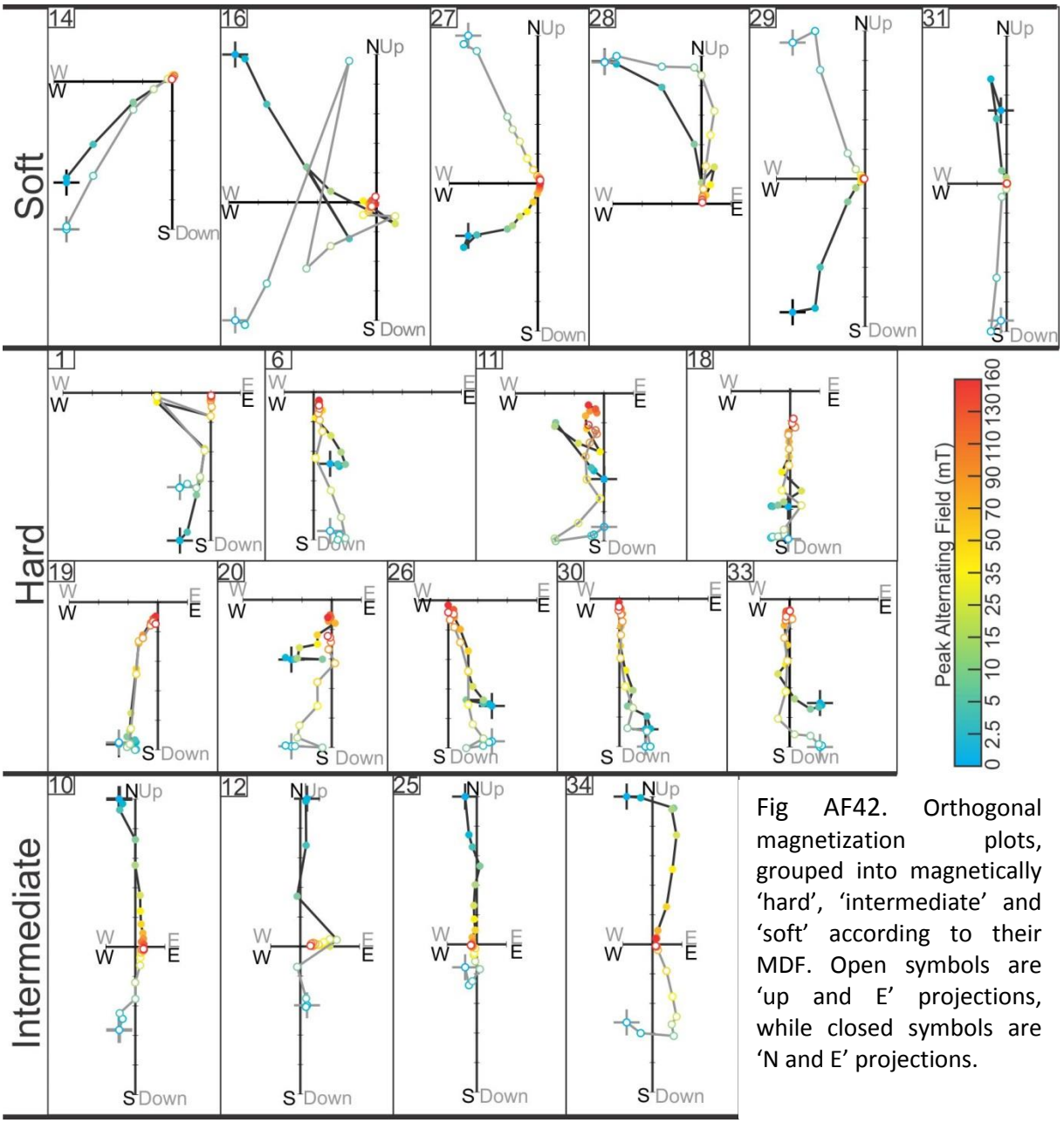

Fig AF42. Orthogonal magnetization plots, grouped into magnetically 'hard', 'intermediate' and 'soft' according to their MDF. Open symbols are 'up and E' projections, while closed symbols are 'N and E' projections.

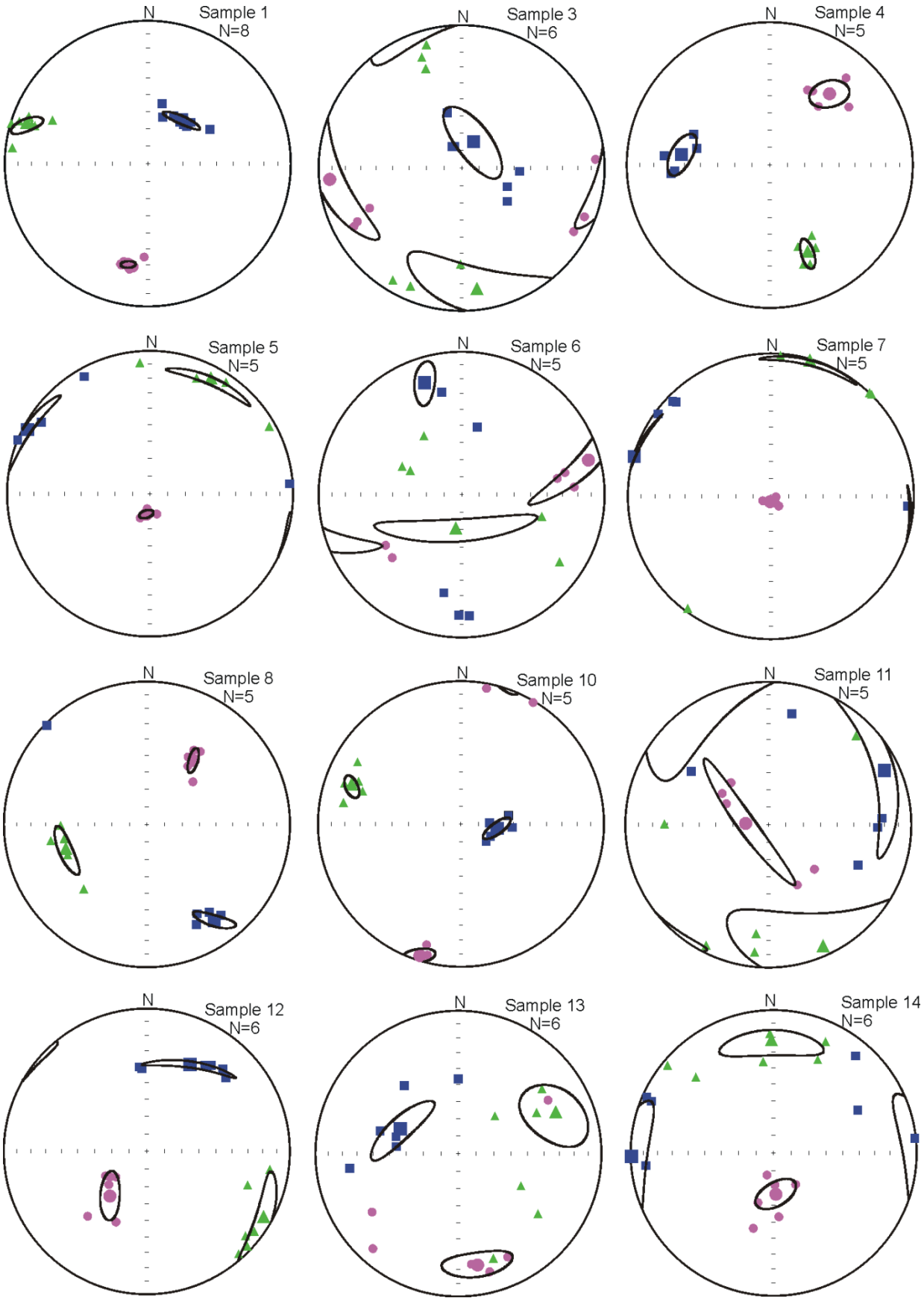
N
Sample 1
N=8
N
Sample 3
N=6
N
Sample 4
N=5
N
Sample 5
N=5
N
Sample 6
N=5
N
Sample 7
N=5
N
Sample 8
N=5
N
Sample 10
N=5
N
Sample 11
N=5
N
Sample 12
N=6
N
Sample 13
N=6
N
Sample 14
N=6

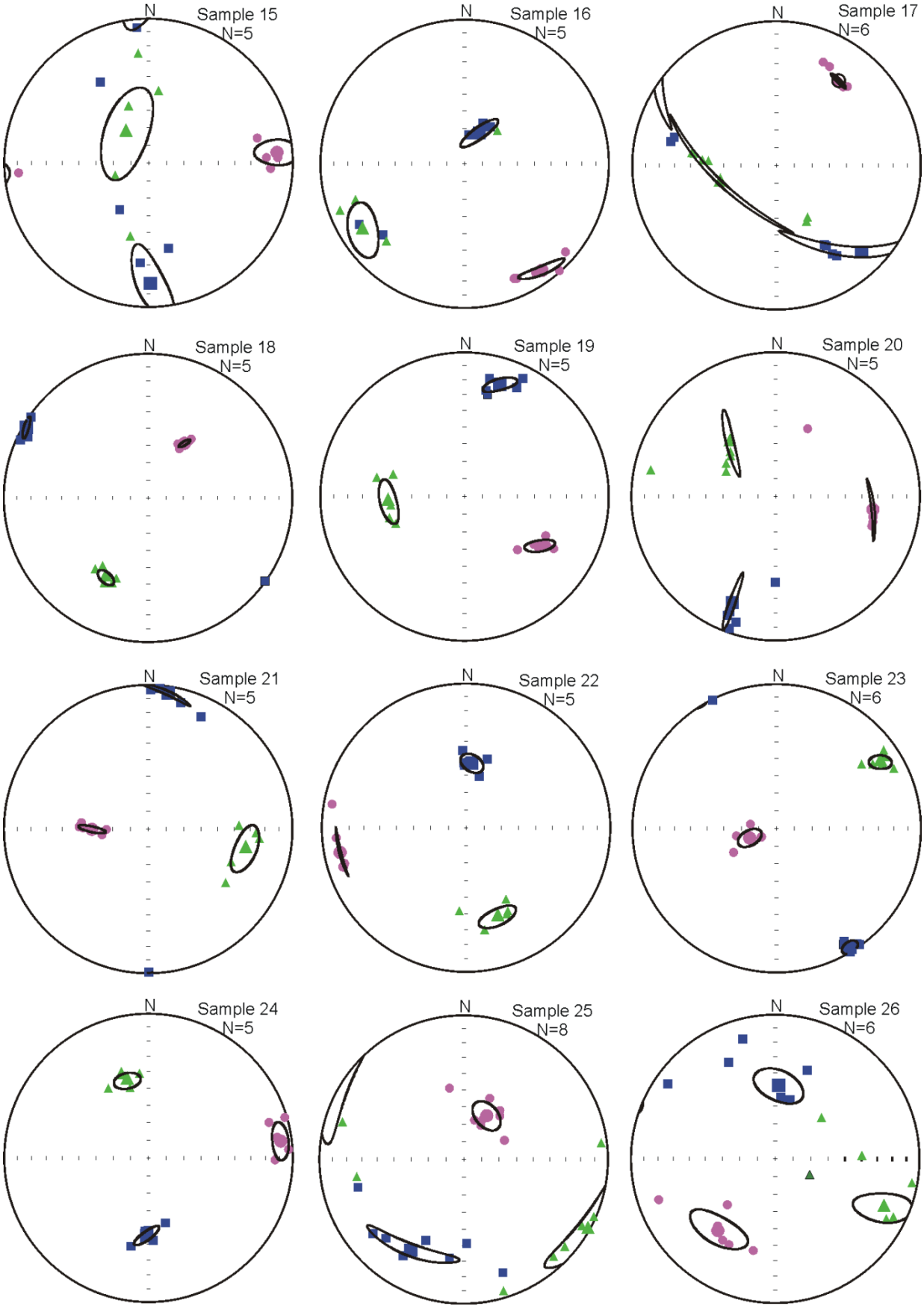
N
Sample 15
N=5
N
Sample 16
N=5
N
Sample 17
N=6
N
Sample 18
N=5
N
Sample 19
N=5
N
Sample 20
N=5
N
Sample 21
N=5
N
Sample 22
N=5
N
Sample 23
N=6
N
Sample 24
N=5
N
Sample 25
N=8
N
Sample 26
N=6

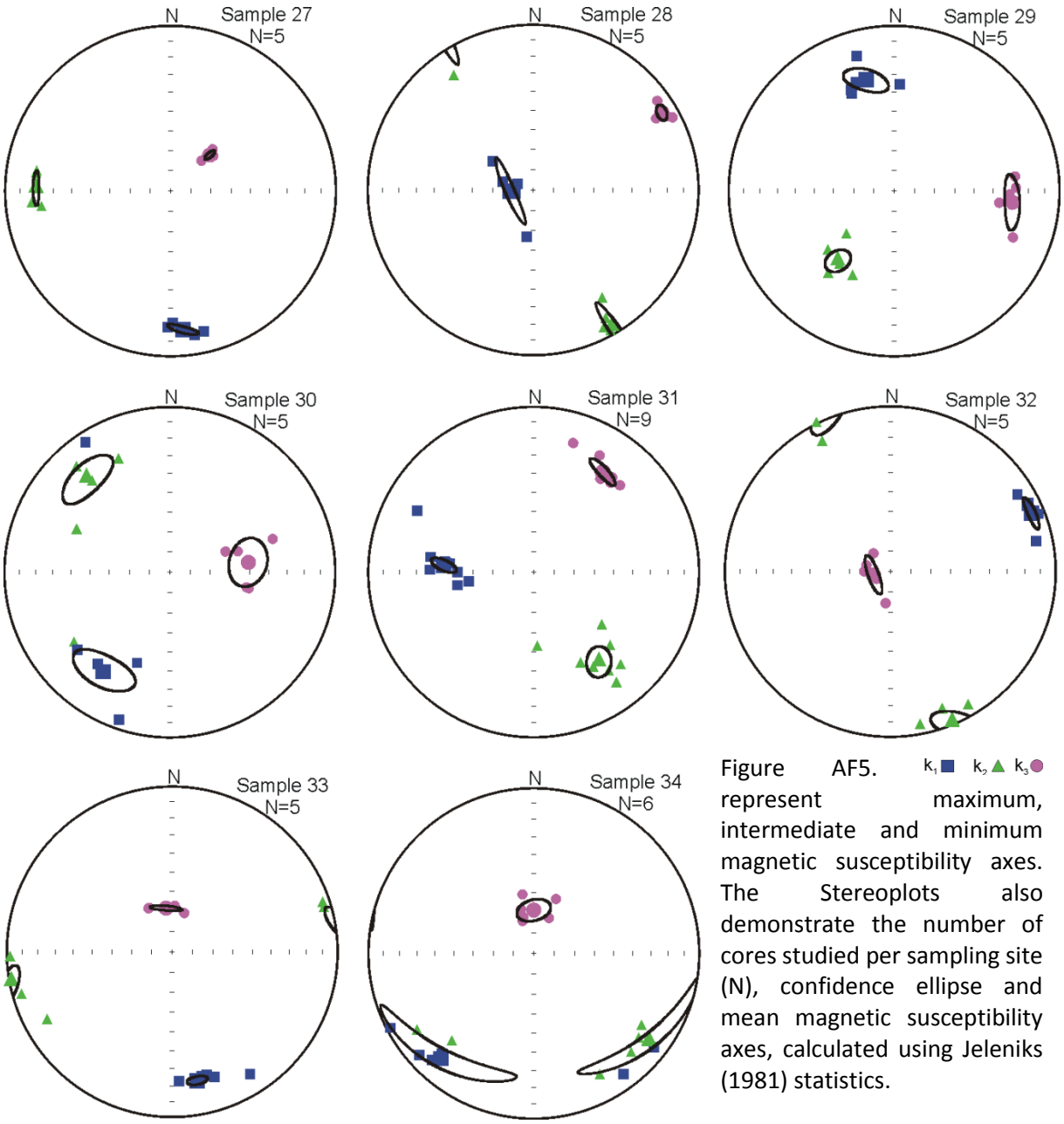

Figure AF5. k_1 ■ k_2 ▲ k_3 ● represent maximum, intermediate and minimum magnetic susceptibility axes. The Stereoplots also demonstrate the number of cores studied per sampling site (N), confidence ellipse and mean magnetic susceptibility axes, calculated using Jeleniks (1981) statistics.

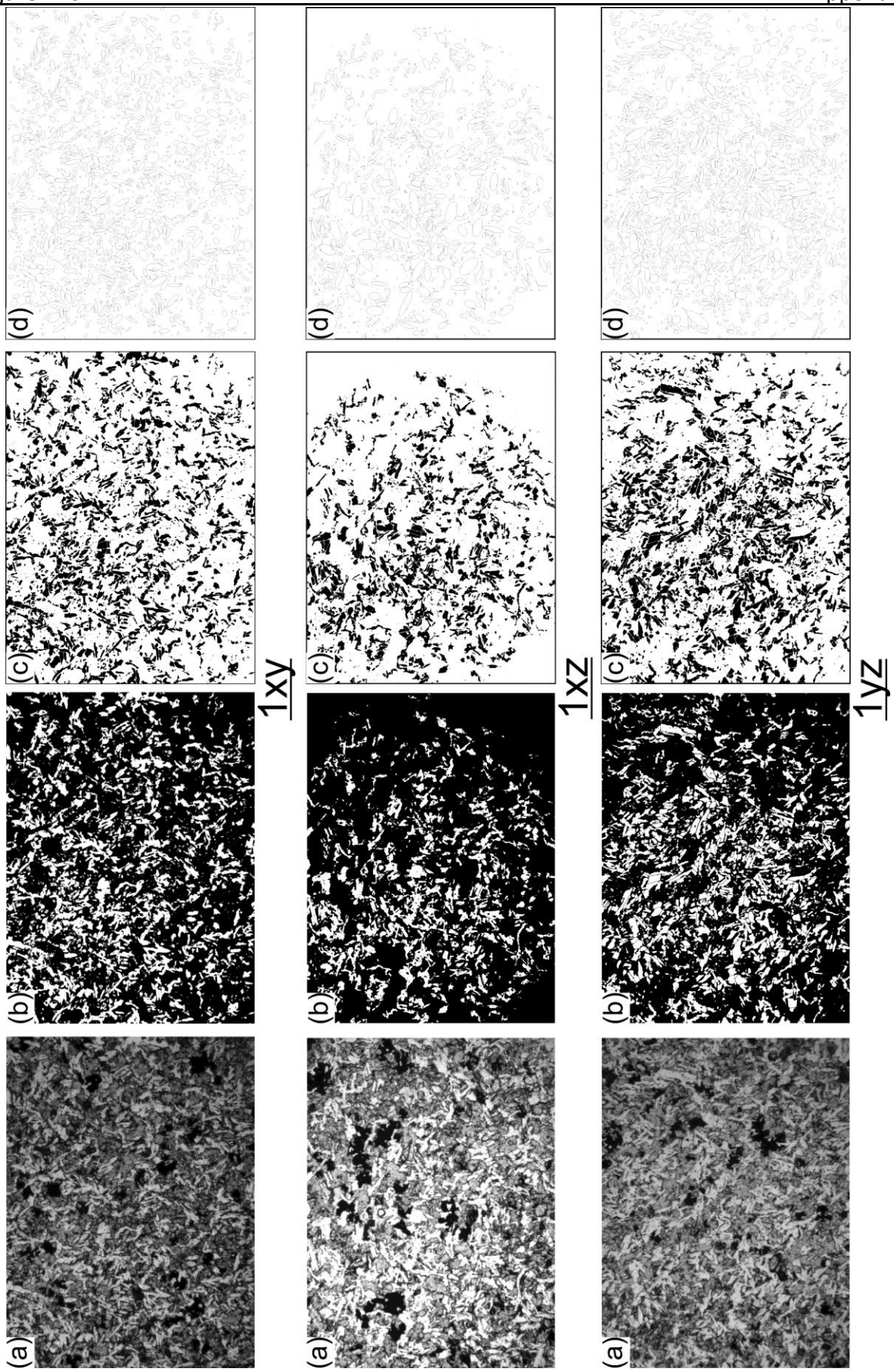
(a)
(b)
(c)
(d)
1xy
1xz
1yz

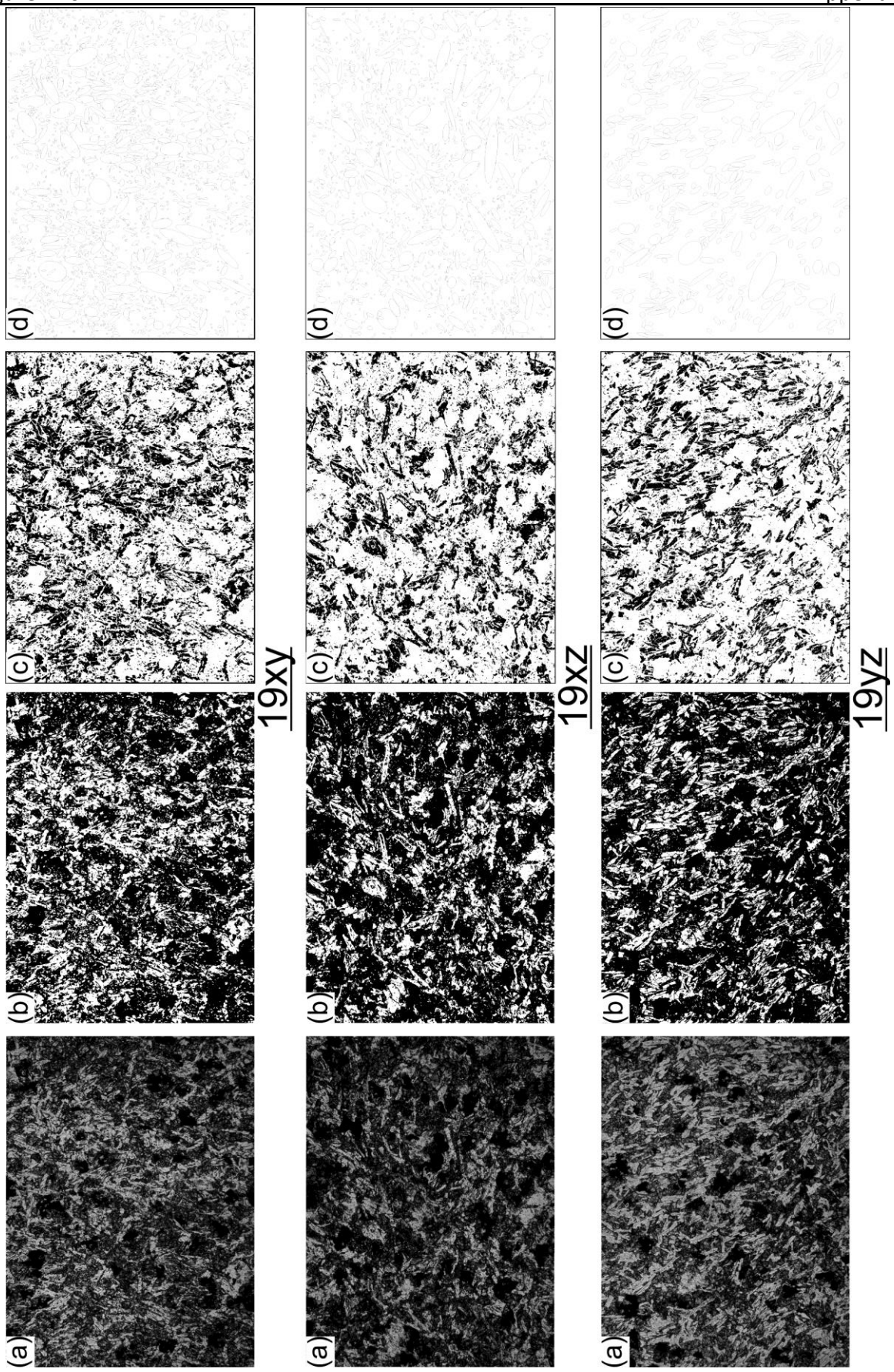
(d)
(c)
(b)
(a)
19xy
(d)
(c)
(b)
(a)
19xz
(d)
(c)
(b)
(a)
19yz

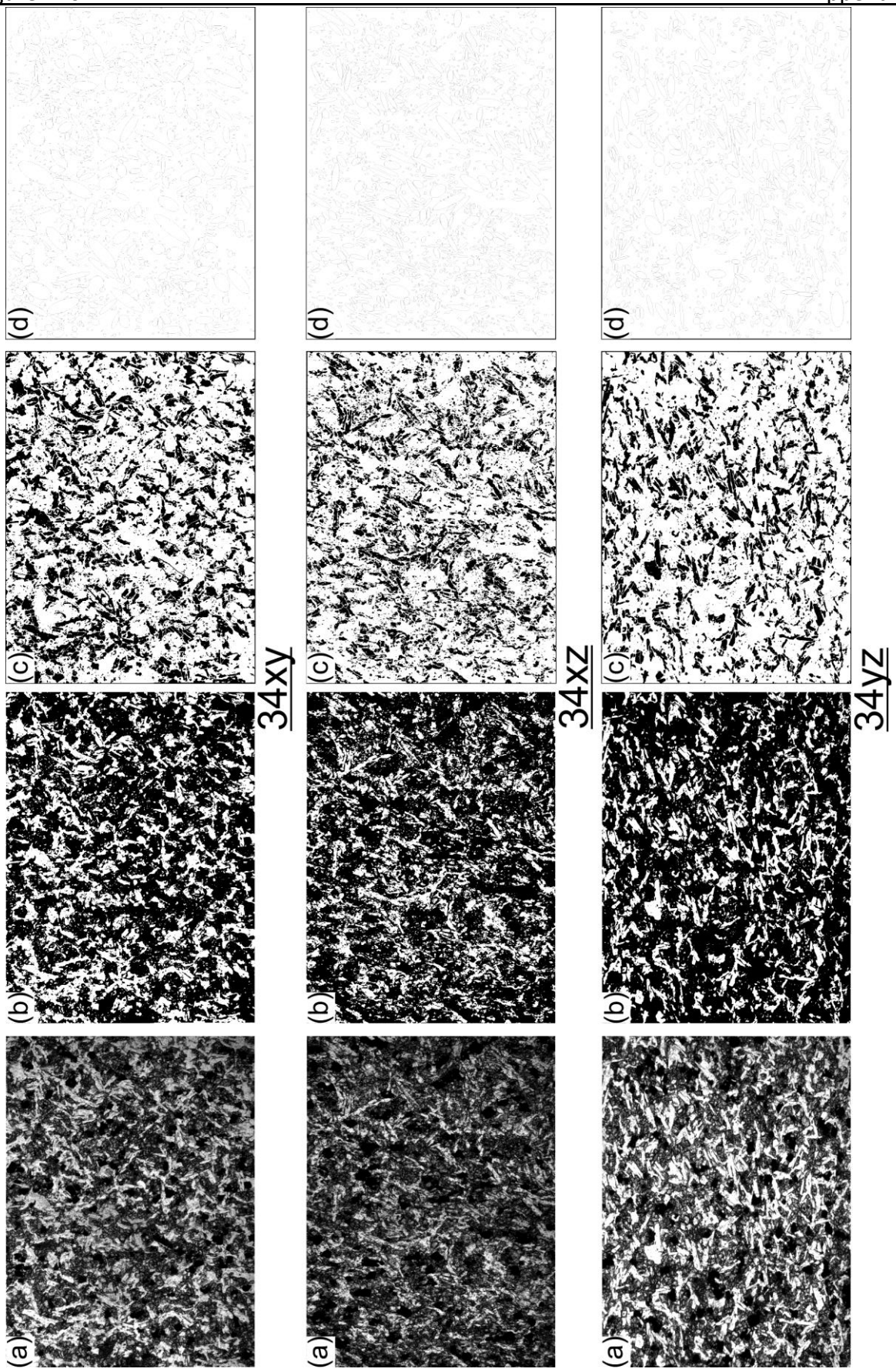
(a)
(b)
(c)
(d)
34xy
34xz
34yz

Figure AF6. Steps of magmatic fabric analysis from the thin sections. (a) Grayscale photomicrograph from a monochromatic camera. (b) The image is thresholded into b/w such that the plagioclase grains in white, contrast against black background of mafic minerals. (c) The image is smoothened to get rid of smaller grains, holes, etc. The image is then inverted. (d) ImageJ is used to fit ellipse in all the grains. The size and orientation of each ellipse is recorded and a mean is calculated, which is shown in table below.

Table AT5. Example results of "particle analysis" through ImageJ. "Count" represents the number of particles analysed. Sum of the area covered by the analysed grains is represented by "total area". "Average size" represents the average size of the ellipse. The mean length of the major and minor axis and the mean angle of the major axis from the vertical are represented by "major", "minor" and "angle", respectively. The lengths and angles are represented in pixels and degree, respectively.

Name	Count	Total area	Average Size	Major	Minor	Angle
1xy	1847	1120482	606.65	33.907	14.831	88.7739
1xz	1372	900078	656.034	31.643	13.913	89.61438
1yz	2048	1306826	638.099	32.166	14.079	83.40501
19xy	1861	3243466	1742.862	50.524	23.777	88.53305
19xz	1558	3453707	2216.757	55.357	24.656	92.3273
19yz	430	3261968	7585.972	151.21	54.31	70.60914
34xy	1421	4493500	3162.21	67.744	31.341	92.94352
34xz	1935	3673740	1898.574	59.445	25.427	92.82832
34yz	1250	2964818	2371.854	71.085	29.524	91.76981

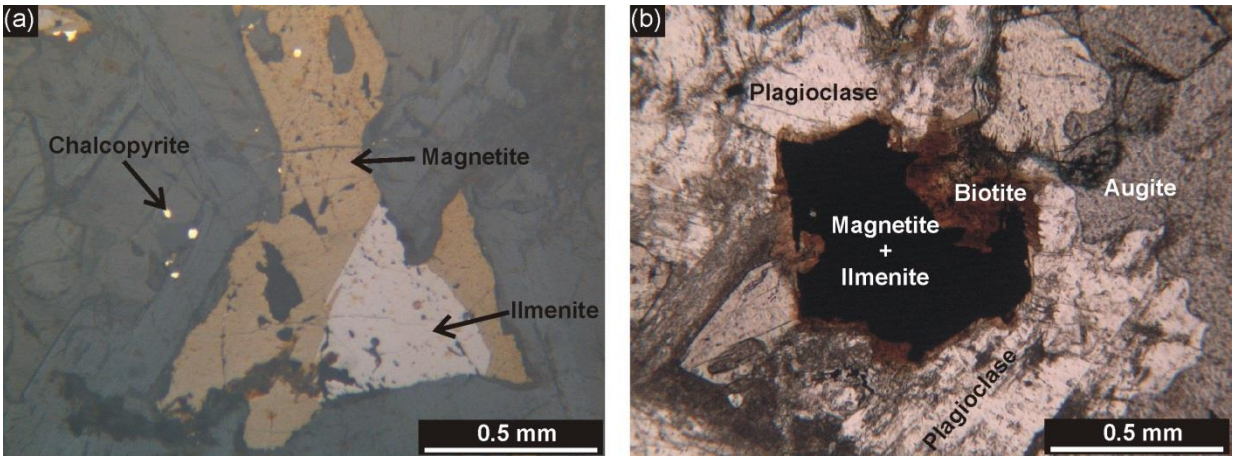

Figure AF7. (a) Reflected light photomicrograph of a dolerite thin-section covered with the ferro-fluid, demonstrating intergrown magnetite and ilmenite. Minor chalcopyrite are also present. (b) Plane polarized transmitted light photomicrograph showing intergrowth of biotite, magnetite and ilmenite surrounded by plagioclase and augite.

Table AT6. AMS data, representing mean of values from cores (n) collected from each site (sample no.) in crystalline basement rocks at Lockne Impact structure. , k_1d, k_2d and k_3d are the declination; k_1i, k_2i and k_3i are the inclination and k_1, k_2 and k_3 are the intensities of maximum (k_1), intermediate (k_2) and minimum (k_3) susceptibility axes of AMS ellipsoid. k_m= mean susceptibility. P'=corrected degree of magnetic anisotropy. T_{mean}= shape parameter. $k_m = (k_1+k_2+k_3)/3$; $P' = \exp \sqrt{[2(\eta_1-\eta_m)^2+(\eta_2-\eta_m)^2+(\eta_3-\eta_m)^2]}$; $T_{mean} = (2\eta_2-\eta_1-\eta_3)/(\eta_1-\eta_3)$;Here $\eta_1=\ln k_1$; $\eta_2=\ln k_2$; $\eta_3=\ln k_3$ and $\eta_m=(\eta 1.\ \eta 2.\ \eta 3)^{1/3}$ k_2 [127].

Sample No	k_m (10^{-3} SI)	k_1	k_2	k_3	k_1d	k_1i	k_2d	k_2i	k_3d	k_3i	P`	T
1.1	0.226	1.010	1.007	0.984	239	13	334	21	119	65	1.029	0.75
1.3	0.225	1.012	1.010	0.979	230	8	321	3	69	81	1.038	0.91
1.4	0.209	1.011	1.007	0.982	267	19	3	17	132	64	1.031	0.70
1.6	0.218	1.012	1.010	0.978	231	8	323	14	111	74	1.040	0.91
1.7	0.209	1.012	1.009	0.979	232	7	323	4	84	82	1.038	0.82
1.8	0.257	1.011	1.006	0.983	256	21	355	22	127	59	1.030	0.61
2.1	8.864	1.030	1.003	0.967	47	36	300	22	185	46	1.066	0.15
2.2	8.152	1.025	1.007	0.968	63	15	326	26	180	59	1.060	0.37
2.4	7.578	1.031	1.006	0.963	50	33	302	25	183	46	1.072	0.27
2.5	7.896	1.023	1.004	0.972	66	20	324	30	184	53	1.053	0.27
2.6	6.804	1.027	1.008	0.965	51	29	309	21	188	53	1.066	0.40
2.8	6.241	1.027	1.006	0.967	73	13	336	28	185	59	1.063	0.30
3.1	5.173	1.036	1.015	0.950	302	31	123	59	32	1	1.095	0.53
3.2	6.572	1.035	1.015	0.950	294	11	109	79	204	1	1.094	0.56
3.3	8.102	1.039	1.017	0.945	297	20	115	70	207	1	1.104	0.55
3.4	7.150	1.041	1.016	0.944	292	19	115	71	22	1	1.108	0.50
3.5	5.113	1.039	1.022	0.939	294	24	115	66	24	0	1.115	0.68
4A	2.536	1.049	1.014	0.937	293	34	74	49	189	20	1.122	0.39
4B	2.537	1.052	1.017	0.932	296	30	74	52	194	21	1.133	0.45
4C	2.509	1.046	1.020	0.934	292	23	62	57	192	22	1.126	0.55
4D	2.667	1.047	1.017	0.936	289	18	57	62	192	21	1.123	0.47
4E	2.701	1.050	1.018	0.932	292	26	65	54	190	22	1.131	0.47
4F	2.697	1.051	1.016	0.933	296	37	78	46	191	20	1.130	0.44
4G	2.680	1.053	1.017	0.929	292	20	58	58	192	24	1.138	0.44
5.1	0.166	1.014	0.999	0.987	40	27	146	30	276	48	1.027	-0.09
5.2	0.154	1.020	0.995	0.984	49	23	153	29	288	52	1.037	-0.38
5.3	0.149	1.015	0.998	0.987	41	23	144	29	279	52	1.029	-0.20
5.4	0.157	1.013	0.998	0.989	41	32	144	20	260	51	1.024	-0.19
5.5	0.200	1.012	0.998	0.990	38	28	144	28	271	48	1.023	-0.21
5.7	0.211	1.012	0.997	0.992	34	28	150	39	279	39	1.021	-0.51
6.1	0.870	1.021	1.000	0.980	97	42	321	39	210	23	1.042	0.01
6.2	0.827	1.025	0.998	0.977	101	52	324	30	221	22	1.050	-0.11
6.3	0.924	1.028	1.007	0.965	103	32	267	57	8	8	1.067	0.34
6.4	0.851	1.038	1.000	0.962	106	49	321	36	218	18	1.079	0.01
6.5	0.857	1.037	0.996	0.967	101	49	324	32	219	22	1.072	-0.17
6.6	0.770	1.023	0.999	0.979	95	45	323	33	214	26	1.045	-0.06
7.1	0.774	1.001	1.001	0.998	253	55	77	35	345	2	1.003	0.57
7.2	48.300	1.197	0.973	0.830	59	65	323	3	232	25	1.443	-0.13
7.3	33.820	1.189	0.977	0.834	77	66	337	5	245	24	1.426	-0.11
7.4	44.000	1.176	0.977	0.847	89	62	348	6	255	28	1.389	-0.13
7.5	30.910	1.196	0.969	0.834	61	68	159	3	250	21	1.436	-0.17
8.1	7.055	1.029	0.997	0.974	299	4	31	23	199	67	1.056	-0.14
8.2	6.559	1.028	0.996	0.977	117	3	26	18	216	72	1.053	-0.24
8.3	7.754	1.026	1.002	0.972	288	2	19	25	193	65	1.056	0.13
8.4	6.766	1.033	1.001	0.966	109	2	18	18	204	72	1.070	0.06

8.5	6.780	1.031	1.002	0.967	285	5	17	22	184	67	1.066	0.12
9.1	6.915	1.022	1.002	0.976	256	3	348	33	162	57	1.048	0.11
9.2	7.735	1.021	1.004	0.975	258	4	352	38	163	51	1.048	0.24
9.3	6.728	1.020	1.007	0.973	76	1	346	32	168	58	1.051	0.47
9.6	7.131	1.016	1.012	0.971	266	3	358	38	172	52	1.051	0.82
9.7	7.379	1.025	1.003	0.973	259	6	353	32	160	57	1.054	0.17
9.8	6.887	1.020	1.009	0.971	77	6	344	25	180	64	1.053	0.55
10A	11.620	1.015	0.999	0.987	141	4	233	20	39	70	1.028	-0.14
10B	11.140	1.014	1.001	0.985	312	8	222	1	124	82	1.029	0.08
10C	10.920	1.017	0.998	0.985	129	2	220	27	35	63	1.033	-0.15
10D	12.170	1.011	1.010	0.980	185	20	279	9	31	68	1.036	0.94
10E	10.670	1.020	0.995	0.985	319	4	225	43	53	47	1.037	-0.42
10F	11.250	1.010	0.998	0.992	320	5	51	9	201	79	1.019	-0.35
10G	11.080	1.014	1.004	0.983	294	20	198	17	70	64	1.032	0.36
11A	4.546	1.018	0.998	0.985	194	27	289	10	37	61	1.034	-0.20
11B	9.951	1.016	1.004	0.980	249	8	159	6	32	80	1.037	0.31
11C	0.814	1.005	1.000	0.995	218	33	319	18	73	52	1.010	0.02
11D	0.771	1.012	0.996	0.993	112	3	204	43	19	47	1.021	-0.70
11E	0.758	1.005	1.003	0.992	144	39	240	8	340	50	1.014	0.65
11F	0.876	1.011	1.000	0.989	16	8	283	20	127	68	1.022	0.02
12A	9.235	1.022	0.998	0.980	336	22	239	16	116	62	1.043	-0.10
12B	10.090	1.023	1.001	0.976	343	20	253	2	157	70	1.048	0.06
12C	9.177	1.022	1.000	0.978	354	29	257	13	146	58	1.045	0.01
12D	10.880	1.023	0.998	0.979	339	15	246	11	121	71	1.045	-0.13
12E	10.380	1.018	1.000	0.982	351	11	259	9	131	75	1.037	0.00
12F	10.120	1.021	1.001	0.979	337	23	243	9	132	65	1.043	0.07
13B	15.910	1.020	1.003	0.978	312	15	219	9	98	72	1.044	0.20
13C	15.440	1.019	1.006	0.976	274	18	7	9	122	70	1.045	0.39
13D	15.920	1.018	1.001	0.981	282	13	188	18	46	68	1.037	0.12
13E	16.070	1.018	1.003	0.980	308	20	214	10	98	68	1.039	0.21
13F	16.160	1.018	1.001	0.981	21	8	289	18	135	70	1.039	0.09
14.1	0.241	1.034	1.000	0.966	60	74	298	8	206	13	1.071	0.02
14.2	0.252	1.031	0.997	0.972	360	70	123	11	217	16	1.061	-0.16
14.3	0.165	1.026	1.008	0.967	304	73	104	16	195	5	1.062	0.40
14.4	0.309	1.034	0.992	0.974	22	72	122	3	213	18	1.064	-0.37
14.5	0.293	1.033	0.998	0.969	23	65	139	11	234	22	1.066	-0.09
14.6	0.245	1.027	1.004	0.969	25	72	124	3	215	18	1.060	0.21
15A	0.169	1.050	0.979	0.972	30	25	285	29	155	50	1.089	-0.81
15B	0.161	1.050	1.025	0.925	17	7	136	75	285	13	1.145	0.61
15C	0.168	1.053	0.987	0.961	28	20	283	35	141	48	1.098	-0.42
15D	0.064	1.033	1.016	0.952	23	38	191	51	288	6	1.090	0.59
15E	0.188	1.043	0.987	0.970	31	20	134	32	275	51	1.079	-0.54
15F	0.153	1.061	1.010	0.930	33	47	162	31	269	27	1.143	0.25
15G	0.139	1.050	0.994	0.957	23	23	185	66	290	6	1.098	-0.18
15H	0.166	1.054	0.988	0.958	26	30	160	50	282	24	1.102	-0.34
16.1	10.860	1.079	1.059	0.862	154	11	297	76	62	8	1.283	0.83
16.2	12.110	1.093	1.041	0.866	339	6	86	69	247	20	1.279	0.58
16.3	9.299	1.091	1.021	0.888	292	28	136	60	27	11	1.234	0.35
17.1	23.330	1.017	0.997	0.986	276	34	177	13	68	53	1.031	-0.31
17.2	25.470	1.010	1.008	0.983	321	2	229	44	53	46	1.031	0.89
17.3	25.040	1.016	1.000	0.984	304	19	200	36	57	48	1.032	-0.02
17.4	21.720	1.016	0.995	0.989	257	33	164	4	68	57	1.029	-0.50
17.5	23.380	1.018	0.998	0.984	274	31	176	13	67	56	1.035	-0.13
17.6	25.290	1.009	1.004	0.986	321	5	228	33	58	57	1.025	0.58
18.1	12.880	1.013	1.003	0.984	182	12	275	13	52	72	1.030	0.36
18.2	11.380	1.011	1.006	0.984	174	3	265	30	79	60	1.030	0.62

18.3	13.040	1.015	1.007	0.979	189	26	287	18	48	58	1.039	0.56
18.4	12.910	1.014	1.004	0.983	344	4	252	26	81	63	1.032	0.39
18.5	11.340	1.011	1.005	0.984	331	0	241	19	62	71	1.028	0.53
18.6	13.690	1.010	1.004	0.986	168	2	259	36	76	54	1.026	0.50
18.7	12.780	1.015	1.005	0.980	323	12	228	26	76	0	1.037	0.40
19.1	1.236	1.005	1.004	0.991	86	47	210	27	317	30	1.015	0.83
19.2	1.170	1.010	1.000	0.990	346	19	99	48	242	36	1.020	0.04
19.3	1.059	1.010	1.008	0.982	164	33	255	1	346	57	1.032	0.84
19.4	1.019	1.015	0.998	0.987	198	7	105	22	305	66	1.028	-0.19
19.5	0.941	1.010	1.002	0.988	222	29	111	32	344	44	1.022	0.30
20.1	16.230	1.018	1.009	0.973	264	37	174	0	83	53	1.049	0.59
20.2	17.170	1.023	1.002	0.976	272	39	170	15	64	47	1.048	0.12
20.3	15.620	1.020	1.002	0.978	283	34	181	17	69	51	1.043	0.19
20.4	14.850	1.025	0.993	0.981	238	46	329	1	59	44	1.046	-0.46
20.5	15.170	1.027	0.999	0.974	285	40	170	27	57	38	1.055	-0.02
20.6	12.930	1.027	0.998	0.975	305	27	194	35	63	43	1.053	-0.11
21.1	29.970	1.022	0.999	0.979	279	14	187	7	72	75	1.044	-0.09
21.2	32.730	1.026	1.005	0.969	265	10	356	9	127	77	1.059	0.26
21.3	26.730	1.029	1.007	0.964	246	9	337	2	78	80	1.068	0.34
21.4	27.040	1.032	0.995	0.974	274	9	5	3	115	80	1.061	-0.26
21.5	33.190	1.025	1.005	0.970	286	9	195	4	80	80	1.058	0.29
21.6	34.910	1.026	1.005	0.969	289	13	19	1	115	76	1.059	0.29
21.7	31.880	1.022	0.998	0.980	267	9	359	13	144	74	1.043	-0.12
21.8	25.960	1.029	1.006	0.965	284	2	194	7	28	83	1.067	0.29
22A	19.000	1.005	1.003	0.992	341	25	243	17	122	59	1.014	0.64
22B	19.060	1.006	1.002	0.993	344	24	248	14	130	61	1.013	0.35
22C	19.320	1.005	1.000	0.995	346	30	254	4	157	60	1.010	0.07
22D	18.660	1.006	1.002	0.992	356	14	261	17	123	67	1.015	0.36
22E	18.040	1.009	0.999	0.992	338	34	236	17	124	52	1.017	-0.16
23.1	49.710	1.025	0.990	0.985	145	4	235	13	39	76	1.044	-0.71
23.2	42.220	1.026	1.001	0.973	142	4	51	6	264	83	1.055	0.08
23.3	45.060	1.025	1.008	0.967	328	2	58	6	220	84	1.061	0.41
23.4	49.800	1.023	0.997	0.980	318	0	48	9	227	81	1.044	-0.19
23.5	47.300	1.022	0.995	0.983	326	5	56	6	196	83	1.040	-0.41
23.6	41.010	1.026	0.990	0.984	327	6	61	33	228	56	1.046	-0.74
23.7	45.820	1.029	0.997	0.974	140	1	50	13	233	77	1.056	-0.13
23.8	37.420	1.022	1.001	0.976	327	5	57	7	198	81	1.047	0.11
24.1	17.930	1.008	1.007	0.985	270	27	153	42	22	36	1.026	0.85
24.2	18.590	1.014	1.001	0.985	107	10	204	32	2	56	1.030	0.10
24.3	16.630	1.015	0.997	0.988	147	14	55	9	293	73	1.029	-0.33
24.4	17.080	1.014	1.004	0.982	101	23	191	1	283	67	1.034	0.38
24.5	17.240	1.017	0.997	0.986	134	2	225	24	40	66	1.032	-0.24
24.6	17.230	1.015	0.998	0.987	125	3	216	5	1	84	1.029	-0.20
25.1	0.088	1.010	0.998	0.992	298	9	134	81	28	3	1.018	-0.27
25.2	0.103	1.006	0.999	0.995	292	2	27	72	202	18	1.010	-0.25
25.3	0.087	1.007	0.998	0.995	286	14	18	10	142	73	1.012	-0.52
25.4	0.112	1.006	0.999	0.995	303	12	35	10	166	74	1.012	-0.25
25.5	0.124	1.007	0.999	0.994	292	7	25	30	190	59	1.012	-0.21
25.6	0.101	1.007	0.999	0.994	283	6	18	40	186	49	1.014	-0.28
25.7	0.093	1.007	0.999	0.994	302	14	46	42	198	45	1.013	-0.30
26.1	0.024	1.036	1.032	0.931	321	63	157	27	64	6	1.129	0.93
26.2	0.040	1.051	1.047	0.902	204	74	335	10	67	12	1.191	0.95
26.3	0.054	1.040	1.035	0.925	180	61	331	26	67	12	1.141	0.92
26.4	0.055	1.044	1.040	0.916	173	66	328	22	62	9	1.161	0.95
26.5	0.036	1.044	1.038	0.919	183	76	334	12	65	7	1.155	0.90
26.6	0.056	1.043	1.039	0.918	170	67	333	22	65	6	1.156	0.95

27.1	0.613	1.036	0.992	0.973	313	65	155	23	61	8	1.066	-0.37
27.2	0.708	1.042	1.001	0.957	332	57	161	33	68	4	1.089	0.06
27.3	0.663	1.043	0.993	0.964	309	67	183	14	89	18	1.083	-0.26
27.4	0.630	1.038	0.995	0.967	320	65	168	22	74	10	1.073	-0.20
27.5	0.658	1.041	0.995	0.964	312	67	183	15	89	17	1.081	-0.18
27.6	0.654	1.042	1.004	0.954	328	61	182	25	86	14	1.093	0.16
28A	0.102	1.016	1.001	0.983	267	9	176	5	60	80	1.035	0.12
28C	0.173	1.010	1.009	0.981	55	6	324	12	172	76	1.035	0.93
28D	0.115	1.033	1.017	0.950	239	5	335	49	145	40	1.093	0.63
28E	0.124	1.011	1.005	0.984	238	0	328	1	112	89	1.030	0.56
28F	0.125	1.016	0.998	0.986	60	3	329	15	163	75	1.031	-0.17
28G	0.174	1.007	1.001	0.992	125	6	34	8	251	80	1.016	0.23
28H	0.171	1.009	1.007	0.985	243	1	334	19	151	71	1.027	0.80
29.1	0.000	1.002	0.999	0.999	310	8	45	36	209	53	1.004	-0.79
29.2	0.000	1.002	1.000	0.999	34	0	124	57	303	33	1.003	-0.15
29.3	0.000	1.004	1.000	0.996	132	4	37	53	226	37	1.008	0.11
29.4	0.000	1.002	1.001	0.998	235	3	327	45	142	45	1.004	0.40
29.5	0.000	1.003	0.999	0.998	265	14	38	71	172	14	1.005	-0.48
29.6	0.000	1.002	1.001	0.997	220	19	322	30	103	53	1.006	0.63
30A	0.176	1.071	0.998	0.931	177	39	84	3	351	51	1.150	-0.01
30B	0.184	1.070	1.018	0.912	167	44	76	1	345	46	1.178	0.38
30C	0.201	1.070	1.009	0.921	168	41	258	0	348	49	1.163	0.22
30D	0.190	1.073	0.999	0.928	185	39	91	5	356	51	1.156	0.02
30E	0.185	1.072	0.997	0.931	180	39	88	3	354	51	1.151	-0.03
30F	0.196	1.072	1.007	0.921	170	42	77	4	343	48	1.164	0.18
30G	0.178	1.071	1.013	0.916	166	44	75	1	344	46	1.172	0.29
30H	0.172	1.067	1.006	0.927	181	40	88	3	354	50	1.151	0.16
31.1	19.920	1.005	1.003	0.993	304	8	34	0	126	82	1.012	1.013
31.2	21.720	1.005	1.003	0.992	289	8	20	9	159	78	1.013	1.014
31.3	18.490	1.003	1.002	0.995	342	6	72	0	162	84	1.009	1.010
31.4	22.750	1.005	0.998	0.997	321	4	53	19	219	70	1.008	1.009
31.5	25.760	1.006	1.000	0.993	312	7	221	9	79	79	1.013	1.013
31.6	25.140	1.006	1.001	0.993	306	5	216	6	80	82	1.013	1.013
31.7	17.500	1.003	0.999	0.998	160	5	67	26	259	63	1.005	1.005
32.1	11.850	1.027	1.017	0.956	8	28	102	6	204	61	1.075	1.082
32.2	16.510	1.026	0.997	0.977	316	26	68	38	200	41	1.050	1.051
32.3	13.220	1.017	1.007	0.976	321	18	62	31	205	53	1.043	1.045
32.4	2.353	1.033	1.010	0.957	73	18	328	38	183	47	1.080	1.082
32.5	9.324	1.039	0.985	0.976	348	9	140	80	258	5	1.065	1.070
32.6	14.280	1.022	1.007	0.971	351	45	95	13	197	42	1.053	1.055
32.7	3.344	1.026	0.997	0.977	303	37	101	51	205	11	1.050	1.050
32.8	13.810	1.026	1.002	0.972	148	11	353	77	239	5	1.055	1.055
32.9	14.500	1.022	0.997	0.981	332	42	113	41	223	20	1.042	1.042
33.1	12.180	1.028	0.995	0.977	278	21	12	9	124	67	1.052	1.053
33.2	21.310	1.030	0.999	0.971	271	30	166	25	44	49	1.061	1.061
33.3	17.470	1.028	0.994	0.978	264	36	169	7	70	53	1.051	1.052
33.4	13.970	1.028	0.988	0.984	272	28	115	60	7	10	1.044	1.049
33.5	13.540	1.031	1.001	0.968	253	24	354	24	124	55	1.065	1.065
33.6	17.850	1.027	0.995	0.979	261	23	355	10	107	65	1.049	1.050
33.8	11.410	1.024	1.003	0.973	285	6	192	25	28	65	1.052	1.052

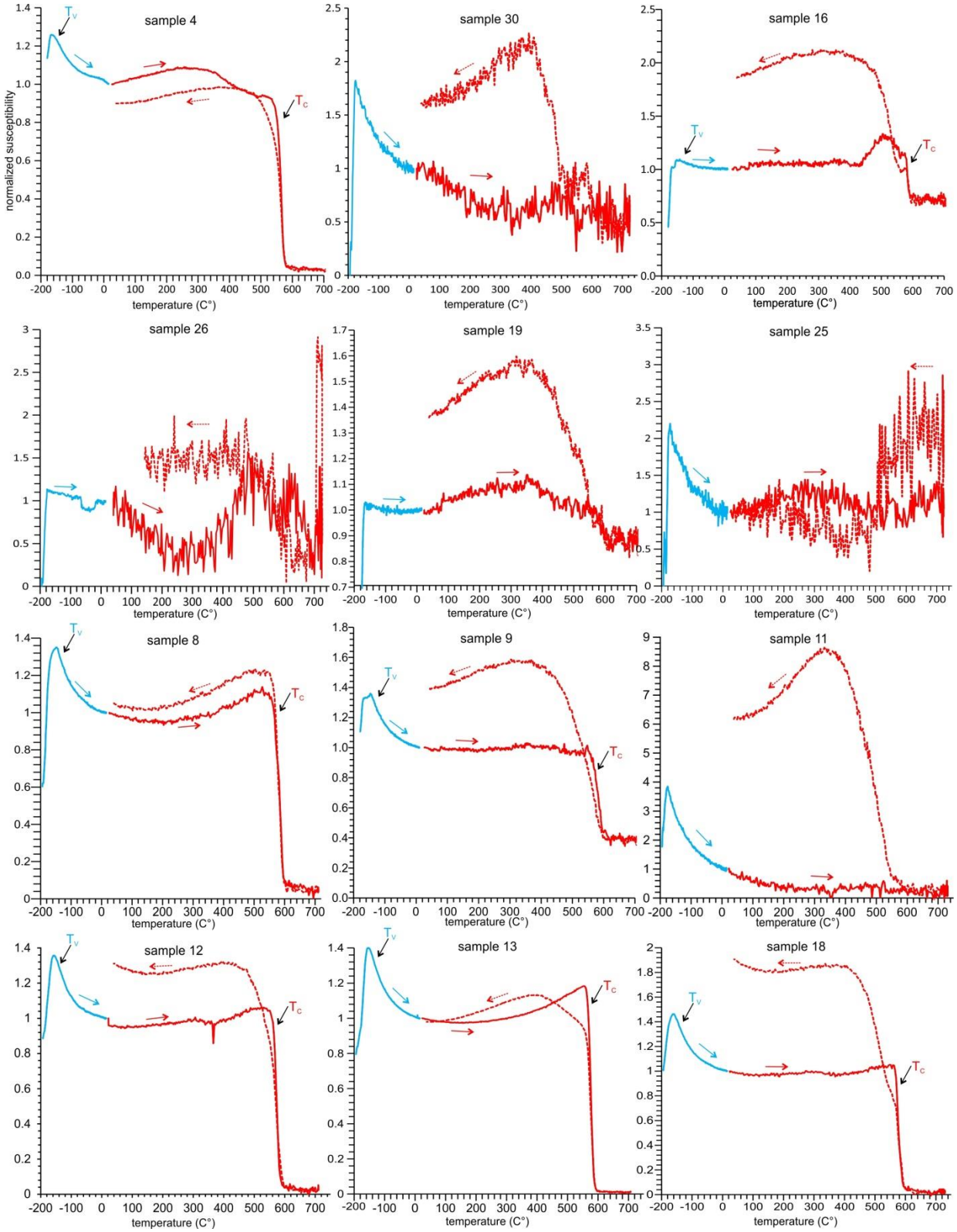

Figure AF8: Magnetic susceptibility (normalised by the susceptibility at 40°C) vs. temperature curves of crystalline basement rocks at the Lockne impact stricture.

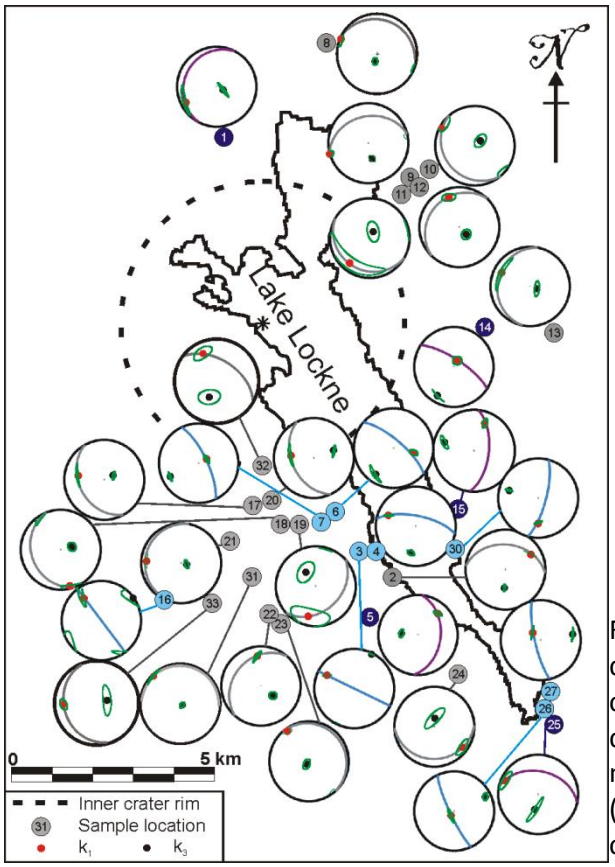

Figure AF9. Map of the Lockne area, demonstrating magnetic foliations, k_1, k_3 and corresponding confidence ellipse of the three dominant basement lithologies, i.e., metavolcanic (blue), granite (violet) and dolerite (grey). The data is averaged over all the cores, collected from a particular sampling site.

sample	lattitude	longitute	elevation
3	62.942791	14.821737	410.564
5	62.968282	14.828497	400.656
16	62.954023	14.872807	332.980
22	62.972129	14.828547	351.725
23, 24	63.037139	14.888395	345.477
25, 26	63.037139	14.888395	345.477
28	63.002635	14.953874	330.577
33	62.967291	14.706957	397.628
41	62.965601	14.817964	410.365
42, 43	62.962035	14.819637	413.73
44	62.966609	14.821518	405.559
46	62.958285	14.802494	404.838
47	62.942798	14.821723	402.915
48	62.942139	14.822484	402.900
49	62.930058	14.908902	372.634

Table AT7. GPS location of the dolerite samples. The latitude and longitude are in degrees and the elevation is in meters. The samples marked in red show alternating augite and labradorite lamellae.

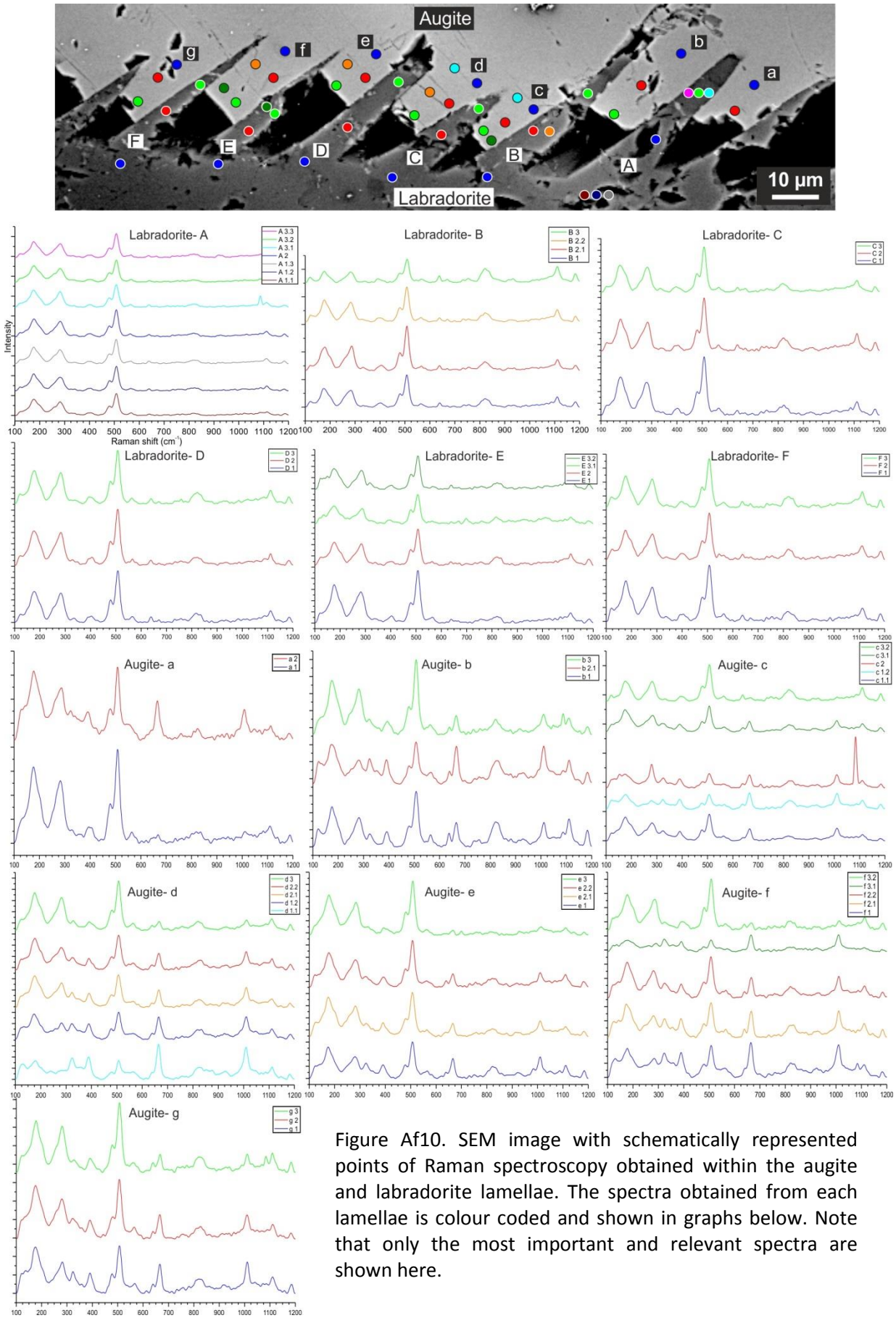

Figure Af10. SEM image with schematically represented points of Raman spectroscopy obtained within the augite and labradorite lamellae. The spectra obtained from each lamellae is colour coded and shown in graphs below. Note that only the most important and relevant spectra are shown here.

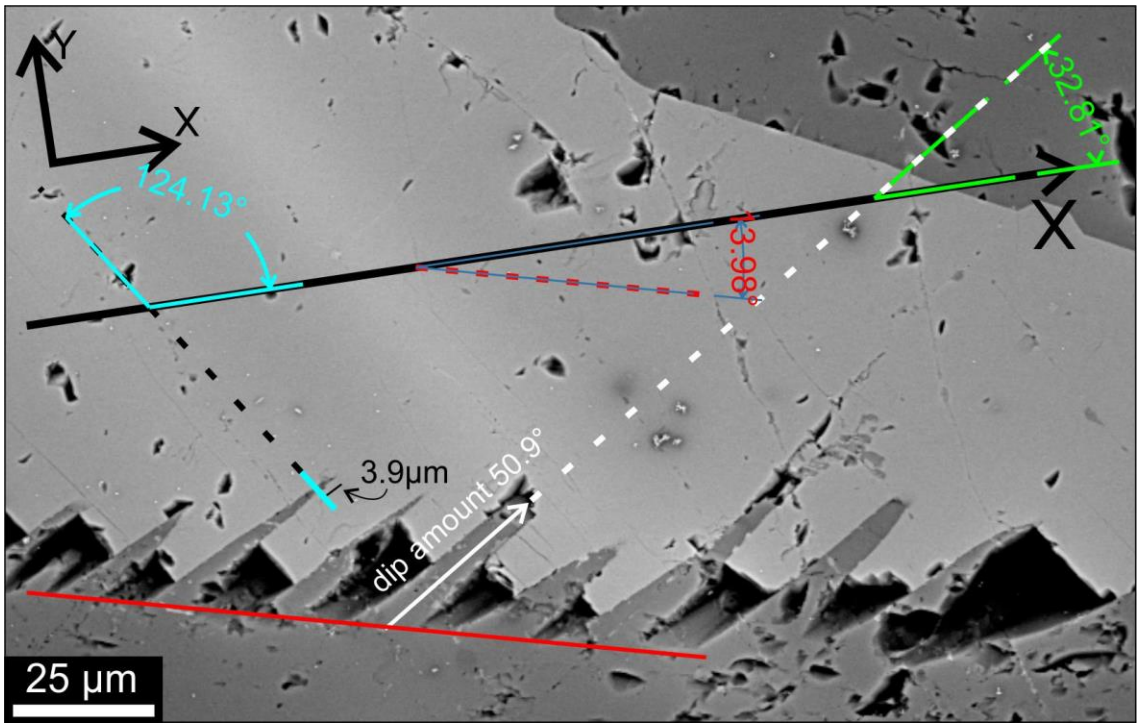

Figure Af11. The SEM image demonstrating critical the spatial relationships employed to plot the equal area plot, figure 4.3b. The actual location of TEM section is shown by blue line. It is perpendicular to the labradorite lamellae, and makes an angle of 124.13° from 'X'. The TEM section was extracted at 8.9 µm from the end of the labradorite lamella. Using this distance and the thickness of labradorite lamellae recoded during TEM measurements (Fig. 4.5a) dip amount of the trough of labradorite lamellae was calculated. The dip direction (white arrow) makes an angle of 32.81°.